3-2016

Analytical and experimental investigation of microstructural alterations in bearing steel in rolling contact fatigue

Sina Mobasher Moghaddam
Purdue University

Recommended Citation

Moghaddam, Sina Mobasher, "Analytical and experimental investigation of microstructural alterations in bearing steel in rolling contact fatigue" (2016). *Open Access Dissertations*. 682.
https://docs.lib.purdue.edu/open_access_dissertations/682

Graduate School Form 30
Updated 1/15/2015

PURDUE UNIVERSITY
GRADUATE SCHOOL
Thesis/Dissertation Acceptance

This is to certify that the thesis/dissertation prepared

By Sina Mobasher Moghaddam

Entitled

ANALYTICAL AND EXPERIMENTAL INVESTIGATION OF MICROSTRUCTURAL ALTERATIONS IN BEARING STEEL IN ROLLING CONTACT FATIGUE

For the degree of Doctor of Philosophy

Is approved by the final examining committee:

Farshid Sadeghi
Chair

Pablo Zavattieri
Co-chair

Rodney Trice
Co-chair

Ganesh Subbarayan

To the best of my knowledge and as understood by the student in the Thesis/Dissertation Agreement, Publication Delay, and Certification Disclaimer (Graduate School Form 32), this thesis/dissertation adheres to the provisions of Purdue University's "Policy of Integrity in Research" and the use of copyright material.

Approved by Major Professor(s): Farshid Sadeghi

Approved by: Jay Gore 3/11/2016
Head of the Departmental Graduate Program Date

ANALYTICAL AND EXPERIMENTAL INVESTIGATION OF MICROSTRUCTURAL ALTERATIONS IN BEARING STEEL IN ROLLING CONTACT FATIGUE

A Dissertation
Submitted to the Faculty
of
Purdue University
by
Sina Mobasher Moghaddam

In Partial Fulfillment of the
Requirements for the Degree
of
Doctor of Philosophy

May 2016
Purdue University
West Lafayette, Indiana

ACKNOWLEDGEMENTS

First of all, I want to express my deepest appreciation to my advisor Professor Farshid Sadeghi for providing me with the unique opportunity to join his laboratory. His comments and guidance have had an invaluable impact on both my professional and personal life.

Also, I would also like to thank Professor Ganesh Subbarayan, Professor Rodney Trice, and Professor Pablo Zavattieri for serving on my advisory committee and providing their very important inputs.

I would like to thank my wonderful friends and lab mates at Mechanical Engineering Tribology Laboratory (METL) with whom I collaborated. They made the work environment productive, friendly, and refreshing.

Finally, I would like to thank Mr. Thomas Kreis, Mr. Martin Correns, Dr. Markus Dinkel, Mr. Toni Blass, Dr. Vasilios Bakolas, and Dr. Nick Weinzapfel from Schaeffler Group for their intellectual and financial support of my research projects.

TABLE OF CONTENTS

Page

Page

LIST OF TABLES

LIST OF FIGURES

Figure Page

Figure Page

Figure Page

NOMENCLATURE

b	~Half contact width
BFI	~ Butterfly formation index
C	~Stiffness tensor
d_{inc}	~Inclusion diameter
D	~Damage variable
$\mathrm{D}_{\mathrm{c\text{-}Butterfly}}$	~ Critical damage for butterfly formation
$\mathrm{D}_{\mathrm{c\text{-}Crack}}$	~ Critical damage for crack formation
E	~ Modulus of elasticity
m	~Damage law exponent
N	~Number of cycles
$N_{appearance}$	~Number of cycles for butterfly appearance
ΔN	~Increment in number of cycles
ε	~Strain tensor
σ	~Stress tensor
σ_r	~Resistance stress
τ	~Shear stress
$\tau_{alternating}$	~Amplitude of shear stress
τ_{mean}	~ Mean shear stress
τ_f	~Fatigue limit

ABSTRACT

Mobasher Moghaddam, Sina. Ph.D., Purdue University, May 2016. Analytical and Experimental Investigation of Microstructural Alterations in Bearing Steel in Rolling Contact Fatigue. Major Professor: Farshid Sadeghi.

Rolling Contact Fatigue (RCF) is one the most common failure modes in bearings. RCF is usually associated with particular microstructural alterations. Such alterations (i.e. white etching cracks, butterflies, etc.) which lead to RCF failure are known to be among the most concerning matters to bearing industry.

In the current work, an analytical as well as experimental approaches are used to investigate “butterfly wing” formation, crack initiation and propagation from inclusions. A new damage evolution equation coupled with a FE model is employed to account for the effect of mean stresses and alternating stresses simultaneously to investigate butterfly formation. The proposed damage evolution law matches experimentally observed butterfly orientation, shape, and size successfully. The model is used to obtain S-N results for butterfly formation at different Hertzian load levels. The results corroborate well with the experimental data available in the open literature. The model is used to predict debonding at the inclusion/matrix interface and the most vulnerable regions for crack initiation on butterfly/matrix interface.

A new variable called butterfly formation index (BFI) is introduced to manifest the dependence of wing formation on depth. The value of critical damage inside the butterfly wings was obtained experimentally and was then used to simulate damage evolution. Voronoi tessellation was used to develop the FEM domains to capture the effect of microstructural randomness on butterfly wing formation, crack initiation and propagation. Then, the effects of different inclusion characteristics such as size, depth, and stiffness on RCF life are studied. The results show that stiffness of an inclusion and its location has a significant effect on the RCF life: stiffer inclusions and inclusions located at the depth of maximum shear stress reversal are more detrimental to the RCF life. Stress concentrations are not significantly affected by inclusion size for the cases investigated; however, a stereology study showed that larger inclusions have a higher chance to be located at the critical depth and cause failure. Crack maps were recorded and compared to spall geometries observed experimentally. The results show that crack initiation locations and final spall shapes are similar to what has been observed in failed bearings.

CHAPTER 1. INTRODUCTION

1.1 Historical Background

Ball and roller element bearing are crucial components of almost all the machinery with rotary motion. These highly engineered components have a dual functionality of supporting load and enabling rotational or linear motion with low frictional losses.

The earliest application of rolling element bearings is not exactly known. However, there are evidences available that human civilizations have been familiar with similar mechanisms to alleviate motion of heavy objects. Historical findings suggest that thrust bearings have been known to humans for a much longer time as opposed to radial bearings [1].

The first evidence of a device similar to thrust ball bearings dates back to about 40 AD in Roman Empire, where balls where installed under a table to manufacture a rotating dining table or wooden platform in ships [1] Figure 1.1 illustrates one such a design sketched after findings in lake Nemi. The first well documented design belongs to Leonardo Davinci who came up with a design very similar to a thrust bearing for his helicopter in 1498. His original sketch as well as a 3D CAD model of his design are shown in Figure 1.2. The first officially patented ball bearing was introduced by Welsh engineer Philip Vaughan in 1794 to be used in an axle assembly.

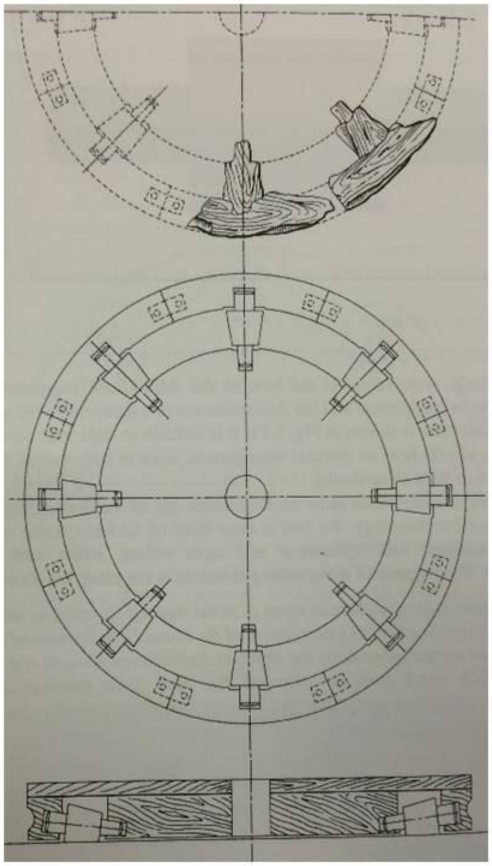

Figure 1.1. Schematic of the roman platform which rotates on wooden roller.

Figure 1.2. Davinci’s bearing mechanism; original sketch (left) as opposed to the 3D CAD model.

On the other hand, the first documented application of radial bearings dates back to 1869 when the first radial ball bearing was installed on a bicycle by Jules Suriray brought the winning place trophy of the world's first bicycle road race to James Moore. Ball bearing technology took a great leap forward in 1883 when Friedrich Fischer of Schweinfurt, Germany designed a machine to allow steel balls to be ground to an absolutely round state for the first time – and in large volumes; his ball grinder machine, is shown in Figure 1.3. Such advances culminated in more innovations such as introduction of first tapered roller bearing by Timken in 1898, followed by first modern self-aligning ball bearing by SKF in 1907. Finally in mid-20th century, Georg Schaeffler designed the first commercial needle bearing.

Figure 1.3. Fischer's steel ball grinder.

As described earlier, today's bearings are highly engineered mechanical components. Alongside the advances in the new designs, the materials used in bearing industries have also evolved significantly over the course of years. In general, desirable bearing material should be capable of carrying large amounts of load without major plastic deformation and suffer from wear. This results in a need to develop hard materials for both races and balls or rollers. New material processing techniques in early 20th century led to discovery of new materials such as AISI 52100 which is still widely in use in bearing industry [2]. Another big factor to consider is the fatigue life of bearings. As will be discussed later, many factors can govern the fatigue life of a bearing one of which is material cleanliness. The current research mainly focuses on the effect of crack formation and microstructural alterations from non-homogeneities that occur during the fatigue failure of bearings due to a phenomenon known as rolling contact fatigue (RCF).

1.2 Mechanisms of Rolling Contact Fatigue

If a bearing is installed properly and operates under appropriate environment, load and speed, the dominant mode of failure will be due to material fatigue. This phenomenon is commonly referred to as rolling contact fatigue. RCF has different modes that differ from one another in terms of driving factor and crack location. The most common types of RCF are surface pitting or subsurface spalling. Figure 1.4. compares two such types of failure. As can be seen, in surface pitting, the cracks start from surface and propagate into the material. The resulted spalls are normally not very deep. The root causes for surface pitting can be many factors such as improper lubrication which increases friction and wear or contaminants in the lubricant which can be trapped in the contact and increase the contact stress. On the other hand subsurface spalling is different both in initiation and propagation stages. In this type of fatigue failure cracks initiate from subsurface of the material and propagate towards the surface. The spalls are commonly deeper than those of surface failure.

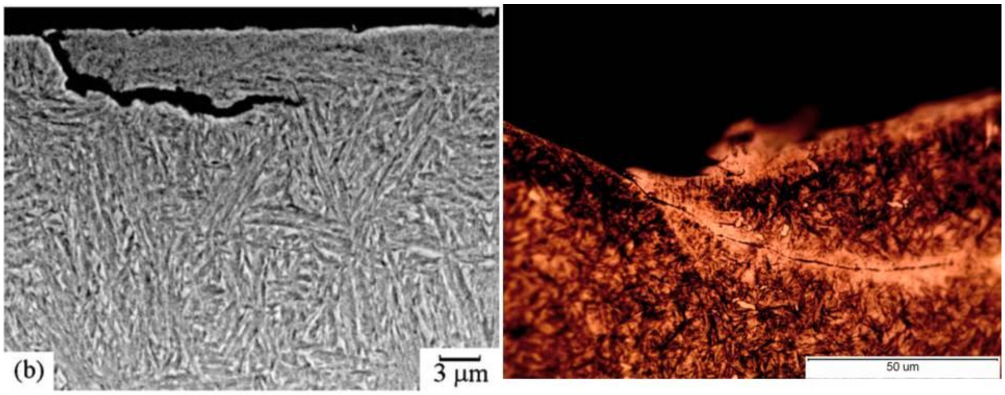

Figure 1.4. Surface pitting (left) as opposed to subsurface spalling (right). Note the difference in the crack depths.

As the current document focuses on microstructural alterations that are related to subsurface spalling, it would be beneficial to study the fundamentals of this type of failure more in depth. For this purpose consider the subsurface stresses when the material is subjected to Hertzian loading. Figure 1. depicts the stress history for a point located at 0.5b below the surface as the ball rolls over the point. As can be seen, shear stress is the only stress at the subsurface of the material which alternates between positive and negative values. Based on a similar analysis, Lundberg and Palmgren [3] suggested that subsurface shear stress alteration is the main cause for subsurface spalling.

1.3 RCF vs. Classical Fatigue

Compared to other common types of fatigue, for a number of reasons, RCF is more challenging and involved to investigate.

1. Classical fatigue mostly occurs at the surface. The main reason is due to existence of scratches and/ or notches on the surface that cause stress concentration points.

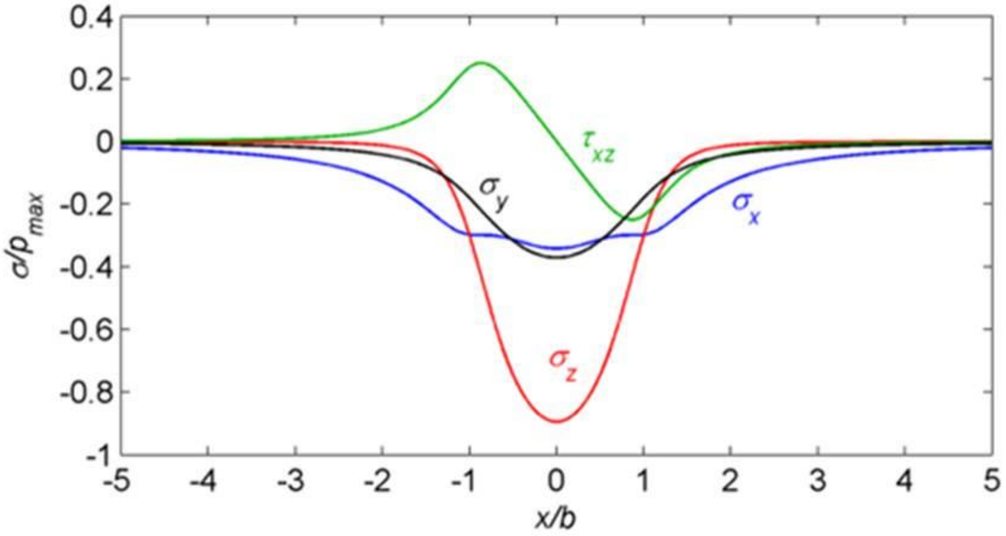

Figure 1.5. Different stress components experienced by an element located at the subsurface of the material as the ball over rolls.

Also, some common fatigue loadings are mainly bending problems. In such cases, the maximum tensile stress occurs at the surface of the part. Investigation of surface initiated fatigue is generally easier since the cracks are mostly visible and they can be tracked during the propagation stage. However, in RCF, the cracks mostly initiate and propagate from subsurface of the material which makes it more difficult to locate and track them.

2. In classical fatigue testing, e.g. uniaxial or torsion fatigue, specimens are subjected to loadings that produce bulk stresses. This causes damage to a large volume of the material and failure happens at the most critical point due to existence of stress risers like defects, inclusions, or dislocations. However, the stresses in RCF are highly localized within the non-conformal contact regions, e.g. a rolling element on a bearing raceway. Consequently only very small volumes of the material are subjected to very large values of stress and a significant stress gradient versus location exists in the matrix.

3. At such small scales, it is not easy to apply common fatigue analysis methods such as linear elastic fracture mechanics (LEFM). This is mainly due to the crack sizes which are comparable to microstructural grain size. Thus, the crack propagation can be affected by microstructural geometry of the material. This makes it of great importance to differentiate between intergranular and transgranular crack propagation assumptions in RCF studies.

4. There is a large compressive component of hydrostatic stress in rolling contacts which tends to inhibit Mode I crack growth,but there is not sufficient information regarding how it affects the Mode II crack growth which is the main cause of RCF.

5. Different stress components, as pictured in Figure 1., experience their peaks at different times during a loading cycle. This culminates in a complex multiaxial state of stress which changes the direction and magnitude of principle stresses at different moments. This makes it very important to consider the history of all stress components during loading cycles.

The above points are some of the reasons that make RCF and RCF related phenomena more challenging to investigate and understand. Some of the most complicated of such phenomena are the microstructural alterations that are observed in the steel that is damaged by rolling contact loading. The next section describes different types of such alterations in bearings steel and categorizes them.

1.4 Microstructural Changes Due to RCF

In addition to surface pitting and subsurface spalling, RCF can happen due to other phenomena as well. Some of such fatigue failures are associated with microstructutal alterations in bearing steel. This section presents a short review of such changes.

The first record of microstructural alterations in bearing steel dates back to mid-20th century when Styri [4] reported formation of ferrite grains around nonmetallic inclusions in bearing steel during post failure inspection.

The most common types of microstructural alterations in bearing steel can be categorized as butterflies wings, dark etching region (DER), white etching bands (WEB) which consist of 30 degree and 80 degree bands and white etching cracks (WEC). Different affiliations may use different terminology for some of these features. However, they are mostly named because of their appearance under microscope after the steel is cut, polished, and etched. Figure 1.-a shows a pair of wings which are formed around an Aluminum Oxide inclusion [5]. Figure 1.-b shows DER and WEBs [6]. As will be discussed later, DERs form in the highly sheared region, and WEBs normally form inside the DERs. However, butterflies mostly form around the non-metallic inclusions that exist in bearing steel; WECs, shown in Figure 1.-c [7], have a more sporadic nature. Their location and the time they occur varies more compared to other features which makes them more difficult to study.

Figure 1. describes the chronological order of appearance of different microstructural alterations according to [8]. Butterfly wings (not shown in this figure) are believed to initiate at approximately one thousandth of L_{10} life of the material. It can be seen that if the load is large enough DERs appear the second. After that, 30 degree bands are next features to form. Their appearance is followed by 80 degree bands which are the last features to nucleate. This pattern for chronological order of appearance for microstructural changes is confirmed by [9] and [10]. A detailed description of each of these features follows.

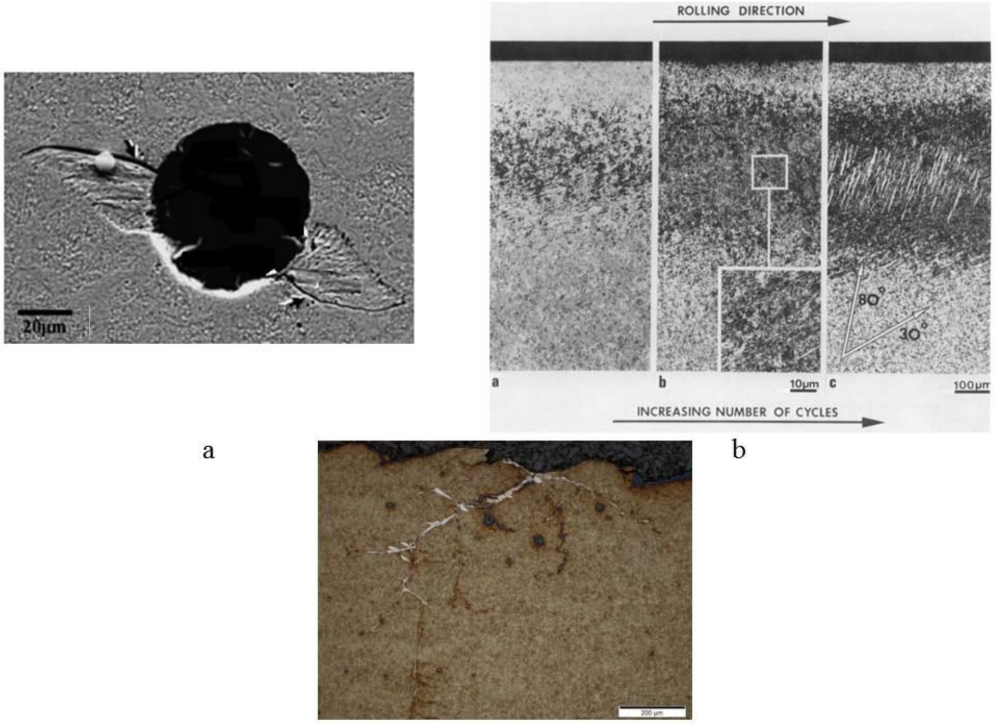

a b

c

Figure 1.6. Different types of microstructural alterations: a) Butterfly wings formed around an Alumina inclusion, b) DER, flat and steel WEBs, c) WEC (references are cited in the text).

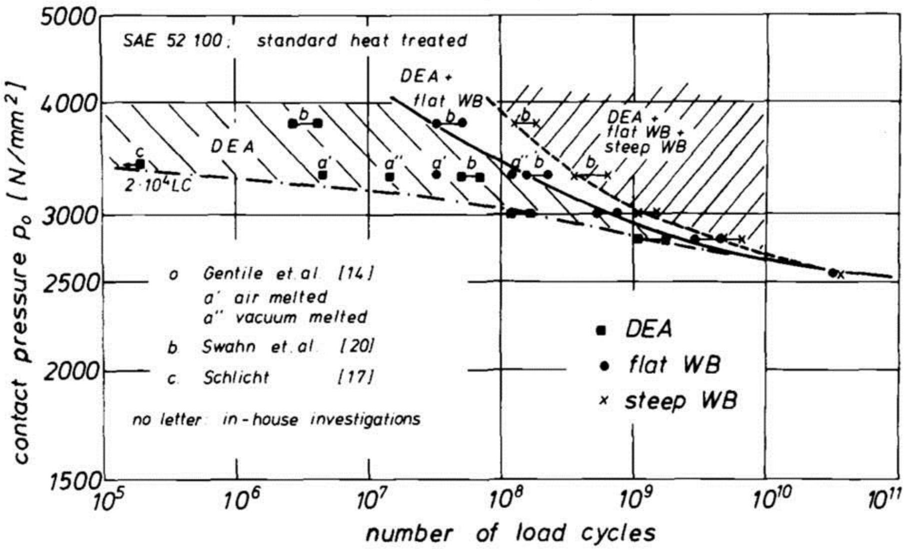

Figure 1.7. S-N curve demonstrating the chronological order of appearance of microstructural alterations [8].

1.4.1 Butterfly Wings

Butterfly wings where first noticed by Styri in 1951 [4]. They can be identified as a pair of altered microstructure around the inclusion which forms at 45 degree angle with respect to the rolling direction. Studies have shown that material microstructure changes from martensite to ferrite in these regions. The reason for the color change is probably due to different grain sizes inside the wings which affects the wavelength of the reflected light from the etched surface. The ferrite grains can be as small as 5-10 nm inside the wings as opposed to a typical 10 um grain size for the pristine martensitic matrix.

Since the first observations, many research studies have focused on butterfly formation to develop a better understanding of fatigue of ball bearings. The main reason for such an interest is due to existence of many microcracks inside the butterfly wings. The cracks can be either inside the wings or at the wing/ matrix interface. Normally a higher density of cracks is observed on top of the upper wing and bottom of the lower wing, as shown in Figure 1.-a with small arrows. While the butterfly progression can stop after a while [11], the cracks may either arrest or grow beyond the wings and grow to the surface to cause the final fatigue failure.

As mentioned before, butterflies are the first microstructural alterations to appear in the steel. Kyozaburo et al. [12] have suggested that they can appear as early as one thousandth of L_{10} life. So, butterfly appearance has been used as a measure for bearing life assessment for relatively low loads where the actual RCF test till failure may take a very long time.

To avoid repetition, a more detailed description of previous research on butterflies is not presented here as it will appear in the introduction of Chapters 2 and 3.

1.4.2 Dark Etching Region

DER is identified by a dark contrast region after the material is etched with nital and looked at under optical microscope. Figure 1. [8] illustrates the DER both in the transverse and parallel planes of a bearing raceway. As can be seen, DER forms in the raceway of the bearing just below the contact region. This region is associated with high stresses due to Hertzian contact; however, the depth and shape of this region makes it hard to associate it with a certain stress component. It is known that the region expands with increasing pressure or number of cycles [13].

Different theories have been postulated to analyze the root causes of DER. Zwirlein [8] suggests that DERs form due to a combination of high compressive stresses with surface shear which happens because of forward or backward slip.

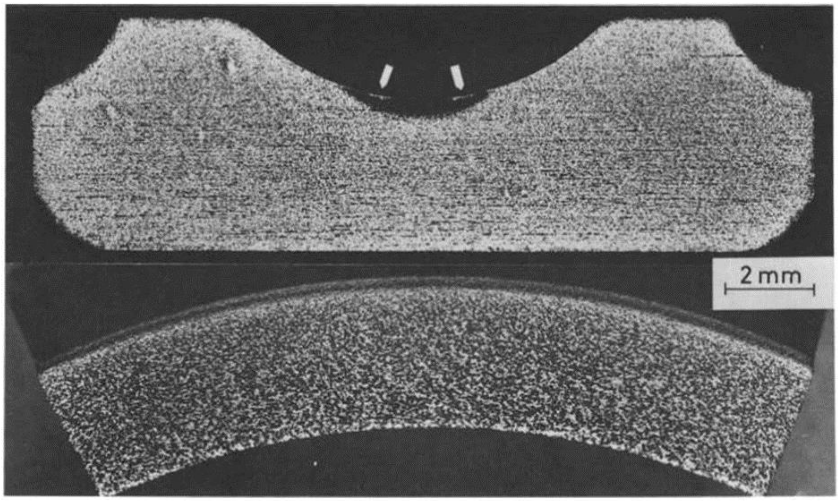

Figure 1.8. DER formation as observed in the transverse and parallel cut planes [8].

Martin [14] et al. observed that heat treatment can be effective in the formation of DER. They suggest that a decrease in the amount of retained austenite which happens during the tempering process can be responsible for absence of DER in their tests. Warhadpande et al. [9] mention a similar observation in their literature review of microstructural changes. Many researchers have suggested that DER forms because of drastic plastic deformations at high loads. Warhadpande et al. [9] suggest that DER matches with the area of maximum unidirectional shear stress closely. Consequently, some researchers have investigated plastic strain accumulation and work hardening in the material as an explanation for DER formation. However, the observations are not very consistent. For instance Bush et al. [15] reported hardness values as low as 53 HRC for DERs that exist in a matrix with 61 HRC for virgin microstructure. A similar phenomenon was observed by Thielen et al. [16]. However, more recently, Bhattacharyya et al. [17] conducted a comprehensive study on the effect of work hardening inside the DER. Their investigation clearly shows an increase in the hardness level due to plastic deformation in the DER.

It should be noted that so far, DER is not proven to have any direct adverse effect on RCF. Even some researchers such as Ruellan et al. [18] suggest that DER is associated with some volumetric expansion of the material which culminates in excess amounts of residual stress and hinders the crack propagation. On the other hand, it is well known that DER can lead to WEB formation and as discussed in the next section, WEBs can include micro cracks and cause material fatigue.

1.4.3 White Etching Bands

The next features to appear in bearing steel are white etching bands. WEBs commonly form after DERs and inside this region. As described before, two types of bands are usually observed. First 30 degree bands, also known as flat bands, form inside the DER. These bands are inclined towards the over rolling direction (ORD) with an angle of about 20-35 degree [13]. In certain applications such as gears [19] the bands have been observed to form angles as high as 45 degree with ORD. The carbon content within the bands is normally less than the parent matrix. Flat bands are 5-30 µm in length and 0.1-05 µm in width, and their spacing is about 0.5-10 µm.

The very last features to appear are 80 degree or steep bands which can vary from 65 to 85 degree in angle [13]. It should be noted that some affiliations refer to 80 degree bands as WEC which stands for White Etching Constituent. This is different than White Etching Cracks which will be discussed in the next section.

WEBs are known to be a sign of severe material damage due to fatigue. Martin et al [14] confirmed the existence of microcracks along the steep bands. Steep bands are commonly formed in the very same region as flat bands; however, they have a relatively bolder appearance and their spacing is wider. For instance, Swahn et al. [6] observed 10x100 µm sized bands which were spaced about 5-50 µm apart in a plane parallel to ORD. The orientation of the bands has always been an unanswered question. Keer and Polonsky [20] in a comprehensive stress analysis discussed the possible effect of different stress components on WEB formation. As they mention, the most probably stress component to cause WEBs is shear stress. But, there exists an issue with such an approach: shear driven phenomena always occur on complementary planes. It means that if there is a band at 80 degrees, we should expect a similar band formed at -10 degrees as well, which is note case according to Keer and Polonsky [20]. Although this is observation is correct for almost all the cases, the author has noticed that in some cases the WEB are formed in complementary planes as well. Figure 1. from published by Forster et al. [21] shows such bands. Another, unique observation is made by Muro and Tsushima in an earlier study in 1970 [22]. As shown in Figure, the formation of bands geometry can involve even more irregularities. Although a lot is unknown about WEB formation, not much experimental or analytical work is conducted to investigate such features. Recently, Gegner and Nierlich [23] and Uyama et al. [24] studied the effect of Hydrogen charging as a possible factor in WEB formation. Holweger et al. [25] have used nondestructive subsurface damage monitoring methods such as fractal dimension analysis to track WEB formation in-situ. In 2013, Warhadpande et al. [9] conducted a comprehensive literature review on the topic. They continued their work by combining a FE model with Fick's law of diffusion to simulate WEB formation [26].

1.4.4 White Etching Crack

White Etching Crack (WEC) is one of the most concerning types of alterations in bearing steel. While WEBs normally initiate after L_{10} life of the bearing, WECs can occur as early as 1-10% of L_{10} life of the bearing [27]. This makes WECs an expensive problem to the industry. Their appearance especially in heavy duty bearings can increase the maintenance costs drastically. For instance, wind turbine bearings are usually designed to last for 20 years of operation; however, irregular failures due to WEC can happen only after 6 months to 2 years of installation. WEC have grabbed an increasing attention in the recent decades with the increasing demand for clean energy. This makes it of great importance to understand them more in depth. Root cause analysis of WEC is an

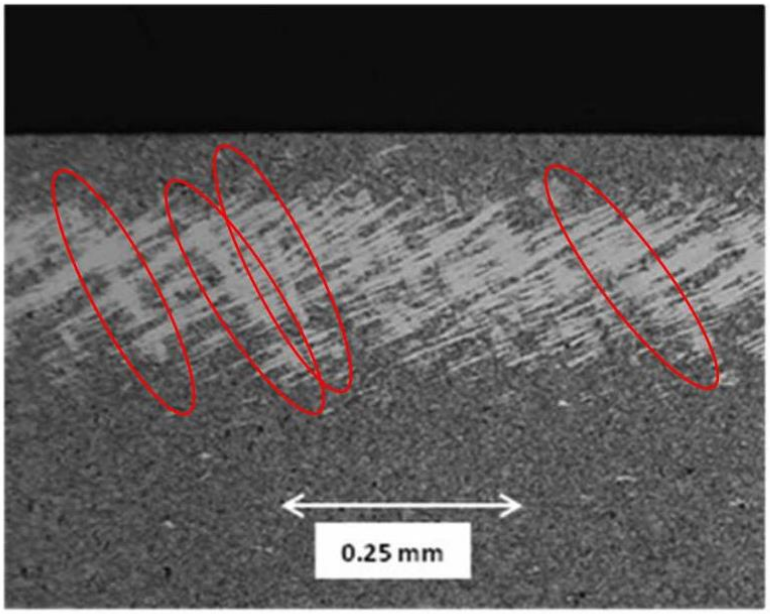

Figure 1.9. A unique observation: formation of WEBs at complementary angles [21].

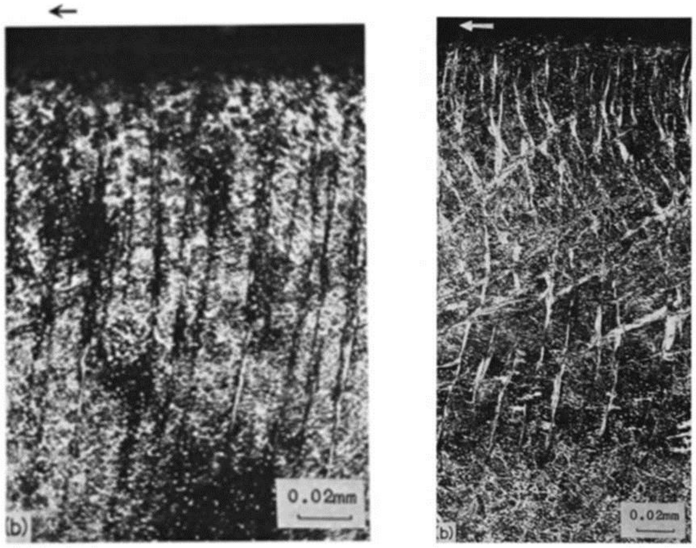

Figure 1.10. Irregular shape and orientation of WEBs. The ORD is pictured with the arrow on top [22].

involved problem. So far, no single factor is known to be the cause for WEC formation, and a combination of factors seems to be responsible for their formation. Such ambiguities make it even harder to reproduce WECs in the lab under similar operational condition. For example, WECs are observed in wind turbine bearings that operate under relatively low stresses as low as 1.0-1.5 GPa, however the attempts to reproduce them in lab at such low loads has not been successful. As mentioned before, there are many factors believed to play role in WEC formation. Currently, the most widely accepted theory for WEC formation focuses on Hydrogen embrittlement (HE) in the steel [18,23,24,27,28]. It is a well-known fact that Hydrogen atoms can penetrate inside the steel matrix. In the case of bearings, lubricant can be a potential source to provide Hydrogen. The diffusion procedure is commonly reversible, however, there are irreversible traps such as grain boundaries and inclusions which cause the Hydrogen to stay inside the matrix and embrittle it. Although, the experimentalists have not been able to achieve great success to diffuse Hydrogen inside bearing by just replicating the operational conditions in the lab, artificial charging methods has obtained more popularity and resulted in successful reproduction of WECs in the lab environment[29].

Recently, some efforts have been made to model WEC formation. Gurijic et al. in a series of three papers [30–32] have used CZM elements on the edges of Voronoi cells to simulate the embrittled grain boundaries. Kadin [33,34] has used Fick’s law to model Hydrogen diffusion inside a 1-D matrix. Due to importance of WEC formation, and because the future work chapter of this document focuses on this phenomenon, a more detailed description of the WEC is left for the last chapter.

1.5 Scope of the Thesis

As mentioned in the previous sections, there are different types of microstructural alterations observed in the bearing steel. Among these, butterflies and WECs have been more concerning to the industry; butterflies, because they act as RCF crack initiators from inclusions, and WECs, because they cause premature and irregular failure in the steel.

For the case of butterflies, despite tremendous amount of experimental efforts there are very few models available to simulate this phenomenon. However, considering the recent experimental findings, it seems that there is enough information available to solve modeling of this problem. This forms the main frame of current research. An effort is made to postulate a model for butterfly formation in bearing steel. The investigation mainly uses an analytical and numerical approach to simulate the phenomenon. Also, experimental tests have been conducted to check the validity of the suggested model, or to find out necessary inputs that were not possible to obtain from the open literature.

Chapter Two provides a comprehensive review of previous investigations of butterflies since mid-1950s. Then the fundamentals of damage mechanics are discussed and a modified damage model is postulated for butterfly formation in 2D. FE model is introduced and exercised and the primary results are compared with those observed by experimentalists.

Chapter Three extends the already introduced model and ties it with a model that simulates crack initiation, propagation, and final failure. Although the main focus of research is not life calculation, a relative fatigue life comparison is conducted for different inclusion characteristics to find which inclusions are the most detrimental to bearing life.

At the end, Chapter Four discusses the outlines of the future work. The extension of the model into 3D and the necessities for such a study are discussed. Also, the author plans to investigate an experimental as well as a numerical approach to study WEC phenomenon during the remaining of his PhD. The WEC study is targeted to build the infrastructure of a more comprehensive research on root cause analysis of WECs for the future.

CHAPTER 2. A DAMAGE MECHANICS APPROACH TO SIMULATE BUTTERFLY WING FORMATION AROUND NON-METALLIC INCLUSIONS

4.1 Introduction

Ball and rolling element bearings are a critical part of all machines and mechanisms which have rotary and relative motion. Because of their geometry, these elements usually operate under large stresses. It has been observed that bearings can fail because of environmental debris, improper lubrication systems, excessive loading etc. If a bearing is properly installed and maintained, the main mode of failure will be due to material fatigue. Historically, it has been postulated that a loaded rotating element has a limited life because of the probability of the subsurface initiated fatigue spalls. Failure due to this phenomenon is commonly referred to as rolling contact fatigue (RCF).

It is commonly believed that RCF is caused by alternating subsurface shear stresses. Assuming b is the half width of the Hertzian contact, Figure 2.1 shows the stress history at a point located at 0.5b below the surface. As can be seen in Figure 2.1, in-plane shear stress is the only alternating stress component. Subsurface cracks initiate due to these stresses, coalesce together and grow to the surface forming spalls that cause the final RCF failure[35,36]. It is believed that subsurface cracks initiate at material imperfections, such as voids, dislocations and particularly non-metallic inclusions which act as stress risers [37,38]. It is frequently observed that crack initiation from inclusions is accompanied with microstructural changes. These microstructural alterations are commonly referred to as "butterfly-wings" due to their appearance. Kyozaburo et al [39] suggested that butterflies appear around one thousandth of the L10 life of bearing steel in rolling contact. They used butterfly appearance as a criterion to find the fatigue limit of different bearing steels.

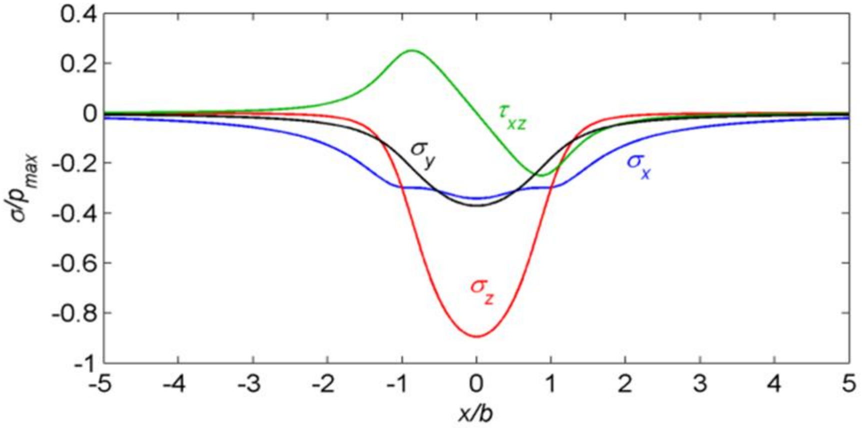

Figure 2.1. Normalized stress history experienced by a point located at 0.5b under a bearing surface.

Butterfly formations in bearing steel were first detected in 1951 by Styri [4] who observed a pair of altered microstructure regions emanating from the non-metallic inclusions. Over the past 60 years, many other investigators have observed butterflies and studied their characteristics [39–42]. There is still a significant amount of controversy over the possible mechanisms culminating in butterfly formation and no widely accepted theory has been presented. Consequently, any work on this topic needs to include a comprehensive literature review to consider and compare different schools of thoughts.

Figure 2.2 depicts schematically the details of a typical butterfly. Butterflies are observed to have a pair of wings around the inclusions that are oriented along a direction which forms an angle of 30 to 60 degrees with respect to the rolling direction (40-45 degrees is most prevalent in the case of a spherical inclusion shape). This implies that alternating shear stresses are probably the driving factor for the formation [43]. However, as will be discussed later, there are four regions of maximum alternating shear stresses around the inclusions while most of the butterflies have only two wings. This indicates that formation of the wings is strongly affected by rolling direction. Tricot et al. [xx11] proved this fact in a classic paper by creating four-wing butterflies only after interrupting the test and reversing the rolling direction.

Material properties and the formation mechanism of butterflies have been studied by several researchers [13,20,27,41,44–52]. Many researchers [11,20,41,52–56] convey that a phase change from martensite to ferrite occurs in these regions. Early researches suggested temperature effects and dynamic recrystallizations (DRX) as a potent source for these changes, but later works reject these factors and introduce a low-temperature recrystallization (RX) process as a more plausible mechanism[47,49,50]. Butterflies exhibit a fine grain size as compared to the parent matrix [13,51,52]. Different investigations observed different grain sizes and ranges within the butterflies. Grain size generally varies from 10 nm to 100 nm. Grains shrink in size when moving from the inclusion vicinity to the crack tips [46,47].

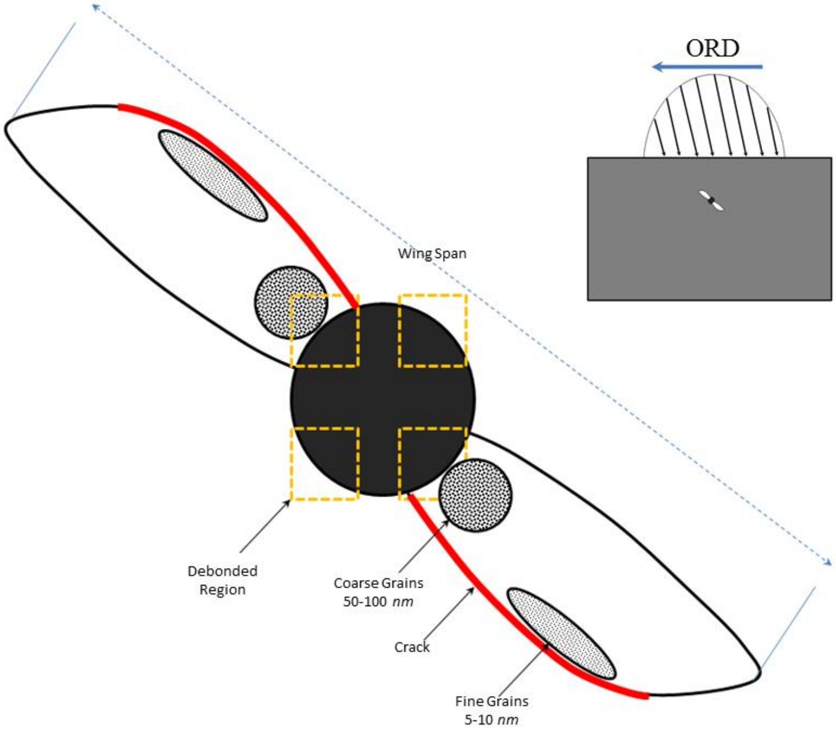

Figure 2.2. Schematic of a typical pair of butterfly wings. Note the Over Rolling Direction (ORD).

Table 2.1 lists the grain sizes in butterflies as observed by different researchers. Several investigators [5,52,56–58] have examined the hardness of butterflies. In general, the results consistently indicate that the altered regions have a hardness value of more than 1000 HV as opposed to the parent martensite that varies from 600-800 HV.

Table 2.1. Comparison of grain sizes observed by different authors in the altered microstructure of bearing steel

Author	**Grain Size (nm)**
Evans[8,16,50]	**10-60**
Grad[51]	**70**
Grabulov[5,45,46,60]	**10-1000**
Becker[43]	**10-100**

Many researchers have observed, cracks growing along the butterflies. In most cases there is a major crack at the junction of the butterfly/matrix interface. These primary cracks are commonly observed on the top of the upper wing and the bottom of the lower wing [44] as illustrated in Figure 2.2 with red lines. However, secondary cracks may appear on the opposite sides or even inside the wings [44]. It is suggested that coalescence of micro cavities in the butterfly-matrix interface which is governed by Mode I loading causes the micro crack formation [11]. Dominance of Mode I loading on butterfly crack initiation in the vicinity of the inclusions is confirmed by Evans [44] and Umezawa [57].

Another important factor to consider is when butterflies appear in the bearing steel. It should be noted that it is quite difficult to determine the exact number of cycles when butterflies start to form, as they form inside the material and before the final failure. Takemura [36] used the results of more than 400 RCF tests to determine an estimation of when butterflies do appear. His results show that butterflies commonly form in advance to other microstructural alterations.

In recent years, new techniques such as focused ion beam (FIB), transmission electron microscopy (TEM), ultrasonic C-scans, X-ray tomography and serial sectioning has led to new findings regarding butterfly formations. Evans [44], Grabulov [45], and Umezawa [57] have used FIB, TEM, and scanning electron microscopy (SEM) to closely examine microstructural changes. Their works shows that voids and micro cavities on butterfly boundary join together to form the micro cracks. They have used serial sectioning for 3D reconstruction of butterfly maps [27,58]. Grabulov in another paper [5] used electron backscatter diffraction (EBSD) to study butterfly matrix bondings and concluded that debonding in the inclusion/matrix interface can have a substantial effect on butterfly formation. Umezawa [57], Stienon [61], and Guy [62] have implemented high-frequency ultrasonic tests to monitor crack initiation at the inclusion.

Despite the considerable amount of experimental analysis on butterflies, very few researchers have attempted to investigate this problem analytically. Alley et al. [63] used plastic strain accumulation around cubic and circular inclusions to model butterflies. This approach successfully predicts the formation of two wings, but fails to predict the shape and orientation of the wings. Vincent et al. [64] suggest dislocation emission on the inclusion/matrix interface as the driving factor for butterfly formation; their model predicts the butterfly shape and orientation very well, but envisages four-wing butterflies as opposed to the two-wing butterflies that are dominant in experimental investigations. Melander [65–67] assumed the cracks to be initiated along a line that forms a 45 angle with the rolling direction. Then he studied the crack propagation in the vicinity of inclusions for different inclusion/matrix bonding scenarios using fracture mechanics. Umezawa [57] conducted an FEM analysis to find the most vulnerable regions around the inclusion for crack propagation; however, his model does not predict the existence of two major wings. Lewis and Tomkins [11] have used fracture mechanics to find the maximum allowable contact stress versus inclusion size for butterfly formations, but their work does not deal with location and orientation of the altered microstructure. Previous investigators have addressed various aspects of butterfly wings; however, there is no model capable of predicting the shape, orientation of two wing butterflies and their appearance as function of load cycle successfully.

In the current investigation a new approach to model butterfly formation is presented. A 2D FEM model was developed to obtain the stress distribution around a circular inclusion which has its main axis transvers to the rolling direction. Continuum damage mechanics was used to model the fatigue damage and microstructural alterations around the inclusion. A new damage evolution law is postulated which takes the effect of mean stresses into account. The model envisions the butterfly shape, orientation, and size successfully. The model was used to obtain S-N curve for butterfly appearance and the results are in good agreement with the experimental data. The stress solution is implemented to predict the debonding regions on the inclusion/matrix interface and possible locations for crack initiation on butterfly/matrix interface. In both cases the results corroborated well with experimental observations.

2.2 Modeling Approach

2.2.1 FEM Model Set Up

To investigate the effect of non-metallic inclusions on rolling contact fatigue of bearing steel, a 2D finite element model with plane strain assumptions and constant strain triangle (CST) elements is developed using commercially available software ABAQUS to represent a semi-infinite domain. The length of the domain is chosen to be 1000 μm and the width is set to 700 μm. A circular non-metallic inclusion is located on the vertical centerline of the domain. The modulus of the matrix and inclusion are set to 200 GPa and 300 GPa respectively. It should be noted that 300 GPa is close to the modulus of elasticity of Al2O3 which is one of the most common types of inclusions around which butterflies form. To reduce the computational effort, four different levels of mesh density are chosen such that the mesh size around the inclusion is finest (0.05 dinc) and at the outer most regions from the contact zone it is 20 μm. The user defined subroutine UTRACLOAD is developed to apply a parabolic pressure profile to the surface representing the Hertzian contact stresses. The peak value of the Hertzian pressure is 2.0 GPa and the half-contact width is 100 µm. The pressure profile is moved over the surface in 21 steps with its centerline displaced from -100 µm to +100 µm. The value of surface friction coefficient is assumed to be 0.05. The direction of surface traction is opposite to over rolling direction (ORD) to be consistent with previous experimental and analytical work presented in [68–71]. Figure 2.3 illustrates the model geometry schematically.

It should be noted that in this investigation the simulation results are compared to the experimental data available in the literature. Since there is variation in parameters among different references, in each case it has been tried to set the simulation parameters (such as inclusion diameter) as close as possible to the reference data. For the sake of clarity, the inclusion diameter modeled in each section is mentioned specifically.

2.2.2 Stress Analysis

It is a well-known that inclusions function as stress risers. The stress concentrations are commonly very local and reduce with increasing distance from the inclusion. The stresses along the centerline of a Hertzian contact are shown in Figure 2.4 for two scenarios: with and without an embedded inclusion. As illustrated in the figure, the stress concentrations are negligible for the points that are farther than a distance dinc from the inclusion/matrix interface. Since the goal of this study is to investigate butterfly formation mechanism, the representative volume element (RVE) is selected such that it includes all the regions which are significantly affected by stress concentrations due to inhomogeneity. For this purpose, the RVE size chosen for each case is a square with a length of $3d_{inc}$ and the inclusion is located at the center of the RVE. The detailed geometry of the RVE is illustrated in Figure 2.3.

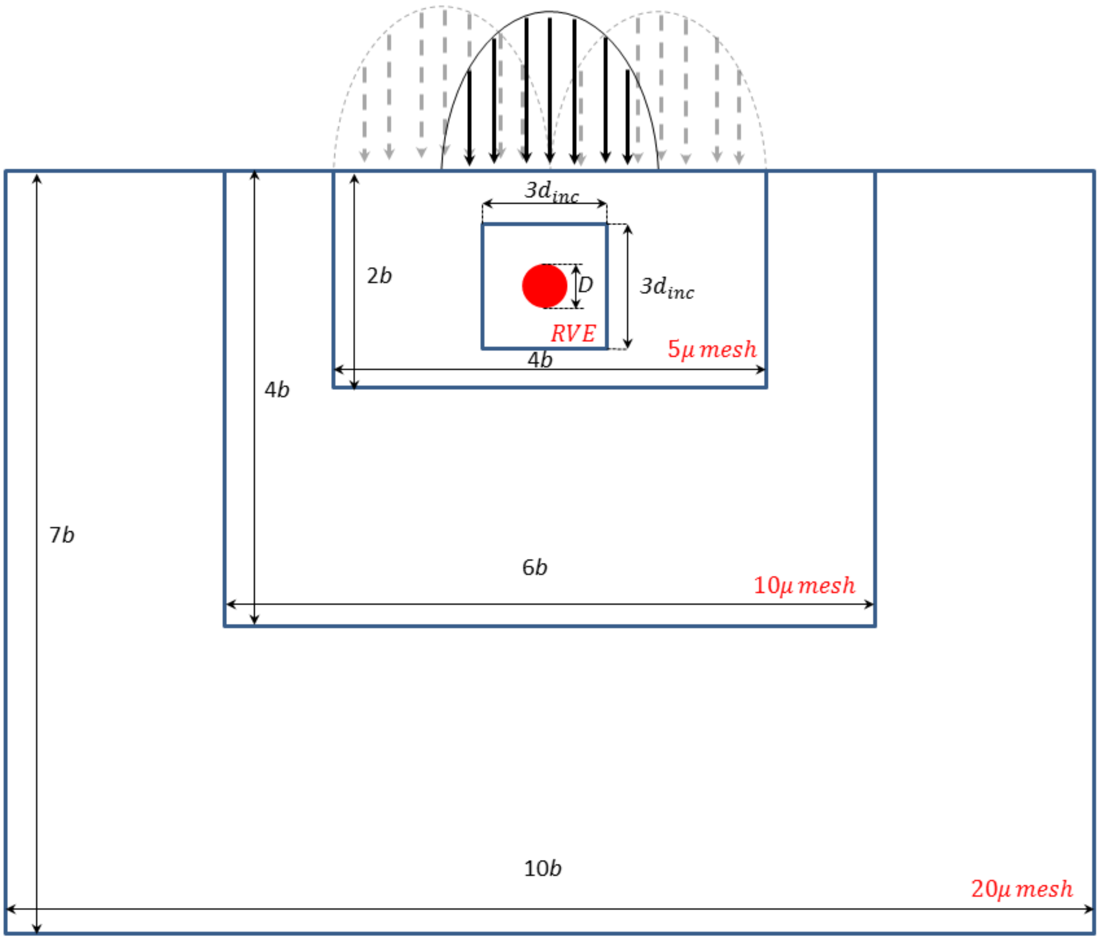

Figure 2.3. Schematic of the domain with relative dimensions (Inclusion location and diameter vary in different cases).

As described earlier, butterflies appear after a considerable number of load cycles in the material; they also mostly form in the depths associated with maximum subsurface shear stresses [68]. Figure 2.5 depicts the shear stress variation around an inclusion located at 0.5b as the Hertzian load passes over the inclusion. As shown in Figure 2.5, no single Hertzian pressure location relative to the position of inclusion reveals clear information explaining the formation of just two wings. This indicates that any stress-based approach to describe butterfly formation should take into account the stress history of the material during each loading cycle. Assuming butterfly formation to be a fatigue related phenomenon, it is important to take the effect of alternating shear stresses into account.

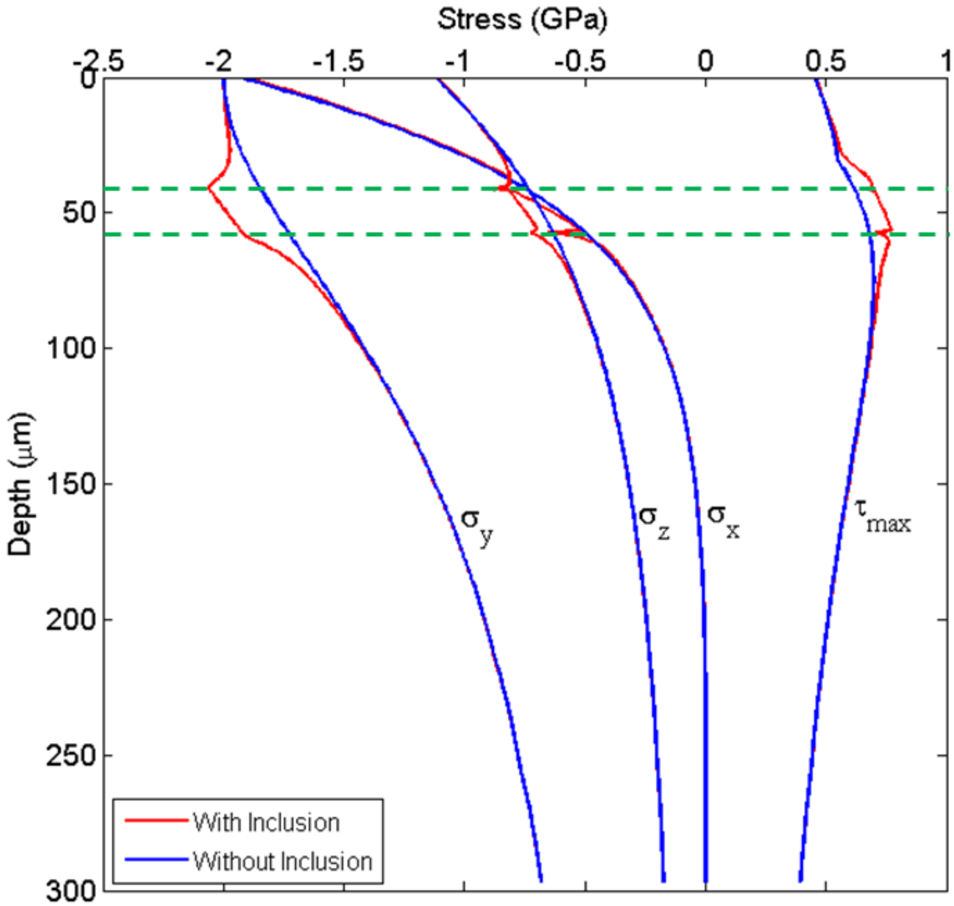

Figure 2.4. Centerline stresses for two domains with (red) and without (blue) an inclusion for a 16 μm.

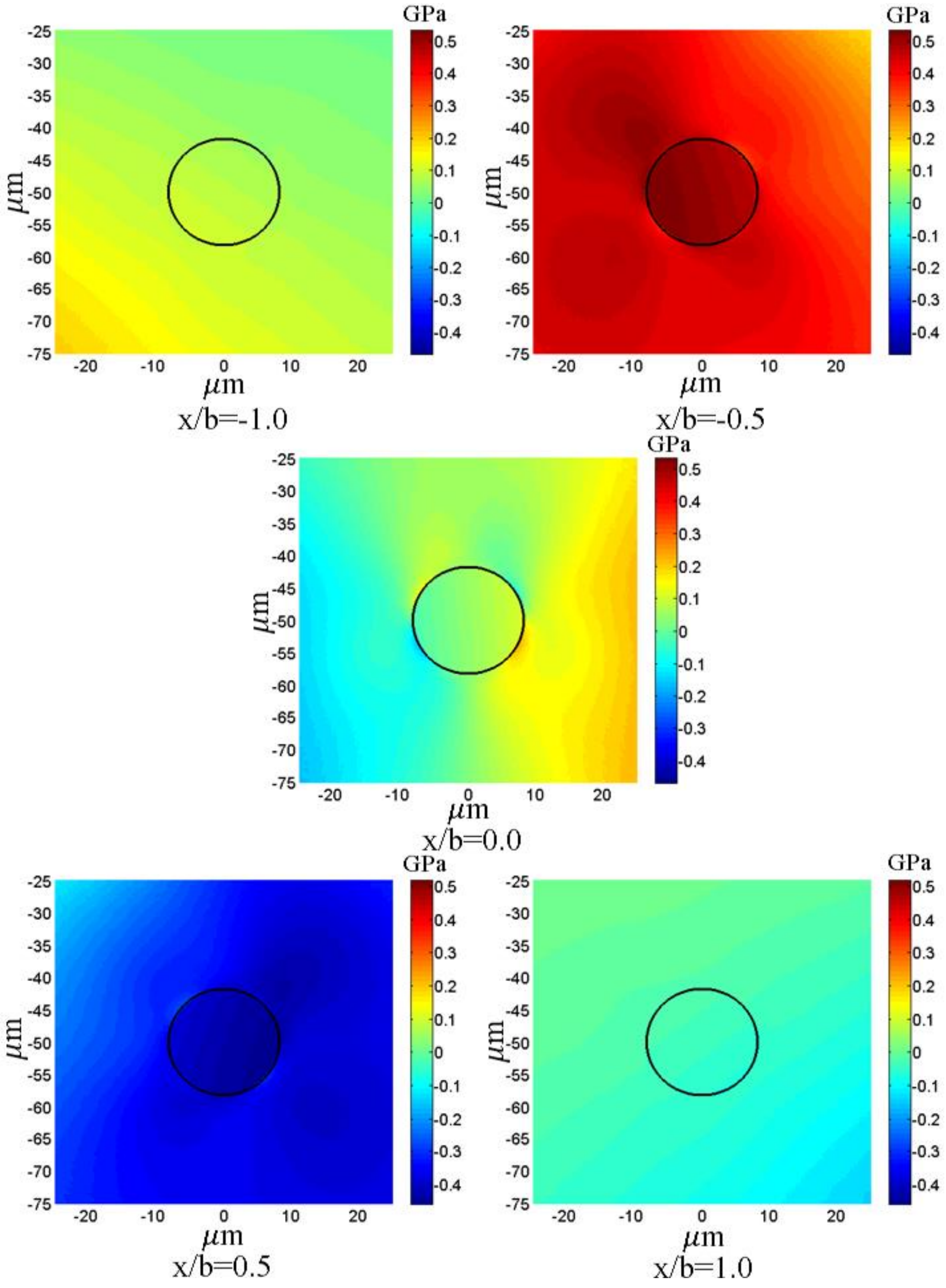

x/b=-1.0

x/b=-0.5

x/b=0.0

x/b=0.5

x/b=1.0

Figure 2.5. Shear stress variations around the inclusion as the Hertzian load passes over the surface. x/b indicates the relative location of the center of the Hertzian pressure distribution.

Figure 2.6 a illustrates the amplitude of variations experienced by each element in the RVE for a simulation without surface traction. Four regions of maximum alternating shear stress exist around the inclusion. As described earlier, direction of wing growth is observed to be a function of rolling direction. This indicates that surface traction due to contact may affect the internal stresses. However, Figure 2.6 b illustrates that surface traction does not change the shear stress amplitudes drastically.

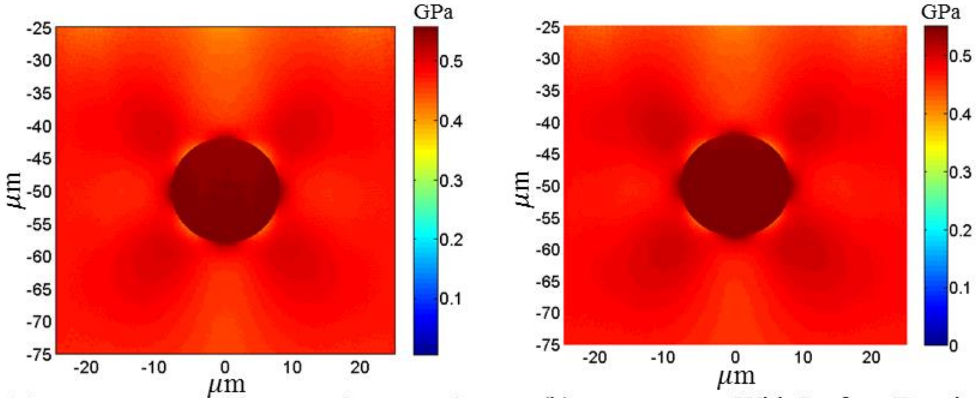

(a) $\tau_{alternating}$- Without Surface Traction (b) $\tau_{alternating}$- With Surface Traction

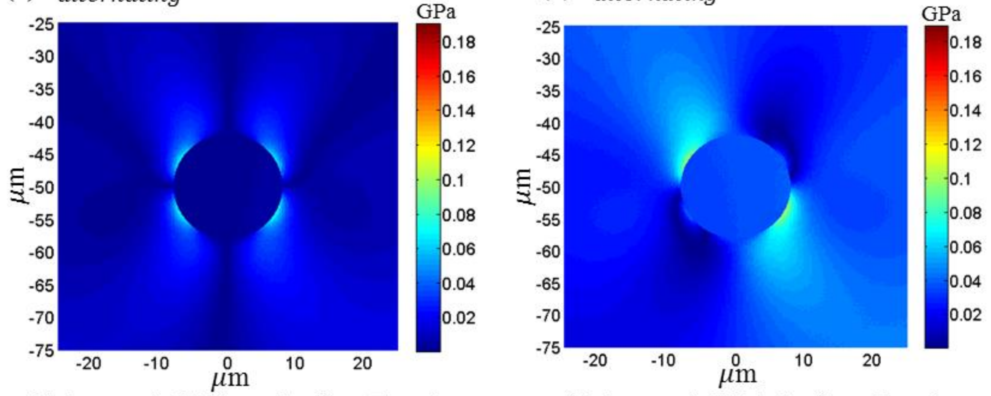

(c) $|\tau_{mean}|$- Without Surface Traction (d) $|\tau_{mean}|$- With Surface Traction

Figure 2.6. Effect of surface traction on amplitude and mean value of shear stress.

It should be noted that the direction of the surface traction is consistent throughout the 21 steps of the loading (always from left to right). Consequently, applying the superposition principle, it should affect the mean value of shear stress instead of the alternating amplitude. Figures 2.6c and 6d demonstrate this idea. As can be seen, due to introduction of surface traction to the domain, two regions are distinguishable as they experience higher values of mean shear stress. It should be noted that the absolute value of shear stress is taken into account, because the mean positive and negative shear stresses are equivalent in terms of damaging the material.

2.2.3 Damage Mechanics

As mentioned in the introduction, most of the research work available in the literature indicates that butterfly wings are regions of altered microstructure that has undergone a transformation from martensite to ferrite; however, the mechanism for this phase change is not known well. Although early research suggest that operating temperature of bearings might have an effect on wing formations, recent work shows that it is mostly a stress based phenomenon [72–74]. The current model employs a stress based approach using continuum damage mechanics to explain this phase change. Damage mechanics has been widely to investigate fatigue behavior of the material due to cyclic loading [70–73]. In this approach, the material degradation due to cyclic loading is taken into account by updating the constitutive relationship. For this purpose, a thermodynamic state variable referred to as damage, D, is introduced. Fatigue damage due to cyclic stresses manifests itself as a gradual evolution of this parameter. In this study fatigue damage accumulation is assumed to be representative of transformation by which martensite decays into ferrite during the cyclic loading of the material.

The updated constitutive relationship due to damage has the following form:

$$\sigma_{ij} = C_{ijkl}(I_{klmn} - D_{klmn})\varepsilon_{mn} \tag{2.1}$$

Where , C_{ijkl}, I_{klmn}, D_{klmn}, ε_{mn} are the stress, stiffness, identity, damage, and strain tensors respectively. For the case of isotropic material which is the assumption in this study, Eq. (2.1) can be simplified to

$$\sigma_{ij} = C_{ijkl}(1 - D)\varepsilon_{kl} \tag{2.2}$$

Modulus of elasticity of the damaged ferrite is assumed to be slightly less than parent martensite (10% lower) due to fatigue damage. Hence, the value of D progresses from 0 for pristine martensitic matrix to 0.1 for fully transformed ferritic phase. After the phase transformation is complete, no further damage is accumulated in the element assuming that there is not any secondary phase transformation. Also, damage is evolved only in the matrix elements and no damage is applied to the inclusion.

The damage evolution law used in this model is based on the equation proposed by Xiao [70]. According to Xiao [70], damage in material evolves during loading cycles with the following differential equation:

$$\frac{dD}{dN} = \left(\frac{\sigma}{\sigma_r(1 - D)}\right)^m \tag{2.3}$$

In the equation above, N indicates the number of loading cycles and is the stress component mainly responsible for the fatigue damage. σ_r and m are material depended parameters. σ_r is commonly known as resistance stress since it represents the material's ability to resist fatigue damage accumulation [70]. The stress component responsible for fatigue damage depends on the loading condition. For example, in a simple tensile fatigue test, as the failure mechanism is governed by the separation of the weak planes in the normal direction, the normal tensile stress is the dominant factor in crack initiation [73]. However, in torsion fatigue, cracks initiate at the maximum shear planes [71]. Butterfly formation is considered as a shear driven phenomenon; hence, shear stress is assumed to be the driving stress component effective on damage accumulation. As mentioned before, it seems that alternating shear stress has the main effect on butterfly formation while mean shear stress has a secondary effect to make two of the wings dominant. Considering the aforementioned observations, an approach similar to Goodman's equation is suggested that accounts for both the amplitude and mean value of shear stress. Figure 2.7 shows the value of $\tau_{alternating}$ +| τ_{mean} | after the first load pass over the RVE. So, the damage equation will have the following form:

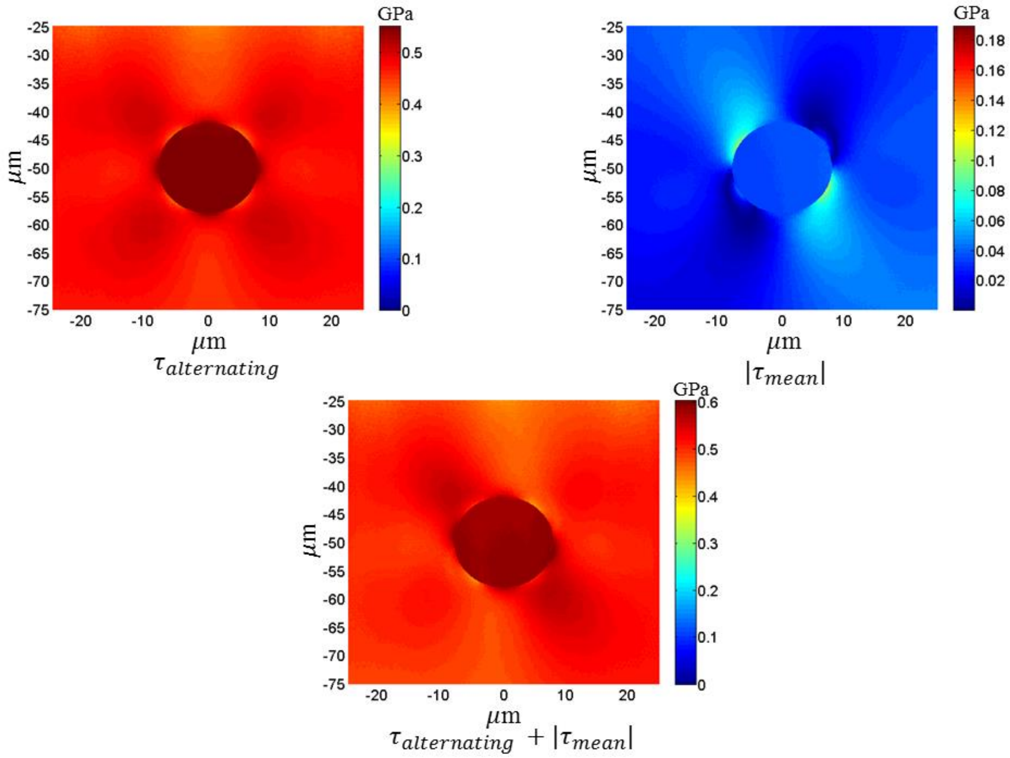

Figure 2.7. Shear stress amplitude, mean, and their summation during one load pass over pristine domain.

$$\frac{dD}{dN} = \left(\frac{\tau_{alternating} + |\tau_{mean}|}{\sigma_r(1-D)}\right)^m \tag{2.4}$$

Integrating Eq. (2.4) over damage from D=0.0 to D=D_c gives the number of cycles for butterfly appearance:

$$N_{appearance} = \frac{1}{m+1}\left(\frac{\sigma_r}{\tau_{alternating} + |\tau_{mean}|}\right)^m \tag{2.5}$$

Parameters σ_r, m, and b are material properties that are commonly obtainable by curve fitting Eq. (2.5) to S-N data obtained from fatigue experiments. Considering butterfly formation as a shear related phenomenon, S-N data for a shear dominated fatigue experiment would provide the closest analogy. For this purpose data for the experimental torsion fatigue tests by Shimizu [75] are implemented. The corresponding values of and m obtained from the curve fitting are 6.11 GPa and 10.0 respectively.

2.2.4 Model Application and Butterfly Progression

A model was developed to record all the stress components and damage evolution from the ABAQUS output data for all the elements during 21 loading steps. It is assumed that microstructural alteration occurs when the damage reaches the critical value of 0.1. Figure 2.8-a depicts the butterfly evolution in the chronological order for a 16 inclusion as the number of cycles increase. As shown, the microstructural transformation starts from the inclusion/matrix interface and then propagates along a direction which is 45 degrees from the over rolling direction. Figure 2.8-b illustrates the evolution process for all 21 steps at once using a color spectrum. The evolution procedure is in agreement with the results and procedure presented by Grabulov [45,46]. Figure 2. compares a sample pair of butterfly wings observed by Grabulov with the current simulation results. As can be seen, the shape of the butterflies and their orientation are in good agreement with the experimental observation.

2.3 Results and Discussion

2.3.1 Effect of Inclusion Depth

Few investigators have studied the effect of inclusion depth on butterfly initiation. Lund [76] studied the effect of maximum contact pressure on butterfly formation depth. His experiments showed that the maximum depth where butterflies form increases linearly with the maximum Hertzian contact stress. These observations strongly support the stress induced theories for butterfly formation. Unfortunately it is not possible to compare the given data with maximum alternating shear stress or maximum in-plane shear stress depth as Lund [76] does not provide the information about the width of Hertzian contact. Grabulov [5,45,46] classifies the butterflies into three main categories based on the depth where they occur: i) Butterfly progression zone: which is from the contact surface to almost 1.5b, at this range butterflies are fully formed. ii) Embryonic butterfly zone: from 1.1b to about 6b in depth, in this region butterflies form but their formation stops without the cracks growing beyond the wings. iii) Unaffected zone: deeper than 8b, where butterflies do not form. This classification also supports the role of alternating shear stresses on butterfly formation. In this investigation, the model was used to determine the effects of an inclusion at different depths and corroborate with the experimental results of Evans et al [27]. It should be noted that to make the simulation conditions as close as possible to the experiments, a 2 μm inclusion was considered in this part of investigation.

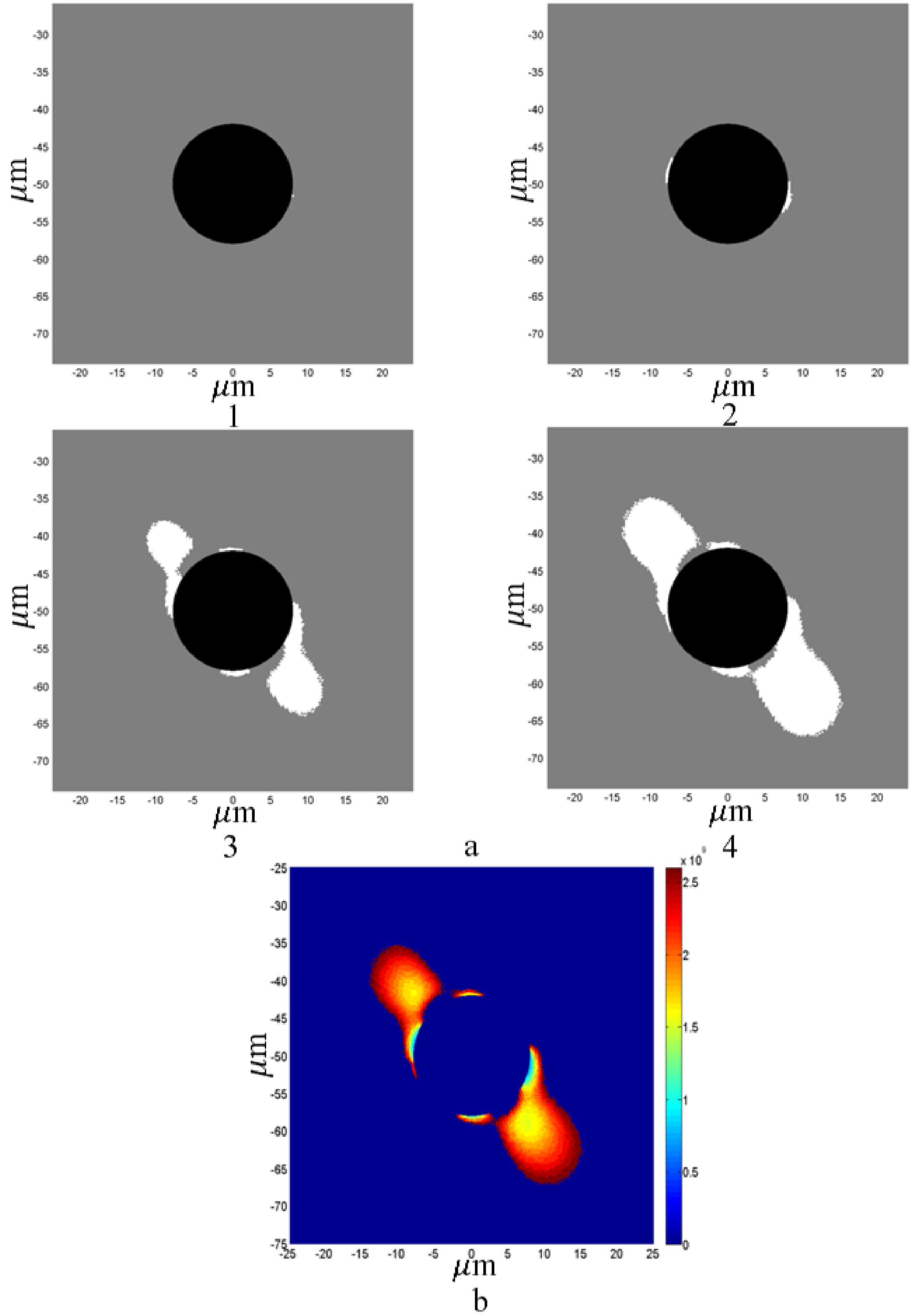

Figure 2.8. a) Chronological order in butterfly evolution: 1) beginning of the microstructural change 2) microstructural alteration near the inclusion/ matrix interface 3) formation of the actual body of the wings 4) fully formed butterfly wings b) Color spectrum showing the butterfly evolution versus number of cycles (Pmax= 2.0 GPa).

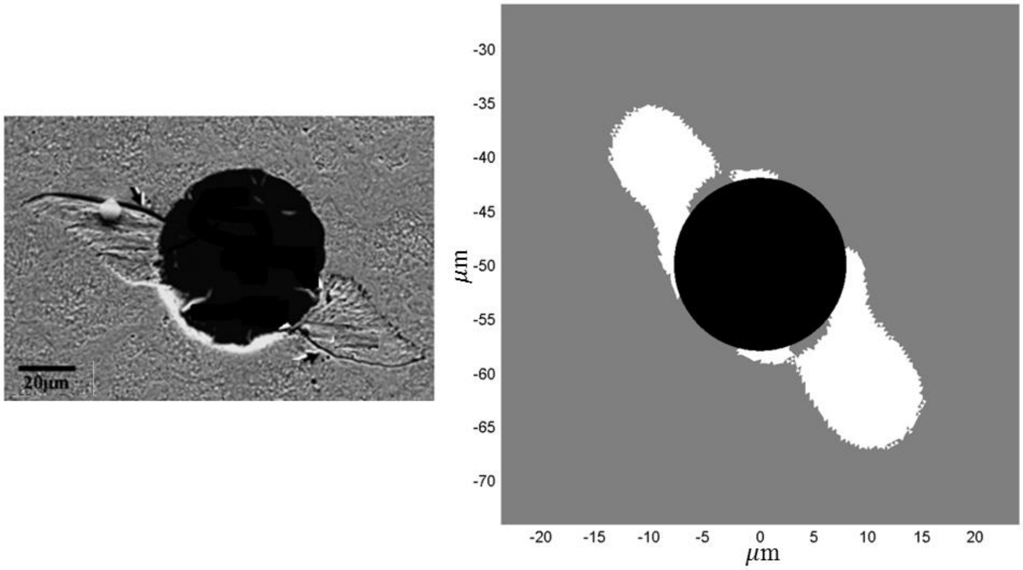

a

b

Figure 2.9. Butterfly wings formed around an inclusion (a) as observed by Grabulov [5] (b) as predicted by the model. (Figure on left is flipped as opposed to the original to set the over rolling direction consistent with the simulation).

Figure 2.10 illustrates the experimental and the results obtained from the current model. Butterflies which are located near the maximum alternating shear stress depth (from 0.2b to 0.8b) commonly have two wings propagated from the sides, but the wing which is closer to the maximum alternating shear stress depth (0.5b) is larger. Consequently, from 0.2b to 0.5b, the lower wing is more developed and from 0.5b to 0.8b, the upper wing is larger. Also, when the inclusion is located at greater depths (such as 1.1 b), as the effect of mean stresses due to surface traction diminishes, the alternating shear stress will be even more dominant. Hence, a secondary wing appears on top of the inclusion where the alternating shear stresses have a higher value compared to the bottom of the inclusion. This confirms the idea of maximum alternating shear stress as the primary factor and the mean shear stress as the secondary factor in butterfly formation. The model developed for this investigation successfully predicts that the wings closer to the maximum alternating shear stress depth propagate more when the inclusion is located at intermediate depths. Moreover, for the deep inclusions the direction and location of the third wing is in agreement with the experimental observation.

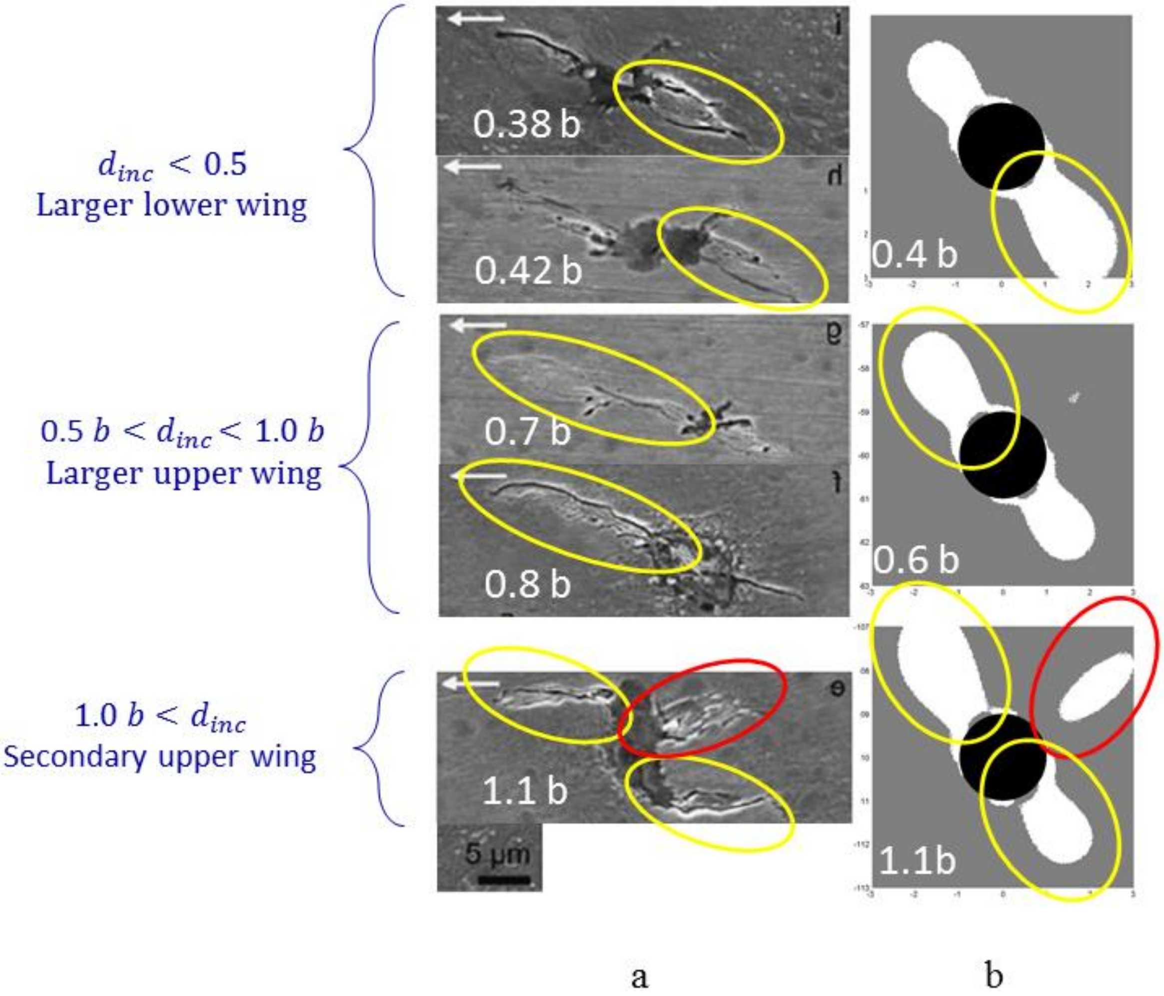

Figure 2.10. Effect of inclusion depth on butterfly wing development: (a) as observed by Evans [27] (b) as predicted by the model. (Some of the figures on left are flipped as opposed to the original to set the over rolling direction consistent with the simulation).

2.3.2 Butterfly Wingspan

Among the many investigators who have studied butterfly formation, few have paid close attention to the butterfly wing size. Lund [76] presents the results of more than 1000 observations on butterfly wing size. In his samples, the inclusions size varies from 5 μm to about 30 μm in diameter with the majority of them lying between 10 to 20 μm. Wing sizes change from 5 μm to more than 40 μm in length with the majority of them being about 20 μm. He provides the accumulative distribution function for both inclusion size and butterfly wing size. But, he does not indicate relative wing span to inclusion size relationship. So, it is not possible to conclude how the wing span development is affected by the inclusion size. Lewis and Tomkins [11] listed the butterfly wing spans compared to inclusion sizes. Their results are compared with the current simulation results.

Figure 2.11 shows the butterfly wing formation around two different inclusions, one 16 μm in diameter and the other 2 μm in diameter. Figure 2.11 illustrates that for the smaller inclusion, the wingspan length is shorter, but the ratio of the wingspan to inclusion diameter is larger. This trend is similar to what Lewis and Tomkins [11] observed.

Figure 2.12 compares the results obtained from the current model for wingspan to inclusion ratio of different inclusion sizes at different depths with the experimental results from the aforementioned studies. The results indicate that both studies follow a similar trend; the results obtained from this investigation lie between the upper and lower bounds of the experimental results.

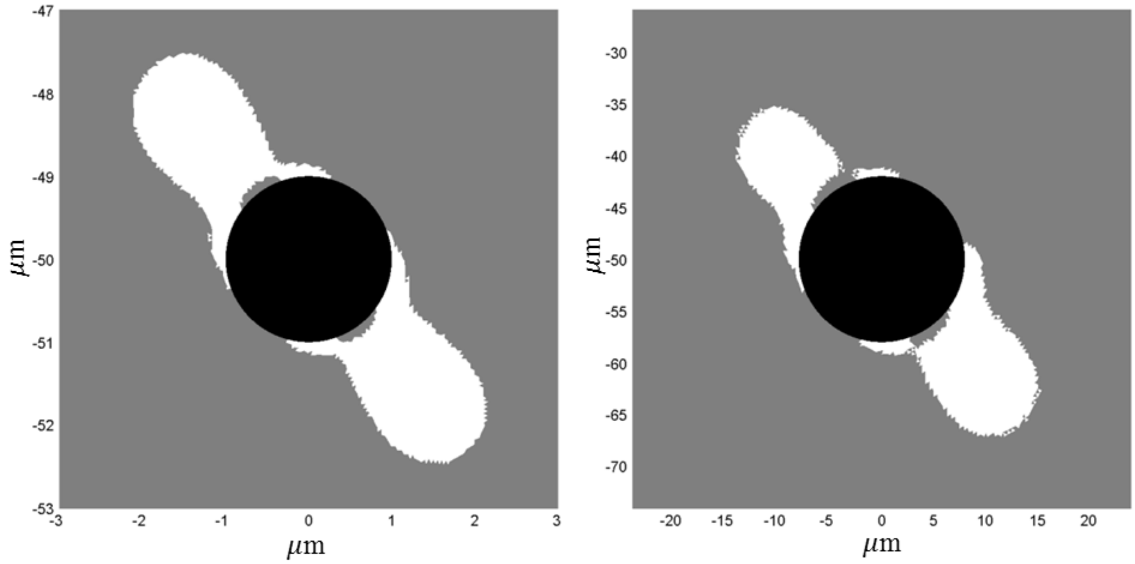

a

b

Figure 2.11. Butterfly wings formed around (a) 2 and (b) 16 inclusions. Note that the relative wingspan to inclusion size is larger for the smaller inclusion.

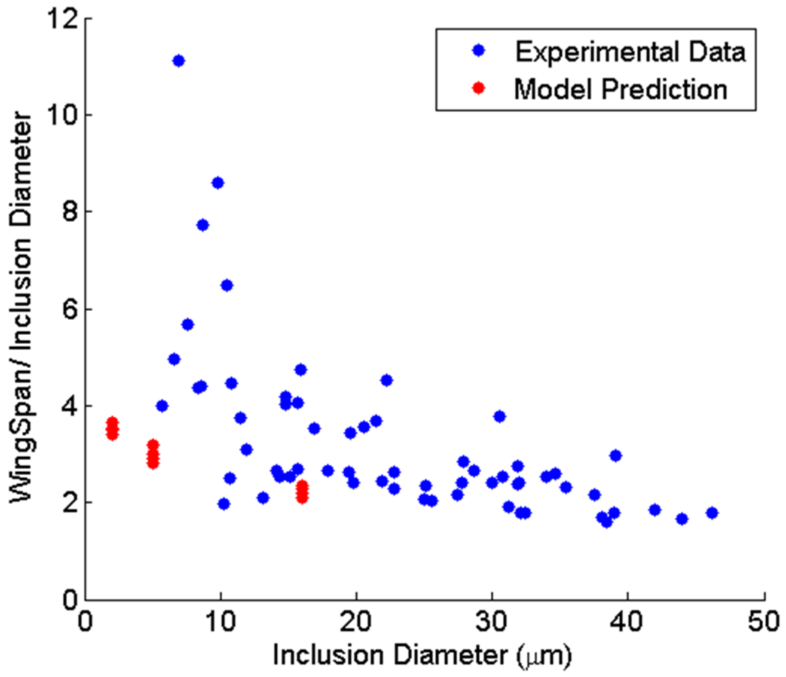

Figure 2.12. Wingspan to inclusion diameter ratio versus the inclusion size variation according to experimental observations [11] and current model.

2.3.3 Life Prediction

One of the most important concerns is to know when they appear in a bearing life cycle. It should be noted that it is very hard to obtain an exact estimation of when butterflies appear because they form well in advance to final failure. Different investigators have suggested different estimations of the number of cycles needed for butterfly formation. This number varies from 10^1 [42] to 10^3 [39] of L_{10} life. The problem is that current experimental methods cannot determine how many cycles were required to form a butterfly; only that they do or do not exist after a number of rolling contact cycles. Takemura et al. [36] used the information collected from over 400 tests to estimate the threshold for butterfly formation.

The current model was used to investigate the effects of different load levels on butterfly formation and to compare the results with those suggested by Takemura. As most of the inclusions observed by Takemura are less than 5 μm in diameter, a 2 μm inclusion is simulated to provide a better basis for comparison. Figure 2. provides a comparison of the fully formed butterfly wings around a 2 μm inclusion at t Hertzian load levels of 2.0, 3.0, and 4.0 GPa. The color spectrum indicates the number of cycles taken for each element to reach the critical level of damage associated with a completed transformation from martensite to ferrite. It can be seen that while the butterfly shapes is not a function of load, the number of cycles is drastically decreasing as the load increases. In the next step the PlotDigitizer [77] software is implemented to extract the experimental data from

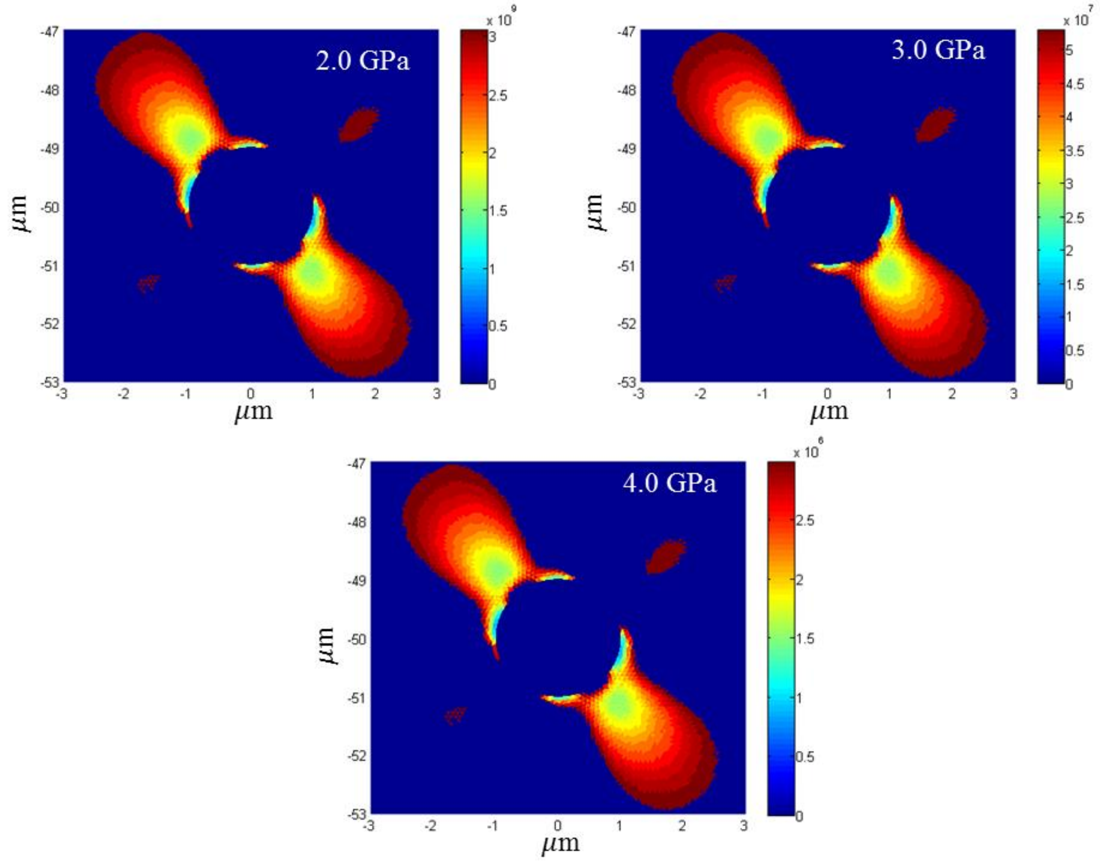

Figure 2.13. Color Spectrums illustrating butterfly formation growth versus number of cycles at different load levels.

Takemura [36]; then a power law curve fit is used to determine the trend for data. The curve fit is compared to the butterfly initiation prediction by the current model in Figure 2.. It can be seen that the model is capable of predicting the butterfly formation life in all the load ranges well. The results are particularly matching the experimental records at about 2.0 GPa which is the typical maximum Hertzian pressure at which wind turbine bearings operate. It should be noted that the damage evolution law used in this paper is calibrated from torsion fatigue tests [75]. The matching results support the idea of using a torsion fatigue as an analogy to RCF phenomena [72,78].

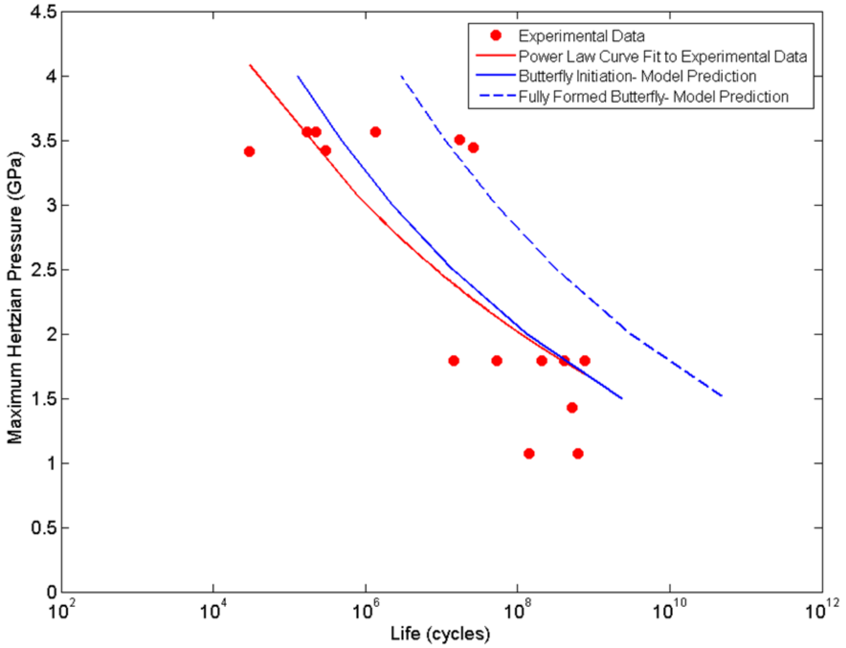

Figure 2.14. S-N curve for butterfly formation. Experimental data are extracted from [36].

2.3.4 Inclusion/Matrix Debonding Regions

Inclusion/Matrix bonds are found to have an effect on butterfly formation [5]. Debonded regions induce local rubbing between inclusion and matrix culminating in nano-scale rubbing damage due to shear stresses [41,44]. Graboluv [5] experimentally located the debonded regions in matrix/inclusion interface for a circular Al2O3 inclusion. According to his results debonding occurs due to accumulation of plastic shear damage at the boundaries. Thus, the current model is employed to predict the most vulnerable regions around the inclusion/matrix interface where debonding may occur.

Considering the maximum shear stress along the interface as the critical factor that causes the debonding, 2D stress transformation equations are used to resolve the stresses along the inclusion/matrix interface in each step, as illustrated in Figure. Maximum value of shear stress along the interface which is experienced by each element on the interface is calculated during one complete load pass. Figure compares the experimental observations with the results obtained from the current model. Figurea shows the deformation and debonding regions around an inclusion investigated by Grabulov [5]. Figureb shows the maximum shear stress in a cylindrical coordinates system centered at the inclusion center for a 16 μm inclusion while the maximum Hertzian contact is 2.0 GPa. The regions of maximum shear stress on the inclusion/matrix interface indicate the most detrimental regions for debonding. As can be seen, these regions closely match what Grabulov has observed experimentally for debonded regions. It should be noted that even for a relatively low value of Hertzian pressure the maximum shear stress is near the threshold for plastic shear deformation. This confirms Grabulov's idea of debonding due to plastic shear deformation at the inclusion/matrix interface.

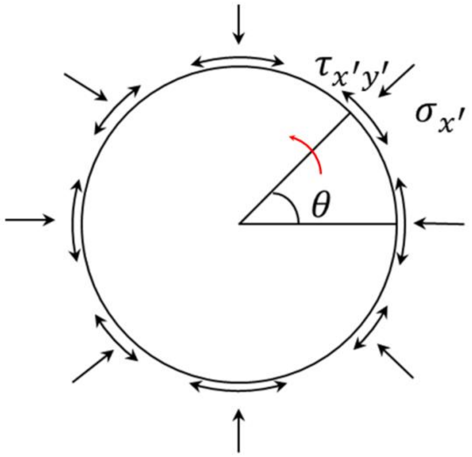

Figure 2.15. Schematic showing the stresses resolved along the inclusion matrix interface. Maximum shear along the interface dominates the debonding.

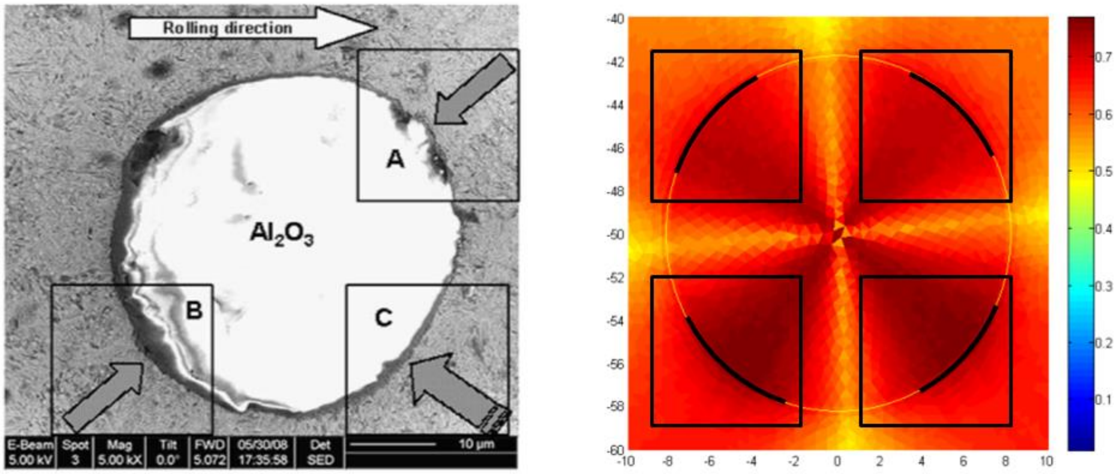

a b

Figure 2.16. Comparison of the debonding and deformation regions at inclusion/ matrix interface (a) as observed by Grabulov (b) Simulation results.

2.3.5 Crack Initiation

In most of the cases where the inclusion has a simple circular shape and regular butterfly forms around it, one major crack is observed in each wing. Such cracks are detectable in the butterfly wings shown in Figure 2.-a. These cracks occur mostly on top edge of upper wing and bottom edge of lower wing. They normally appear on the butterfly/matrix interface. Evans [41] has noticed this fact and has specifically studied it by serial sectioning of a butterfly wing [27]. He suggests that microstructural alteration causes formation of micro cavities. Coalescence of these voids generates the cracks. Mode I loading is known to dominate the propagation of these cracks at the inclusion vicinity. Lewis and Tomkins [11] has paid close attention to crack growth at butterflies. They also propose that Mode I loading is the dominant factor for crack growth near the butterfly; however, if the crack propagates further, Mode II & III loading will govern its propagation.

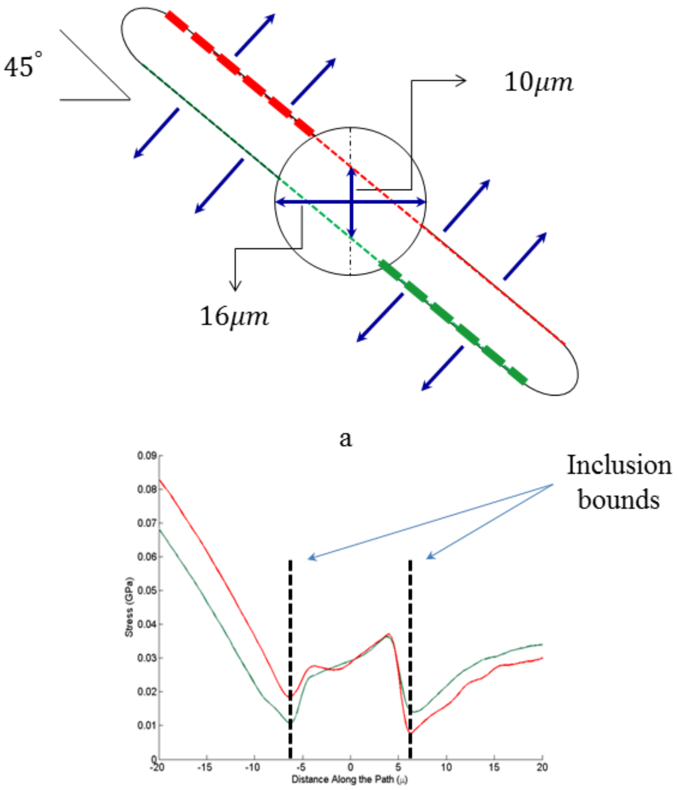

a

b

Figure 2.17. Maximum tensile stress acting on butterfly/ matrix interface. Bold dashed lines show where the model predicts the cracks to grow.

The current model is employed to study if it can explain this phenomenon. Assuming that a typical butterfly grows at 45 degrees, all the stresses are resolved at 45 degrees using 2D stress transformation equations. Then, the maximum tensile stress that each element experiences during 21 loading steps is recorded as it represents the critical stress component for Mode I crack propagation. It is assumed that the cracks initiate on one of the two edges of each wing. So, the maximum Mode I loading is compared at two paths angled at 45 degrees which represent two edges of a typical wing. Figure -a illustrates the lines along which the stresses are recorded, and the results are plotted in Figure -b. Figure demonstrates, Mode I loading has a higher value at the top of the upper wing and bottom of the lower wing. This can explain why the cracks appear in this certain pattern.

2.4 Summary and Conclusions

This paper presents a new model to simulate microstructural changes around non-metallic inclusions in bearing steel which are commonly referred to as "butterfly wings". A 2D FEM model is developed with constant strain elements and plane strain assumptions to model a domain with an embedded inclusion which is subjected to cyclic Hertzian loading. Stress analysis of steel matrix at the vicinity of the inclusion shows that both shear stress reversal and mean shear stress due to presence of surface traction play a major role in wing formation. It is hypothesized that shear stress reversal is the primary driving factor for wing formation while mean shear stress functions as the secondary factor and determines the orientation of the butterflies. Continuum damage mechanics is used to introduce a new damage evolution law which considers both the effect of amplitude and mean value of shear stress to model fatigue damage and microstructural alterations. Damage evolution throughout the cycles is coupled with the FEM simulation using jump-in-cycles technique. The model predicts the butterfly shape and orientation successfully. Effect of inclusion depth and size on wing formation is studied. Also, the model is implemented to predict the wing formation versus load and time to obtain the S-N curve. The stress solution is implemented to predict potential debonding regions on inclusion/matrix interface and possible locations for crack growth on butterfly/ matrix interface. In all the cases, the results correlate well with experimental data available in the open literature.

CHAPTER 3. EFFECT OF NON- METALLIC INCLUSIONS ON BUTTERFLY WING INITIATION, CRACK FORMATION, AND SPALL GEOMETRY IN BEARING STEELS

3.1 Introduction

Ball and rolling element bearings are crucial parts of all machinery which have rotary and relative motion. Because of their geometry, these elements usually function under large stresses. Bearings can fail because of environmental debris, improper lubrication systems, excessive loading, or bad installation. If a bearing is properly installed and maintained, the main mode of failure will be due to material fatigue. It has been observed that a loaded rotating element has a limited life because of the probability of the surface or subsurface initiated fatigue damage. Failure due to this phenomenon is commonly referred to as rolling contact fatigue (RCF).

In general, rolling contact fatigue happens due to two different phenomena: surface originated pitting and subsurface originated spalling [35]. Figure 3.1 shows two typical cracks due to surface and subsurface failure. As can be seen, the depths at which the cracks initiate are different. Hence, these two phenomena commonly can act separately; however, they might interfere in the propagation stage and cooperate to fail the material. While surface initiated fatigue can be hindered by employing better lubricants and more efficient lubrication techniques, there are not actually many ways to stop subsurface initiated fatigue after the bearing is manufactured and installed. So, it is important to understand the mechanisms leading to this type of failure in order to improve the bearing design and manufacturing process.

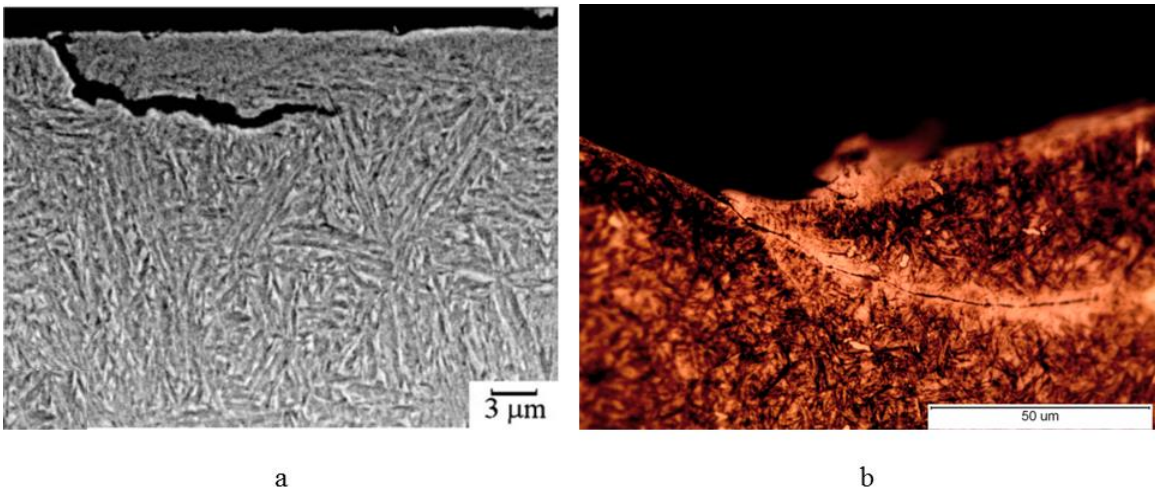

Figure 3.1. Failure due to surface pitting (a)[61] as opposed to subsurface spalling (b) (note the depth of the cracks).

Subsurface cracks mostly occur at stress concentration sites such as material defects, voids, and non-metallic inclusions [79]. Non-metallic inclusions are byproducts of steel manufacturing process and can cause stress concentrations in the matrix due to different material properties. Many researchers have investigated the effect of inclusions on fatigue crack initiation in hardened bearing steels. These works can generally be divided into experimental and analytical research.

Experimental investigation of fatigue crack initiation in bearing steels has mostly been conducted in two main categories: uniaxial tensile fatigue tests [51,79–83] and RCF tests with a set up similar to actual bearings, i.e. with rolling elements [56,84–87]. Uniaxial fatigue tests have their own pros and cons. The advantage of such tests is that a large volume of material (including many inclusions) is subjected to the critical stress level, so the failure is almost always due to the presence of the inclusion, and it is easy to spot the initiation point due to fish-eye phenomenon. However, there is an issue with this approach. In uniaxial tests, the failure is due to tensile loading, but RCF occurs due to reversal of shear stress [35]. As can be observed in Figure 3.2 for a point located at 0.5b, shear stress is the only stress component which experiences a reversal during each load pass. So, the crack initiation and development mechanisms as well as fatigue life assessment with uniaxial fatigue tests may be inaccurate. As a new approach, some researchers [71,75] have recently used torsion fatigue as an analogy to RCF because the failure is shear dominated in both cases. However, in torsion fatigue tests only the outer layer of the shaft is subjected to the critical shear stress value and the probability of crack initiation due to inclusions and defects is less. Tests on rolling elements have been conducted by a number of investigators [5,41,44,45,88] and many more to study the effect of inclusions on RCF. The drawback of current test set up is that crack initiation is hard to detect as it occurs in subsurface of the material. Moreover, it is hard to find an exact correlation between the inclusion presence and final failure, because in most cases, the inclusion itself is removed from the matrix with the spall. Recently, non-destructive methods such as ultrasonic detection [57,62,80,89,90] have provided the ability to detect inclusions and monitor the crack development inside the material before the failure.

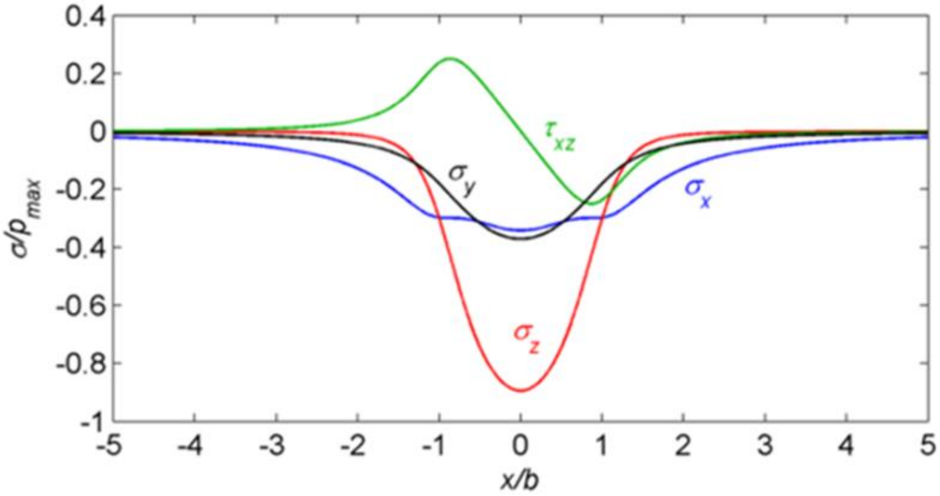

Figure 3.2. Stress history for a point located at 0.5b as a function of distance from the center of a moving Hertzian contact.

It has been frequently observed that crack initiation in the vicinity of inclusions is accompanied by microstructural changes which are commonly referred to as “butterfly wings”. In these regions, the material microstructure alters from martensite to ultrafine ferritic grains [42,43]. A butterfly formation can serve as a crack initiation site which may culminate in the final failure. Experiments suggest that after the wing formation, cracks commonly form on top of the upper wing and bottom of the lower wing as shown in Figure 3.3 in a pair of typical butterfly wings [41,46]. Despite the extensive amount of experimental research on butterflies, there are very few models suggested for butterfly wing formation. In 1992, Salehizadeh and Saka [91] used an elastic-linear plastic model to calculate residual stress evolution around a circular inclusion. In 1996, Melander [65–67,92] used fracture mechanics to investigate the propagation of cracks that were already initiated adjacent to the inclusions. Two years later, Vincent et al. [64], suggested that accumulation of dislocations can be a potential reason for wing formation. Recently, Alley et al. [63] investigated the effect of plastic strains around the inclusion to explain the problem. Finally, Mobasher Moghaddam et al. [93] used damage mechanics with a focus on the effect of mean stress to model butterfly wing formation, orientation, direction, and butterfly initiation life.

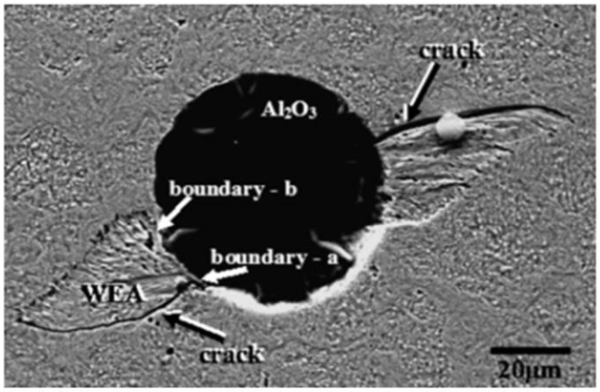

Figure 3.3. SEM image of a pair of butterfly wings formed around Al_2O_3 inclusion as observed by. The cracks are visible on top of the upper wing and bottom of the lower wing [5].

Crack propagation beyond the butterflies has been modeled using linear elastic fracture mechanics (LEFM) [11]; however this method is not capable of explaining crack initiation. Raje et al. used discrete element method (DEM) [94] combined with damage mechanics [95] to predict RCF life. They used Voronoi tessellations to capture the effect of microstructural randomness of the material in RCF. Jalalahmadi and Sadeghi [96], extended the approach to FEM. They, in particular, studied the effect of inclusions on fatigue crack initiation [35]. Warhadpande et al. extended the model to include the effect of plasticity [97]. Weinzapfel et al. [98,99] developed a 3D model and used damage mechanics to model both crack initiation and propagation. Finally, Bomidi et al. [72] studied the effect of plasticity on subsurface damage, initiation and propagation life. Slack and Sadeghi [100] used the “kill element” approach to capture stress concentrations due to crack formation and void coalescence in the material to model spall geometries in the material. This approach is implemented in the current study as well to model intergranular crack propagation.

The current work studies spall formation from inclusions in bearing steel using damage mechanics by focusing on the effect of butterfly wings on crack initiation. The critical damage value within the butterfly wings is measured experimentally and used in the simulation. Effects of inclusion depth, stiffness and size on RCF life are investigated. To capture the microstructural randomness of the material, Voronoi tessellations are used to generate the computational domains. Weibull plots are employed to study the scatter in fatigue lives. Finally crack maps are compared with the experimental spall geometries. The comparison shows a close resemblance between experimental and simulated spalls.

3.2 Modeling Approach

3.2.1 Finite Element Model Set Up

A 2D FEM is developed with plane strain assumption. For this purpose commercially available software ABAQUS is used. Constant strain elements (CST) are implemented to form a semi-infinite domain which is subjected to a moving Hertzian contact. To model the contact, a Hertzian pressure profile is applied to the surface by a user defined subroutine UTRACLOAD. The half width of the contact is set to 100 μ and the Hertzian pressure profile is moved over the surface in 21 discrete steps from -200μ to +200μ (from –2b to +2b) while applying a surface friction coefficient of 0.05. The dimensions of the domain are 700μ in depth and 1000μ in length and the stiffness of the matrix is 200 GPa. The representative volume element (RVE) extends from –b to b along the rolling direction and from 0 to –b into the depth. These dimensions are similar to what Jalalahmadi [35] identified to be sufficient for a 2D model in an earlier study. A circular non-metallic inclusion is located at the centerline of the domain. The stiffness, size, and depth of the inclusion are varied for different scenarios, but the rest of the parameters are constant for all the simulation scenarios.

As described earlier, to capture the effect of microstructural randomness in the domain, Voronoi tessellations are used to model the material grains. The average grain size is set to 10μ to represent the martensitic microstructure observed in commonly used bearing steels. Jalalahmadi et al. [35] have shown that for 10μ grain size, 5μ CST elements will provide enough resolution for the stress solution. However in the current study a much finer mesh size is required for two reasons: (i) A very fine mesh size is required in the vicinity of the inclusion to capture the large stress gradients as accurately as possible, (ii) As will be discussed in the following sections, current study employs an approach known as “kill element” to model cracks. In this approach, cracks are modeled by coalescence of micro voids, and micro voids are represented with elements of zero stiffness. Consequently, to model the reality as close as possible, the mesh size should be reduced to a computationally reasonable extent. For this purpose the mesh size is selected to be 0.5μ throughout the RVE. With such a mesh size, it was possible to simulate more than 100 computational load passes in 24 hours. The triangular mesh is generated using the Triangle code [101] combined with an in-house code for Voronoi generation using a MATLAB preprocessor. Element size gradually increases at points farther away from the RVE and closer to the boundaries of the model.

3.2.2 Theory

As discussed earlier, RCF is known to be a shear driven phenomenon [1]. Different models have already been proposed to predict the fatigue behavior of rolling element bearings. The current model uses a stress-based approach employing continuum damage mechanics to explain this phenomenon. Damage mechanics has been widely used to investigate behavior of the material due to fatigue loading [69,73,102]. In this approach, the material degradation due to cyclic fatigue loading is simulated by updating the constitutive relationship. For this purpose, a thermodynamic state variable referred to as damage, D, is introduced in the domain such that each element of the material has a certain and constant damage value during each loading cycle. Fatigue damage due to cyclic stresses manifests itself as a gradual evolution of this parameter.

The updated constitutive relationship due to damage has the following general form:

$$\sigma_{ij} = C_{ijkl}(I_{klmn} - D_{klmn})\varepsilon_{mn} \tag{3.1}$$

Where , C_{ijkl}, I_{klmn}, D_{klmn}, ε_{mn} are the stress, stiffness, identity, damage, and strain tensors respectively. For the case of isotropic material which is the assumption in this study, Eq. (3.1) can be simplified to

$$\sigma_{ij} = C_{ijkl}(1 - D)\varepsilon_{kl} \tag{3.2}$$

The damage progression law used in this model is based upon the equation suggested by Xiao [70]. According to Xiao, damage in the material evolves due to cyclic loading by:

$$\frac{dD}{dN} = \left(\frac{\sigma}{\sigma_r(1 - D)}\right)^m \tag{3.3}$$

In the equation above, N indicates the number of loading cycles and is the stress component that mainly causes the fatigue damage. σ_r and m are material depended constants. σ_r is commonly known as resistance stress since it represents the material's ability to resist fatigue damage accumulation. The stress component responsible for fatigue damage depends on the loading condition and can vary from case to case. The damage evolution law for this study is the same as what has been used in an earlier study [93] which focuses on the effect of alternating and mean value of shear stress during each load cycle. The damage equation used in this investigation has the following form:

$$\frac{dD}{dN} = \left(\frac{\tau_{alternating} + |\tau_{mean}|}{\sigma_r(1-D)}\right)^m \tag{3.4}$$

Parameters σ_r, m, and b are material properties that are determined by curve fitting S-N data obtained from fatigue experiments. Detailed information regarding how this equation is derived and how it is calibrated is presented in reference [93] and is not repeated here. Eq. (3.4) is used both to define butterfly appearance and crack formation. Therefore, two critical damage values are required: (i) Dc-Butterfly which represents the threshold for martensite to ferrite alteration, and (ii) Dc-Crack which defines the crack formation inside the steel matrix. As the current model uses the kill element approach, the cracks are modeled by microvoid coalescence. Setting Dc-Crack equal to 1.0 can represent a void because it indicates that the stiffness value of the element is zero according to Eq. (3.2), and zero stiffness corresponds to a microvoid in the material [97,100]. However, finding the Dc-Butterfly is more involved as butterflies are mainly ultrafine ferrite grains [41] and not microvoids. For this purpose the critical damage inside the butterflies is measured experimentally and is found to be about 0.1. The details of this measurement are discussed later.

3.2.3 Model Application to Butterfly & Crack Progression

The stress tensor from the ABAQUS was recorded for all of the elements during the 21 loading steps. After each pass of Hertzian pressure, a MATLAB post processor updates the damage in the elements of the matrix which are located in the RVE. The new damage values are then used to update the constitutive relationship of the material during the next rolling contact cycle The model is simulated until the damage value in one of the elements in the RVE reaches Dc-Butterfly. This is recorded as the butterfly formation life. Then damage evolution is continued until the first element passes Dc-Crack. At this point, the collection of elements in the matrix which have a damage value equal to or bigger than Dc-Butterfly are classified as microstructurally altered material that constitutes the butterfly wings. It should be noted that at this stage the butterfly progression is stopped in the model. This is an assumption consistent with most of the experimental observations that suggest cracks can propagate without further butterfly expansion [103]. However, it should be noted that in few cases it has been observed that butterflies wings keep expanding till final failure as shown in Figure 3.4 as observed by [103,104].

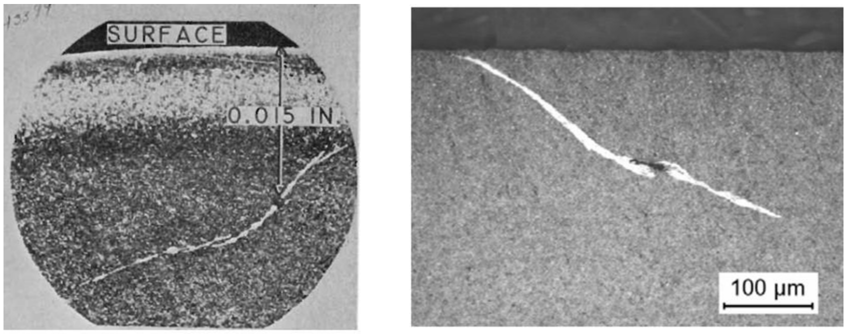

a

b

Figure 3.4. Examples of butterfly wings extended beyond the inclusion vicinity as observed by Carter et al. (a) [103] and cited by Gegner [104] (b).

After the first element reaches the Dc-Crack, the cracks keep propagating using the kill element approach till at least one crack reaches the surface. This phenomenon is assumed to be final failure and the total number of cycles for this to happen is recorded as fatigue failure life. The crack propagation is assumed to be intergranular similar to [78]. In this assumption, the grain boundaries are considered to be the weak planes of the materials.

Figure 3.5 depicts the algorithm used for damage evolution in each grain. As shown in Figure 3.5-a, during each loading step, shear stresses are resolved along all sides of a Voronoi cell. The alternating and mean shear stress on each boundary element is recorded. Then, for all the elements located in each sector of the cell, damage is updated by calculating the maximum damage evolution rate at the boundary elements of that particular sector of the Voronoi cell as illustrated in Figure 3.5-b. In this figure, all the regions with the same color have the same damage value. Finally, once damage reaches the Dc-Crack for at least one element in one side, it will remain at Dc-Crack, for the elements on the boundary of that Voronoi side and for the rest of the elements in the same sector of the Voronoi, damage is set back to zero because the cracks are already represented in the Voronoi cell by killing the boundary elements. The status of a failed Voronoi is depicted in Figure 3.5-c.

Figure 3.6 depicts the chronological sequence of spall formation in a sample domain from beginning till final failure. As can be seen, in the first step, butterfly wings start to propagate around the inclusion (Figure 3.6-a).

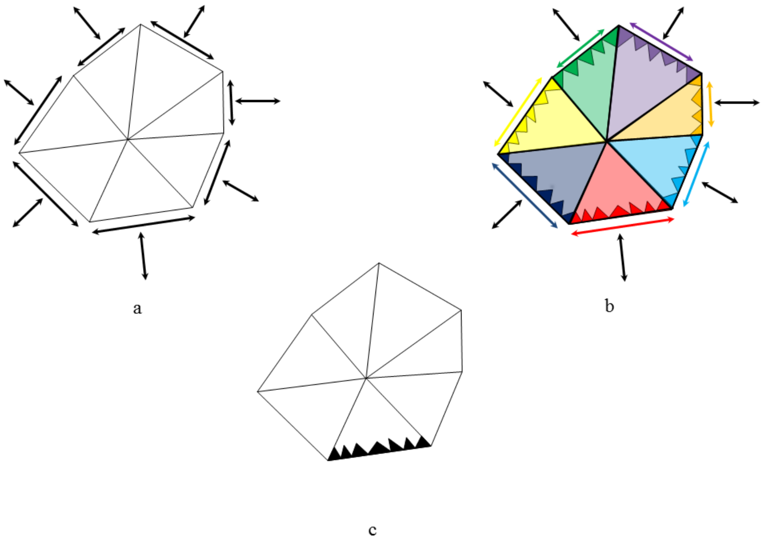

Figure 3.5. Schematic description of kill element approach: a) stresses are resolved along the grain boundaries. b) The maximum value of damage for the boundary elements is given to all elements to that particular side of the Voronoi. c) The boundary elements which reach the critical damage value are killed.

In the next step, the cracks initiate in the vicinity of the inclusion (Figure 3.6-b). These cracks propagate towards the surface (Figure 3.6-c), culminating in final failure by reaching the surface (Figure 3.6-d).

3.3 Experimental Measurement of Dc-Butterfly

As discussed in the previous section, when employing the kill element approach, it is important to use a reasonable approximation for $D_{c\text{-Crack}}$ and $D_{c\text{-Butterfly}}$ values. $D_{c\text{-Butterfly}}$ can be obtained by finding the modulus of elasticity of the damaged ferrite grains within the butterfly. Eq. (3.2) can be rewritten as:

$$\sigma_{ij} = C_{ijkl}{}^{*}\varepsilon_{kl} \tag{3.5}$$

where

$$C_{ijkl}^{*} = C_{ijkl}\,(1 - D) \tag{3.6}$$

For the material inside a butterfly wing in a 2D plane strain condition this can be simplified to:

$$E_{Butterfly} = E_{Steel}(1 - D_{c-Butterfly}) \tag{3.7}$$

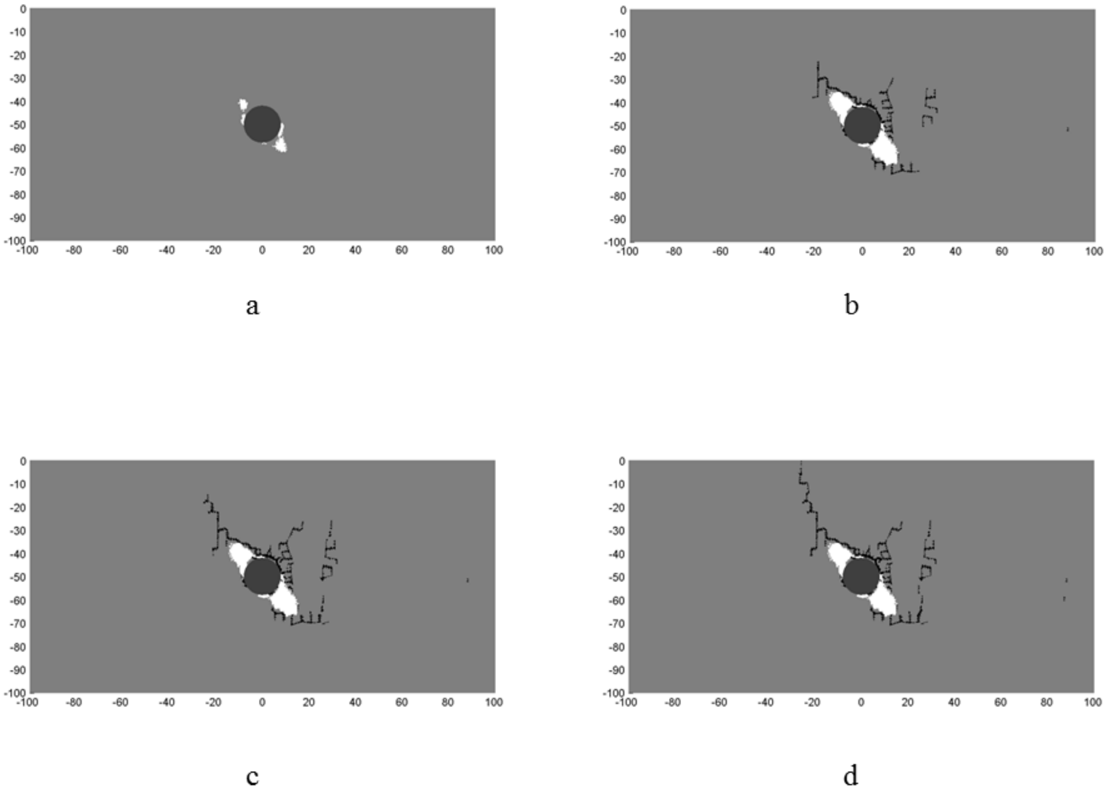

a

b

c

d

Figure 3.6. Four stages of RCF failure due to inclusion presence: a) Butterfly formation. b) Crack initiation on butterfly/ matrix interface. c) Crack propagation towards the surface. d) Final failure as the crack reaches the surface.

Rewriting Eq. (3.7), gives:

$$D_{c-Butterfly} = 1 - \frac{E_{Butterfly}}{E_{Steel}} \tag{3.8}$$

To find the modulus of elasticity of butterflies, RCF tests were run on a 3 ball & rod RCF test rig. The test rig is shown in Figure 3.7-a. The schematic of the contact between the balls and the rod-shaped specimen is illustrated in Figure 3.7-b, and the dimensions of the specimen are mentioned in Figure 3.7-c. As the main objective of current study is an analytical investigation of butterfly wings and RCF cracks, the details of the test rig set up are not described here. A detailed description of the test rig can be found in [105]. The test is run on 8620 bearing steel with less than 5% retained austenite content. The maximum Hertzian contact is 2.0 GPa and the contact radii are 130μ and 236μ respectively. The test is interrupted after spalling occurs (after more than 107 cycles), then the sample is cut along the wear track, and etched with 2% Nital etchant. Figure 3.8-a shows butterfly wings formed around an inclusion found at about 200μ below the surface. Figure 3.8-b illustrates a closer view of the same butterfly wings while the equivalent SEM image can be seen in Figure 3.8-c. The microvoids that lead to subsurface cracks are observable mostly on top of the upper wing and bottom of the lower wing. Micro indentation tests were conducted on the upper wing. The indentation marks and their indices are shown in Figure 3.9. The associated hardness values are listed in Table 3.1, 2nd column. The tests show that the hardness increases inside the butterfly wings which is consistent with the observations by other researchers before [41,43]. The reduced modulus of elasticity is calculated using the method suggested by Oliver and Pharr [106]. The ratio of $E_{\text{butterfly}}/E_{\text{Steel}}$ values is listed in the 3rd column of Table 3.12. The average value is calculated to be 0.9041. And the nominal value of 0.9 is selected for the simulations. Therefore, $D_{\text{c-butterfly}}$ is calculated to be 0.1 per Eq. (3.8).

Table 3.1. Hardness and reduced stiffness ratios inside a butterfly wing (Note that test number 0 is conducted on the steel matrix)

Indentation Index	Hardness (HV)	$E_{butterfly}/E_{Steel}$
0	989.1	-
1	1203.2	0.9229
2	1437.8	0.8795
3	1182.8	0.9099

3.4 Butterfly Formation Index

Assuming that butterfly wings are potential crack initiators in bearing steel, it is of great importance to have a good understanding of the regions below the surface which are the most susceptible to butterfly formation. Nelias et al. [90] have presented the number of inclusions at different intervals under the surface of the material using ultrasonic pretest detection and optical inspection after failure. As the half-contact width is mentioned in the same study, it is possible to non-dimensionalize the depth. Figure 3.10 shows the number of butterflies (non-dimensionalized with respect to the maximum value) versus depth (non-dimensionalized with respect to half-contact width) for the optical inspection with square markers. It can be seen that the highest frequency of butterfly formation is at about 0.5b below the surface. This is about the depth of maximum alternating shear stress. Many researchers have suggested that butterfly formation is a stress based phenomenon [76,107,108].

However, it should be noted that a simple linear relationship between stress reversal and butterfly formation will not explain the butterfly formation frequency accurately.

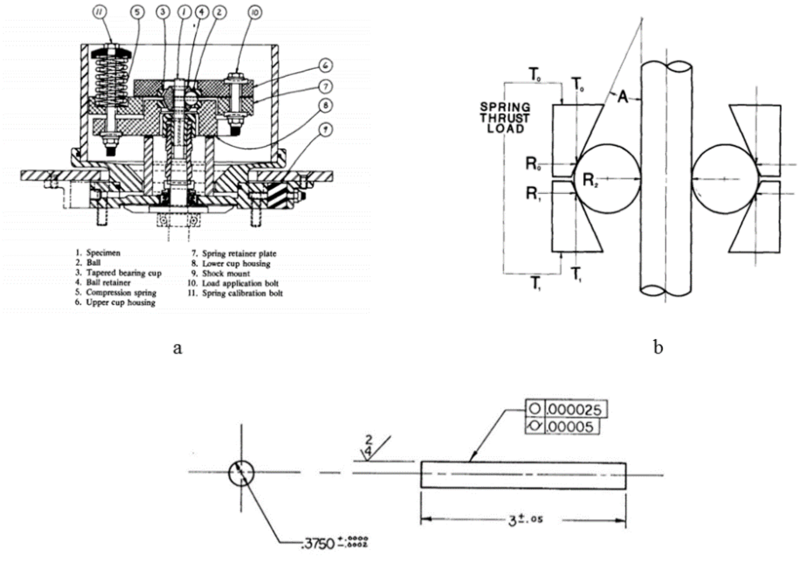

a

b

c

Figure 3.7. Three ball & rod RCF tester. a) Schematic of the components b) geometry of the contact (dimensions are mentioned in [105]) c) specimen geometry. All images are from [105].

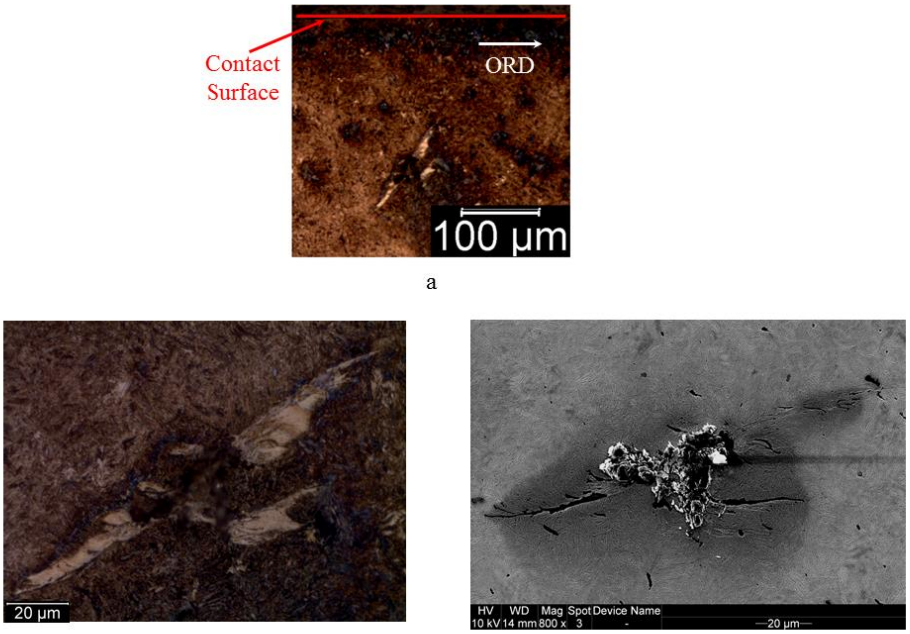

a

b

c

Figure 3.8. Butterfly wing formation in the rolling contact specimens: a) Position of the wings relative to contact surface and over rolling direction. b) Optical image of the same butterfly. c) SEM image (note that images (b) and (c) are slightly rotated due to set up limitations).

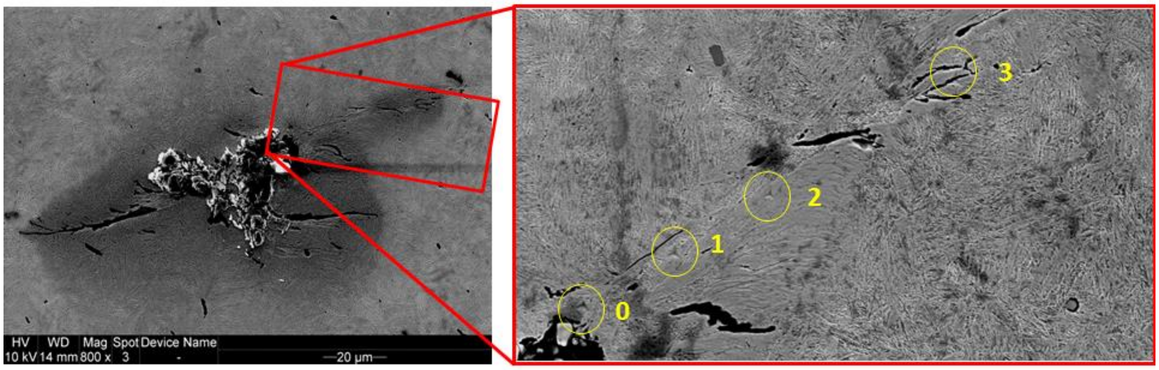

a

b

Figure 3.9. SEM image of the aforementioned pair of wings (a). Indenter marks for the hardness tests are circled along with the indentation test index.

As depicted in Figure 3.10 by circular markers, a simple linear implementation of shear reversal as a reason for butterfly formation can predict the depth for maximum butterfly frequency very closely; however, it fails to explain the drastic drop in the frequency at points farther away from 0.5b.

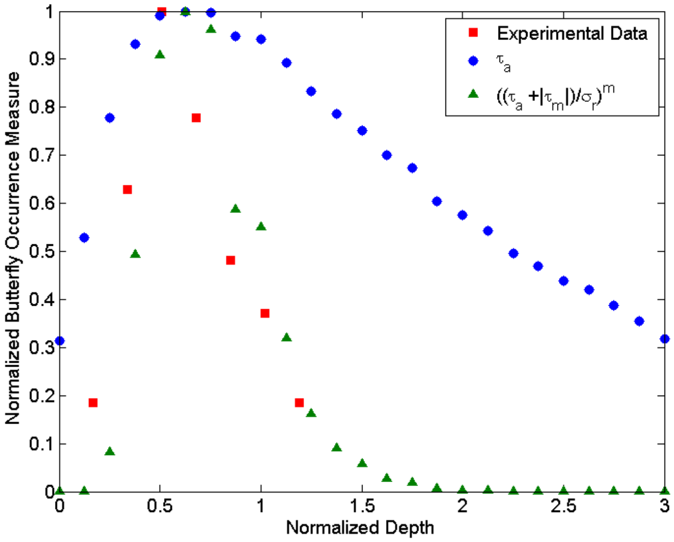

Figure 3.10. Normalized butterfly formation frequency versus depth as observed by [90] and predicted by the current model.

The current study uses continuum damage mechanics to explain butterfly formation in bearing steel. For this purpose, the authors introduce the butterfly formation index, BFI, to gauge the potential for butterfly wing formation:

$$BFI= \left(\frac{|\tau_{mean}|+\tau_{alternating}}{\sigma_r}\right)^m \tag{3.9}$$

It should be noted that Eq. (3.9) is almost the same as Eq. (3.4); in fact, Eq. (3.9) conveys the damage evolution rates at the beginning of the simulation when D=0 for all the elements in the material; this approach provides a comparison of damage evolution rate for different elements at different depths. The triangular markers in Figure 3.10 show how the BFI changes with depth. Because of the high value of m in the exponent, at the depths far from 0.5b the value of BFI has a dramatic reduction. As can be seen, the normalized values closely follow the experimental observations by Nelias et al. [90].

3.5 Effect of Different Inclusion Parameters on RCF Life

This section describes the results of RCF life and spall formation using the developed model. To calculate the RCF life, Eq. (3.4) is rearranged and integrated from zero to $D_{c\text{-}Butterfly}$ and $D_{c\text{-}Crack}$ for butterfly formation and crack initiation respectively. In each simulation, the number of cycles is added up, and when a crack reaches the surface, the total number of cycles designated the final fatigue life. By changing the inclusion parameters such as size, depth, and stiffness, it will be possible to observe the influence of these factors on severity of inclusions. Butterfly formation life and final fatigue life are recorded in each case to compare inclusion detriment on each phenomenon relatively. As discussed in the model description section, the current model is sensitive to the microstructure. To account for the effect of microstructural randomness, 33 domains were developed for each case study similar to what [109] suggests to account for the effect of microstructural randomness in the domain. Besides, in each case study, it has been tried to change only one variable at the time to narrow down the possible factors which can affect the results. All different tests scenarios are listed in Table 3.2. The matrix and Hertzian pressure profile characteristics for all the cases are the same and are listed in Table 3.3.

Table 3.2. Test scenarios for different case studies

	Parameter	Inc. Size	Inc. Stiffness	Inc. Depth	Lower Bound of Parameter	Upper Bound of Parameter
Case Study 0	No Inclusion	-	-	-	-	-
Case Study 1	Size	-	300 GPa	0.5b	8 µ	16 µ
Case Study 2	Stiffness	16 µ	-	0.5b	300 GPa	400 GPa
Case Study 3	Depth	16 µ	300 GPa	-	0.8b	0.5b

Table 3.3. Model parameters for domains without inclusions

b	P_{max}	Friction Coeff.	Grain Size	Matrix Stiffness	Domain Length	Domain Depth
100 µ	2 GPa	0.05	10 µ	200 GPa	1000 µ	700 µ

3.5.4 Effect of Inclusion Size

In this section, two scenarios are compared: 16μ inclusion versus 8μ inclusion. In both cases the inclusions have a stiffness value of 300 GPa and are located at 0.5b. Figure 3.11 compares the alternating shear stress at the centerline of a domain for inclusions varying in diameter from 8μ to 16μ. As can be seen, the peak stress in the raised stress regions is almost the same for all the cases, however, larger inclusions subject larger volumes of the material to stress concentration.

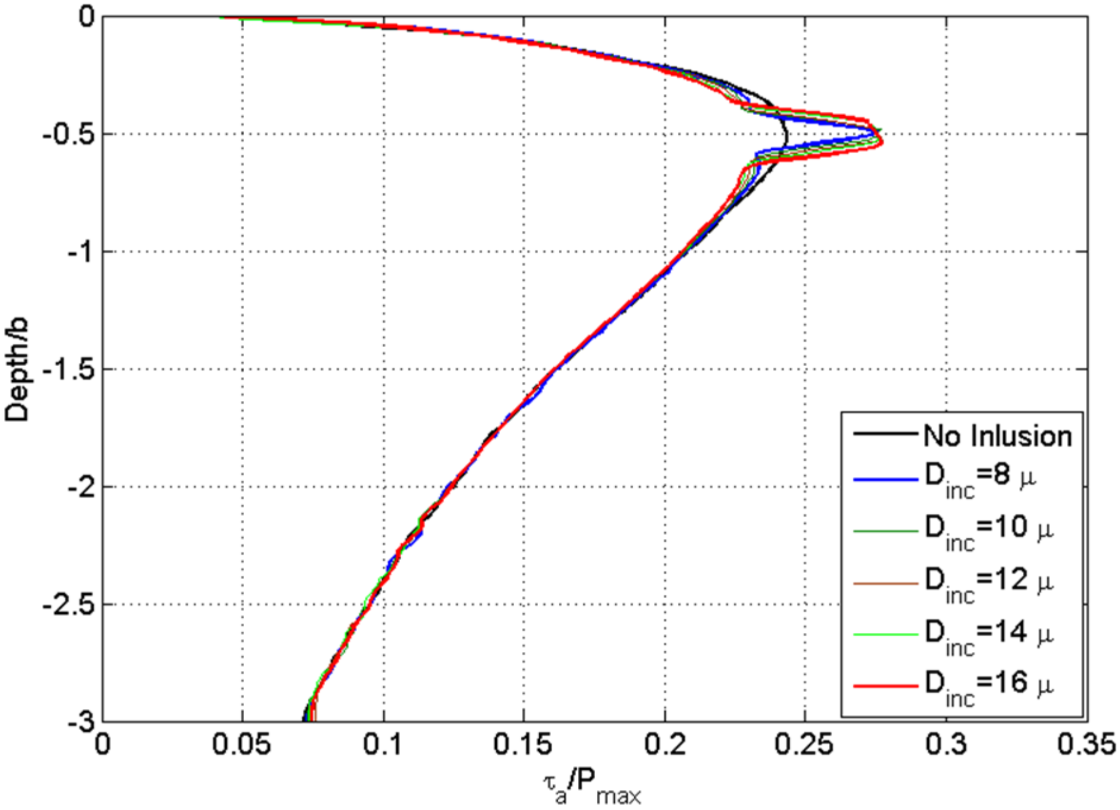

Figure 3.11. Effect of inclusion size on alternating shear stress at the centerline of domain.

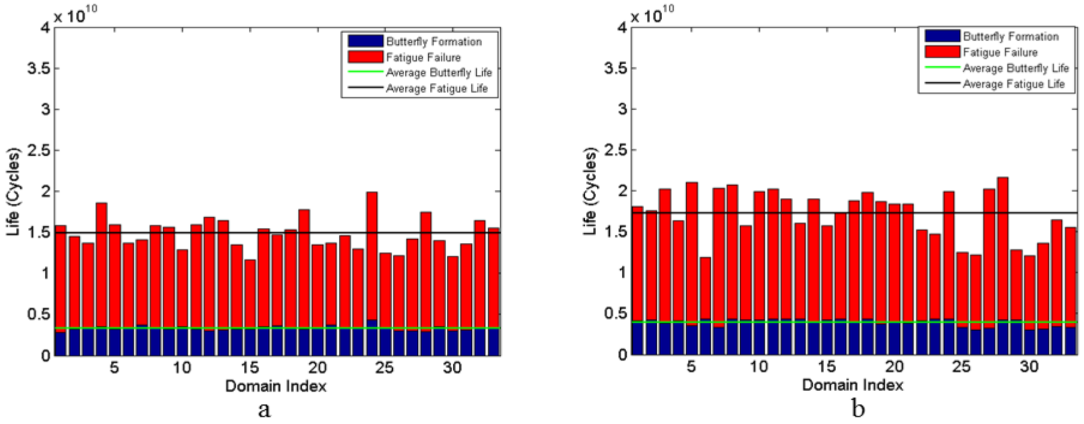

Figure 3.12. Effect of inclusion size on fatigue life: a) 16μ inclusion b) 8μ inclusion.

Figure 3.12 depicts the butterfly initiation and final fatigue lives for all the domains. As can be seen, although the average final life for larger inclusions is shorter than smaller inclusions, this difference is not significant. At first glance, these results are in contrast with experimental results where most authors have found larger inclusions to be more detrimental to fatigue life. To validate these results it is important to take a close look at the stress solutions around the inclusions. Figure 3.13 shows the stress component which is assumed to be responsible for butterfly formation around an 8μ inclusion, and a 16μ inclusion, during a load cycle; the stresses are plotted as a function of the rotational position around the inclusion. As can be seen, the FEM solution does not show much difference in the stress concentrations around the inclusions.

A stereological study is conducted parallel to the FEM to find a possible explanation for the aforementioned observation. Figure 3.14-a depicts an RVE extended along the rolling direction. The yellow plane is a plane located at 0.5b, where the maximum reversal of shear stress happens as the roller moves along the bearing race. A large number of inclusions (10,000) are located in the domain randomly. The RVE is regenerated with 66

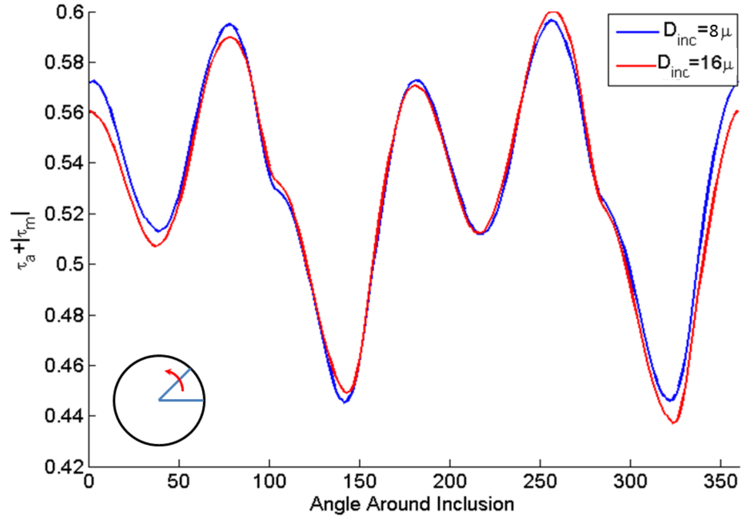

Figure 3.13. Stress variation around an inclusion located at 0.5b versus the rotational position for two inclusion sizes. Rolling direction is from right to left.

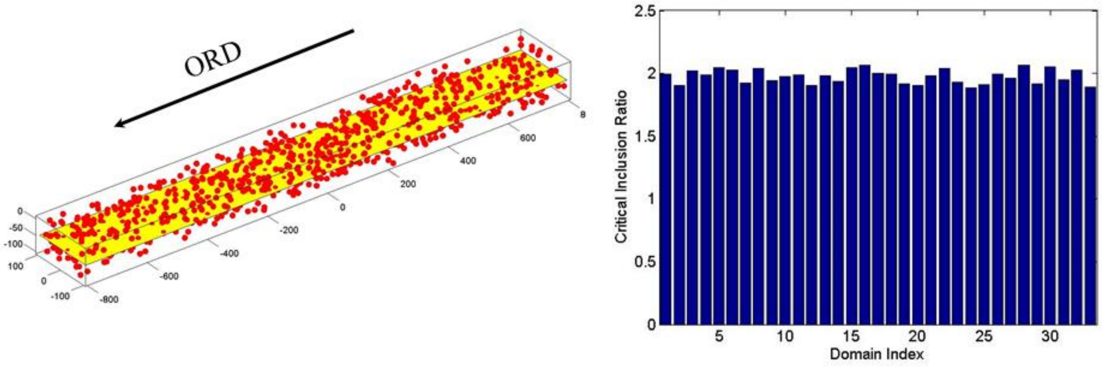

a

b

Figure 3.14. Schematic of the model to calculate number of randomly located inclusions at the critical depth (a), and the ratio of the number of critically located 16μ inclusion to 8 μ inclusions.

random arrangements, 33 domains with 16μ inclusions and 33 domains with 8μ inclusions. The number of intersections between the plane and inclusions is counted in each case and their ratio is plotted in Figure 3.14-b for each pair of random distributions. As can be seen, the ratio is nearly two for all the domains. This corresponds well with the analytical stereological value for this problem which is exactly 2.0.

The results of these studies can be interpreted together as follows: in a matrix with randomly located inclusions around the raceway, though the stress concentration for the round inclusions is not affected by inclusion diameter, larger inclusions have a higher chance of being located at the critical depth. This can be one of the reasons for more detrimental effects due to larger inclusions in bearings. Besides, in this study, all the other factors except for the inclusion diameter are kept the same to purely study the effect of inclusion size. However, it should be noted that in reality, there might be other factors that differ between large and small inclusions such as inclusion/matrix bonding condition, inclusion cracking, etc. For instance, partially debonded areas can serve as premier locations for crack propagation as the crack is already formed there.

3.5.5 Effect of Inclusion Stiffness

Another important factor to consider when studying the inclusion behavior in the matrix is the inclusion modulus of elasticity. It is well known that inclusions have different moduli of elasticity due to distinct chemical compositions. Current study focuses on the behavior of inclusions stiffer than steel which are known to be more harmful to bearing performance. Figure 3.15 shows the alternating shear at the centerline of the RVE for different domains with a 16μ inclusion located at 0.5b. The moduli of elasticity of the inclusions changes from 250 to 400 GPa. As can be seen, the stress

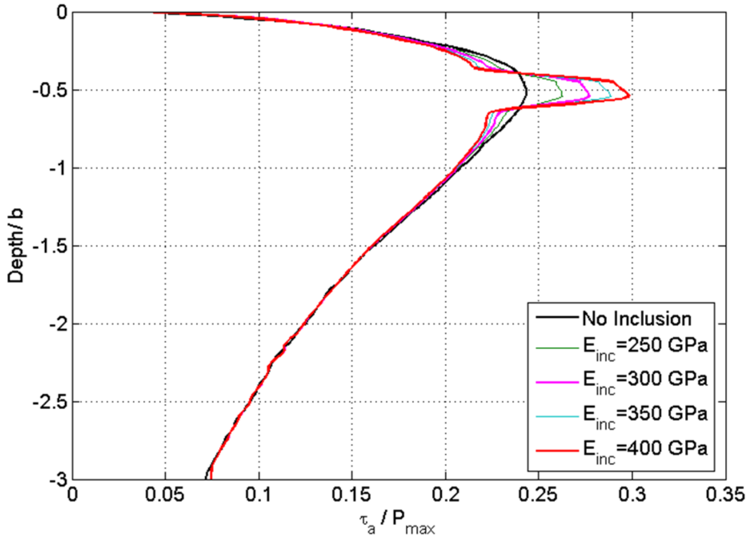

Figure 3.15. Effect of inclusion stiffness on alternating shear stress at the centerline of domain.

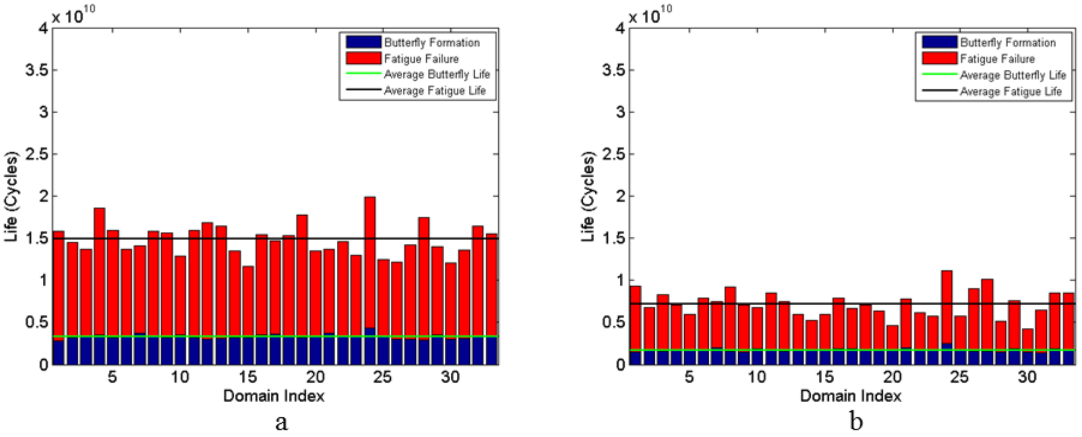

a

b

Figure 3.16. Effect of inclusion stiffness on fatigue life: a) 300 GPa inclusion b) 400 GPa inclusion.

concentration due to an inclusion increases for stiffer inclusions. Among all these inclusions, the ones with moduli of elasticity 300 GPa and 400 GPa are of special interest because of these properties correspond to MgO and Al2O3; which are among the most common non-metallic inclusions in bearing steel.

The fatigue lives are shown for all the domains in Figure 3.16. As mentioned in Figure 3.15, higher stress concentrations around stiffer inclusions reduces the average life by more than half, both for butterfly initiation and final fatigue lives.

3.5.6 Effect of Inclusion Depth

In reality inclusions are found randomly at different depths in the bearing steel. Consequently it is of great importance to determine how inclusion depth affects RCF failure. Figure 3.17 shows the shear stress variation along the centerline of the RVE for domains embedding a 16μ inclusion with a modulus of elasticity of 300 GPa. The inclusions are located from 0.2b to 1.5b in depth. It can be observed that inclusion presence raises the stress reversal due to stress concentration while keeping its shape and slope almost identical. It can be seen for inclusions deeper than 1.1b the stress concentration due to inclusion is less than shear reversal at 0.5b in a pristine domain. This brings up the idea that for inclusion deeper than 0.5b, the inclusion severity decreases as the depth increases. However, although the drop in the alternating shear is even more drastic for points shallower than 0.5b, the detrimental effects of the inclusions in this region does not decrease significantly [110]. One of the possible reasons can be due to interaction of mechanisms causing subsurface spalling and surface pitting for shallow inclusions. To compare RCF lives, 33 domains with a 16μ, 300 GPa inclusion at 0.8b were simulated and the results are compared with a similar inclusion at 0.5b. As the surface pitting mechanisms are out of the scope of this model, no case study for shallow inclusions was conducted. In

Figure 3.18, it can be seen that deeper inclusions have a higher RCF life both for butterfly initiation and final lives. Another look at Figure 3.17 suggests that for inclusions deep enough the value of stress concentration due to inclusion will drop so much that RCF might happen due to shear reversal at 0.5b. In this case the RCF life of domains with very deep inclusion is expected to converge to that of pristine domains without inclusions.

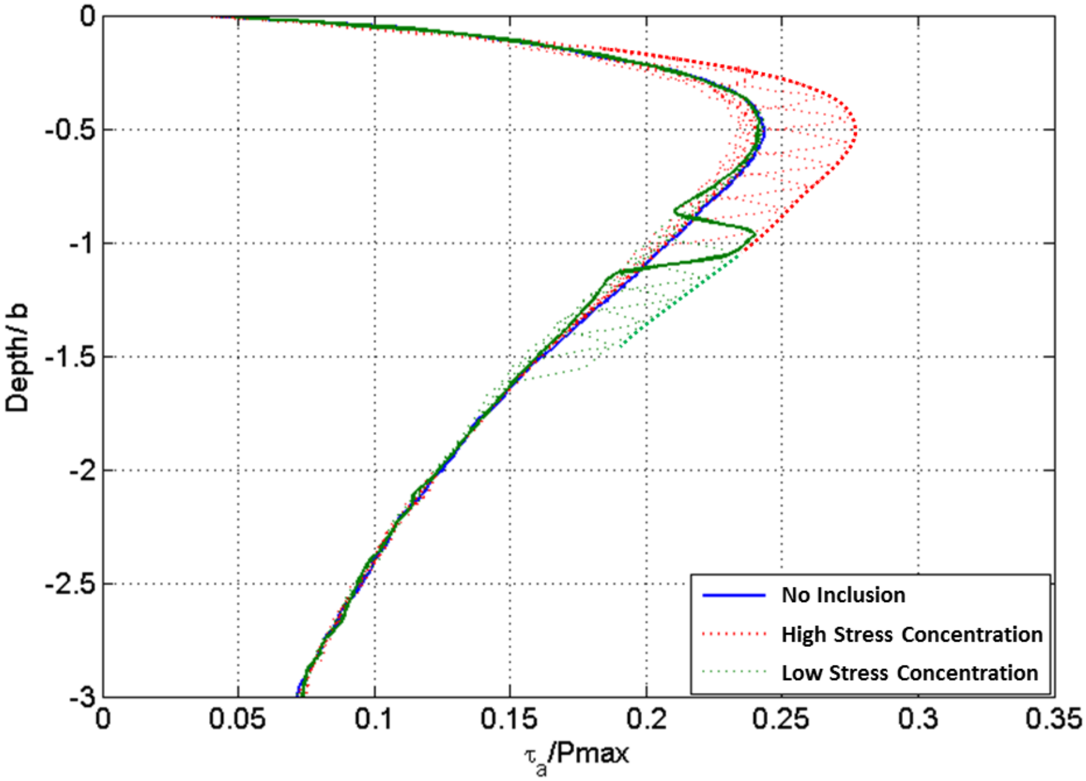

Figure 3.17. Effect of inclusion depth on alternating shear stress at the centerline of domain.

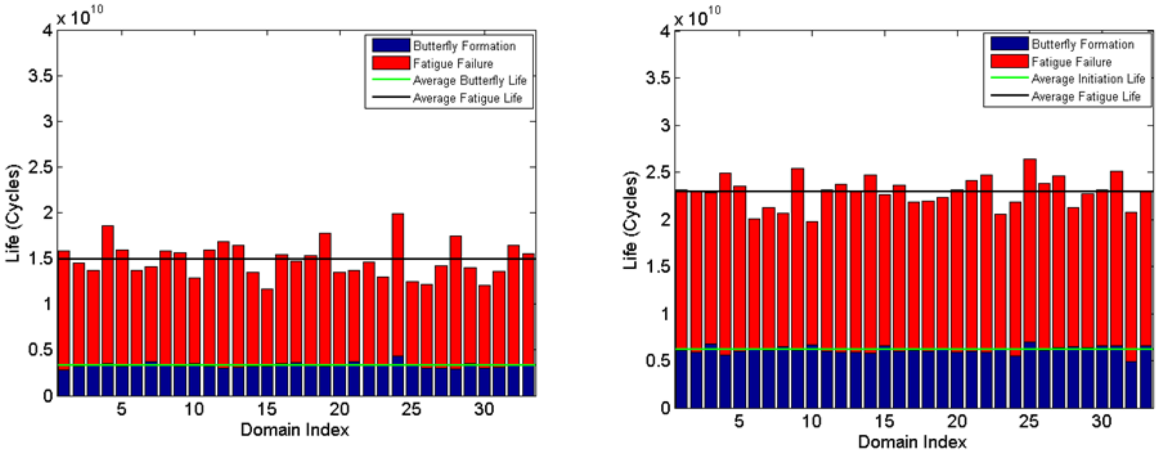

a

b

Figure 3.18. Effect of inclusion depth on fatigue life: a) inclusion at 0.5b b) inclusion at 0.8b.

3.6 Comparison of Weibull Plots

Figure 3.19 compares the Weibull probability plots for the butterfly formation and final lives of different case studies. As can be seen, in almost all the cases, final lives show more scatter compared to initiation lives. This is because in each scenario, butterflies initiate due to a certain type of inclusion located at a certain location and their appearance is almost independent of microstructure. Consequently, the initiation lives are almost identical; however, crack propagation is a function of material microstructure and is affected by its randomness which culminates in more scatter in final lives. The dashed orange line highlights 10% failure probability. In other words, intersection of Weibull plots with this line indicates the L_{10} life for each case study. It should be noted that each of the plots in Figure 3.19 shows the RCF failure due to a certain type of inclusion. However, in bearing operation, failure happens due different types of inclusions and also factors other than inclusions. Different failure roots can culminate in more scatter in the fatigue results.

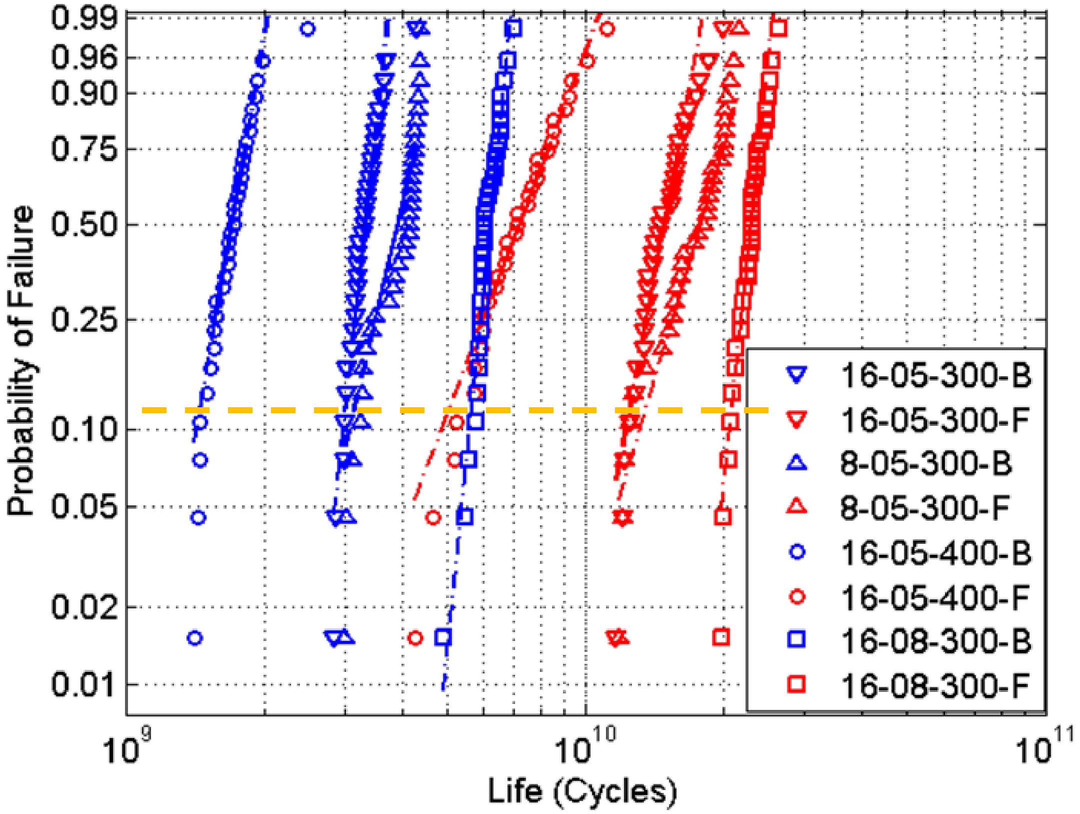

Key to read the graph labels: X-YZ-W-U
X: Inclusion diameter (μ)
YZ: Inclusion is centered at Y.Z (b) under the surface
W: Inclusion stiffness (GPa)
U: "B" stands for Butterfly Formation & "F" stands for Fatigue Failure

Figure 3.19. Comparison of Weibull plots for different case studies.

To account for this difference, all the results from different case studies are combined to form a larger statistical population and the results are plotted in Figure 3.20 both for butterfly formation and for final fatigue lives. As can be seen, the combined results for all case studies show a much higher scatter with a Weibull slope value of 2.5 and 2.9 for butterfly and final failure respectively. These

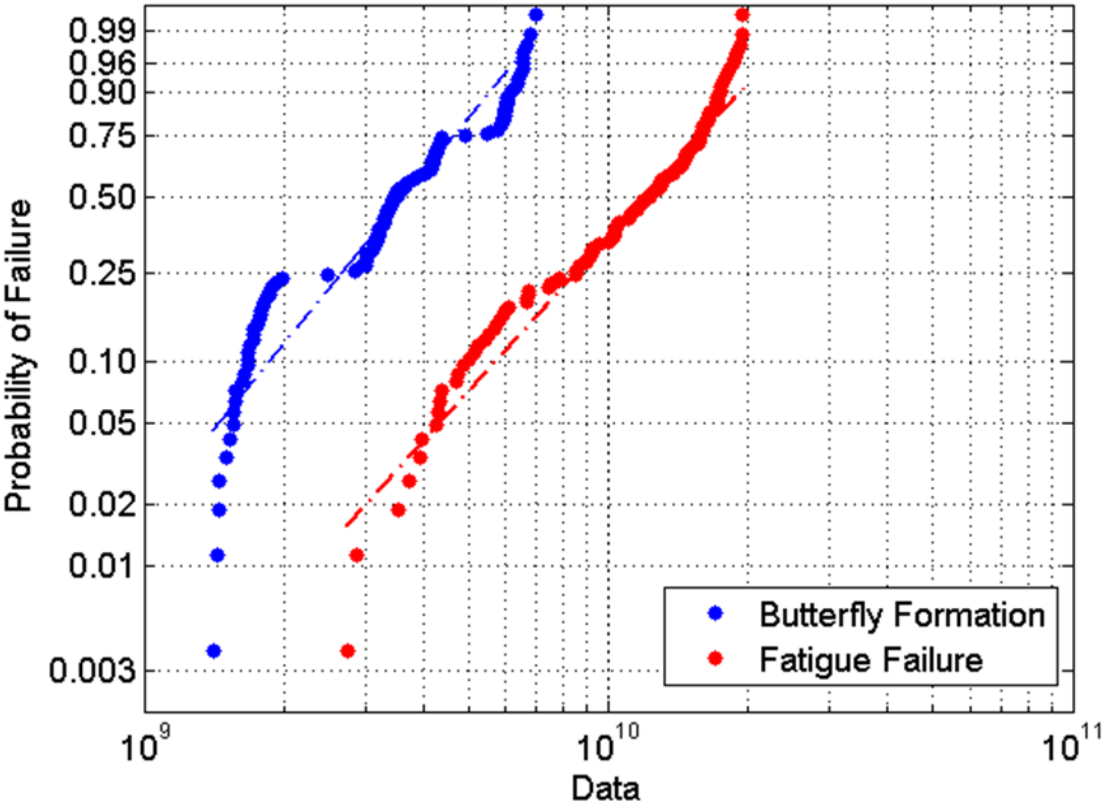

Figure 3.20. Weibull plots for initiation and final lives of all case studies combined.

values fall between the Weibull slope range for ball and roller bearings which is known to be from 0.51 to 5.7 for 52100 bearing steel [53]. It should be noted that this value accounts only for failure due to inclusions. Factors such as surface pitting, improper lubrication, white etching cracks, etc. will add to scatter and lower the Weibull slope even more compared to the results illustrated in Figure 3.20.

3.7 Effect of Butterfly Wings on Crack Maps

In most of the well-shaped, symmetric butterfly wings, it has been observed that cracks are mostly observed on top of the upper wing and bottom of the lower wing [41,46]. Evans et al. [44] suggest that these cracks form as a result of microvoid coalescence in the butterfly/matrix interface. Such cracks can be observed in similar positions in the SEM image of the same pair of butterfly wings which was used for hardness measurement earlier in this study. As can be seen in Figure 3.21, the butterfly wing boundaries are marked with yellow, and cracks with red to compare the relative location of cracks around the wings.

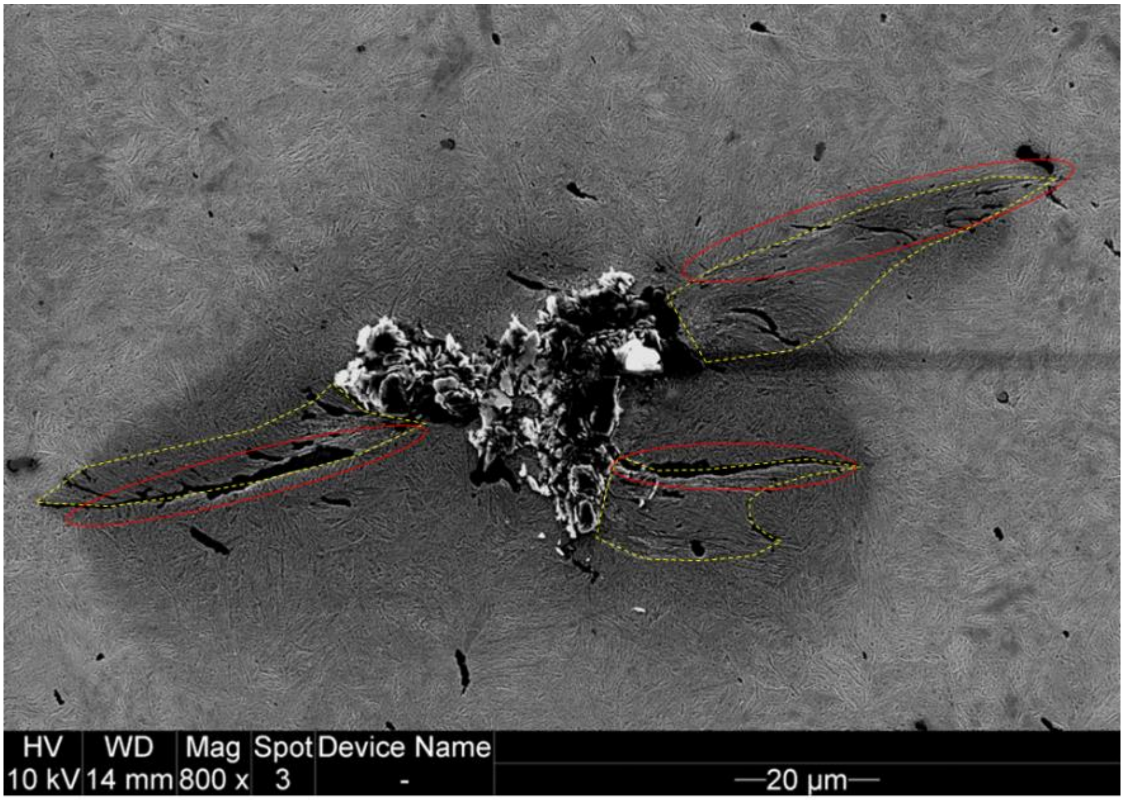

Figure 3.21. Crack initiation at butterfly wings due to microvoid coalescence at butterfly/ matrix interface. For the purpose of clarity, the wing boundaries are indicated in yellow and the microvoids are marked in red.

A study was conducted on the spall geometries in different domains to compare the crack maps with experimental observations. As shown in a previous study, butterfly wings can vary in shape and size based on inclusion depth and size and the most well shaped and symmetric wings appear around 0.5b. For this purpose, the crack geometries of all 33 domains were studied. In 26 out of 33 domains, there is higher concentration of microcracks either on top of the upper wing and/or bottom of the lower wing. Figure 3.22 shows three domains with such crack maps. In most of the cases, as soon as one of the branches of the crack extends beyond the region affected by the inclusion, that particular branch becomes dominant and extends to the surface and forms the final spall.

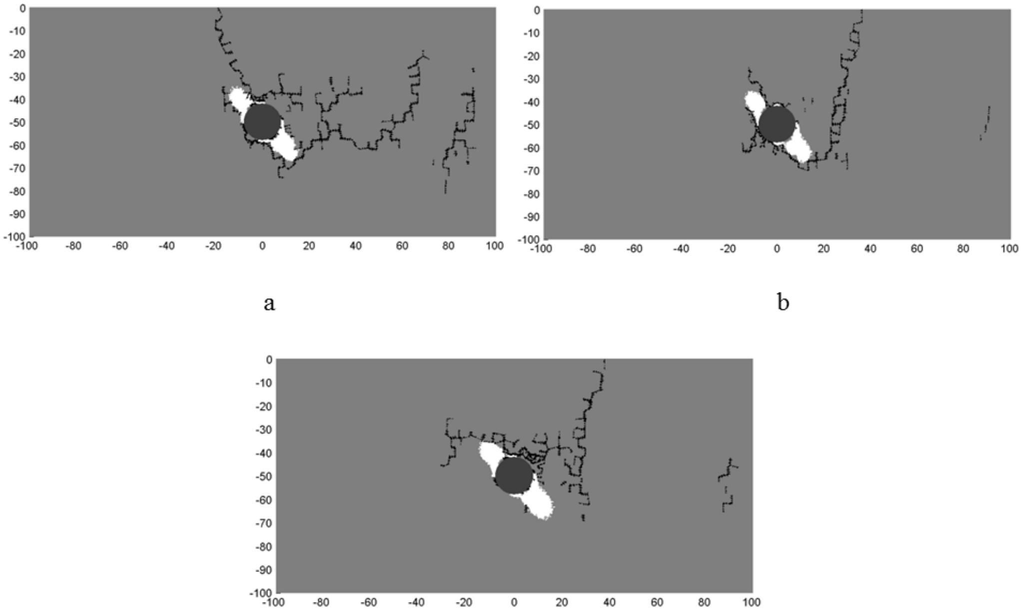

a

b

c

Figure 3.22. Sample crack maps from simulations with 16 μ at 0.5 b. The domain indices are 08 (a), 13 (b), and 22 (c).

3.8 Summary and Conclusions

This paper presents a model to study butterfly wings formation around non-metallic inclusions and investigates the effect of these microstructural changes on crack formation in bearing steel. A new metric called Butterfly Formation Index (BFI), which considers the material's resistance to fatigue damage and the subsurface stress loading, is implemented to predict the propensity of butterfly wing formation at different depths. A confluent experimental study was conducted to obtain the critical damage value inside the butterfly wings. This value is implemented to develop a damage evolution equation which works with a 2D FEM model to simulate butterfly wing formation, crack initiation, and propagation throughout the cycles. To capture the effects of microstructural randomness of the matrix, the material grains are modeled with Voronoi tessellations. The effect of different inclusion parameters such as size, stiffness, and depth on crack formation in bearings is investigated; butterfly formation and fatigue lives are calculated and compared to determine the most detrimental scenarios. It has been found that stiffer inclusions and inclusions closer to the maximum shear reversal depth are more detrimental, while the larger inclusions have a higher chance to fall in the critical region. Finally, the spall geometries are observed. Comparison showed the final crack maps correlate closely with experimentally observed cracks.

CHAPTER 4. 3D NUMERICAL AND EXPERIMENTAL INVESTIGATION OF MICROSTRUCTURAL ALTERATIONS AROUND NON-METALLIC INCLUSIONS IN BEARING STEEL

4.1 Introduction

Ball and roller bearings are among the most important components in all the machinery that have rotary motion. Bearings carry the load through Hertzian contacts between the rollers and the races. Due to geometric restrictions, non-conformal contacts are commonly associated with very large values of stresses. Factors such as improper design and lubrication, environmental debris, unexpected large loads, or bad installation can cause bearing failure. However, if a bearing is well lubricated and operates under the designated loads, the main mode of failure would be due to fatigue. Failure because of this phenomenon is referred to as rolling contact fatigue (RCF).

RCF failure can be divided into two main categories: i) surface pitting and ii) subsurface spalling. While surface pitting can be inhibited significantly by proper lubrication and adequate surface preparation, there are not actually many ways to stop subsurface initiated fatigue *after* the bearing is manufactured and installed. So, it is of great importance to better understand the mechanisms leading to this type of failure in order to improve the bearing design and manufacturing process.

There are a number of differences between RCF and other types of classical fatigue. As opposed to other types of fatigue such as bending or uniaxial fatigue, RCF occurs due to a very complex state of stress in which there is no significant tensile component. Figure 4.1 plots different stress components experienced by a point located at the subsurface of the material. As can be seen, shear stress is the only stress component which alternates between positive and negative values. That is why RCF is generally known as a shear driven phenomenon. It should be noted that unlike other types of fatigue, the volume of the material subjected to large stresses is very small, about few hundred microns in depth for most cases. Consequently, fatigue phenomena occur in a scale comparable to grain size of the material. This makes the fatigue behavior of the material strongly microstructural sensitive.

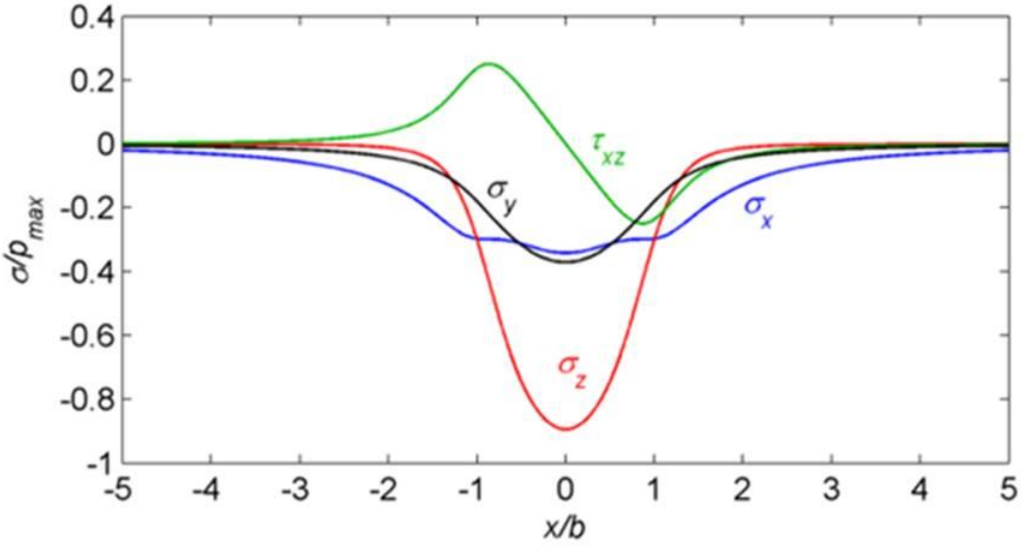

Figure 4.1. Stress History of a point located at the subsurface of the material as the Hertzian load passes over.

It has been observed that when bearing steel is subjected to rolling contact loading certain microstructural alterations can occur in the matrix [111]. Such changes are commonly categorized as butterfly wings, white etching cracks (WECs), dark etching region (DER), and white etching bands (WEBs). Figure 4.2 shows examples of each microstructural alteration type. Among these features, butterfly wings and WECs are more concerning since they appear before L_{10} life of bearing and can result in premature failure of the bearing. The current work investigates butterfly formation experimentally and numerically.

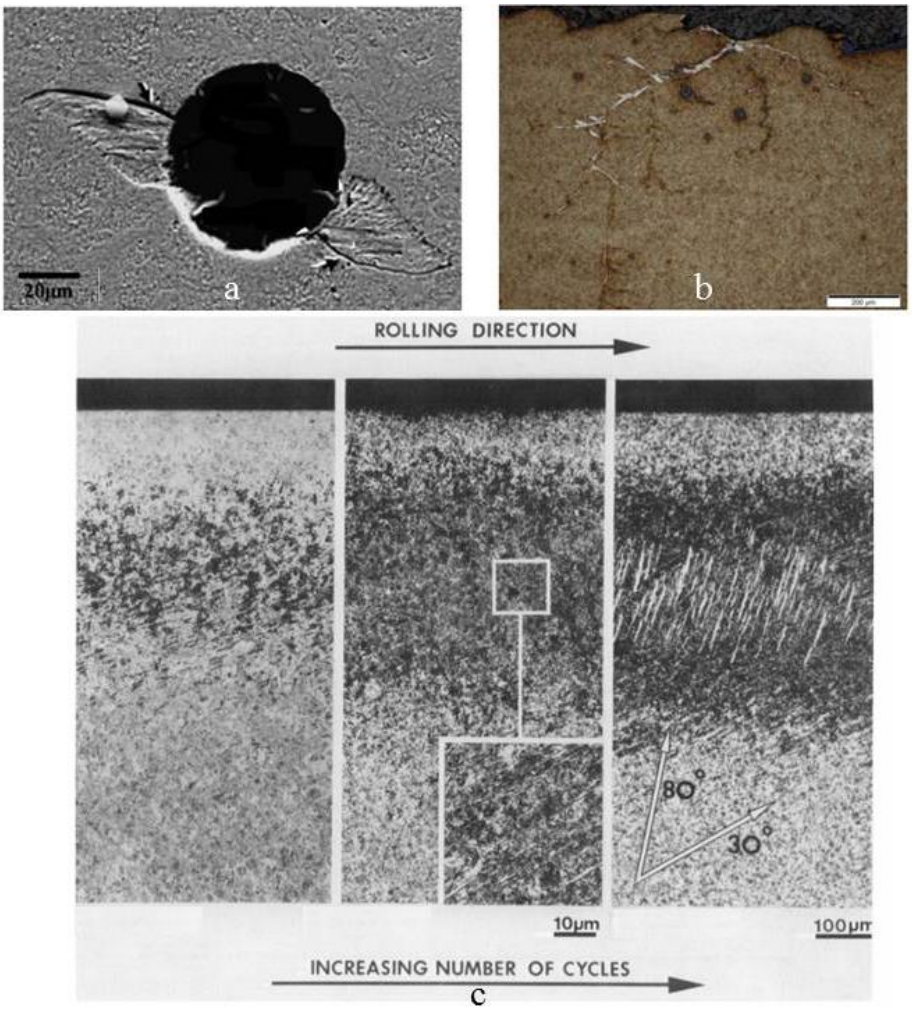

Figure 4.2. Different types of microstructural alterations . a) Butterfly formation [46], b) WEC [47], c) DER (left), DEC+flat bands (center), and DER+ flat bands+ steep bands (right) [6].

First observed in 1951 [112], butterfly wings have been known for more than sixty years. Butterflies are commonly addressed as regions of microstructurally altered material in the vicinity of the nonmetallic inclusions. Most of the butterflies are comprised of two wings that emanate from the inclusion at a 45 degree angle relative to over rolling direction (ORD). The grain size within the wings can be small as 5 nanometers. The regions are most probably made of ultrafine ferrite grains. Butterflies can lead to failure since they are accompanied with many micro-cracks. Two major cracks are commonly observed on top of the upper wing and bottom of the lower wing which can propagate beyond the wings and cause the RCF failure [93].

Since the first observation of butterflies, many experimental attempts have been conducted to investigate their root cause analysis, morphology, and detrimental effects. Early attempts included optical microscopy of the butterflies to study their geometry, size, and location relative to ORD. In the recent years, newer techniques such as SEM, TEM, FIB, and EBSD [5,44–46] have been implemented to obtain a more in depth knowledge of butterflies. Thanks to these new tools more information regarding the grain size, crystal orientation, etc. of butterflies is obtained. However, all these methods are destructive. This makes it difficult to accurately relate the butterfly formation life to crack initiation and propagation stages which lead to final fatigue. It should be noted that butterflies form at the subsurface of the material and only non-destructive techniques (NDT) would be able to track their initiation and propagation before the failure. Consequently, NDT methods have recently been used to study butterfly formation in bearing steels. Among different techniques ultrasonic inspection, acoustic emission, and X-ray tomography has been the most widely used because of their capability to look inside the matrix [13,57,61,62,113].

Among all these methods ultrasounds have obtained the most popularity due their high accuracy, ease of use, and practicality for in-situ application. Guy et al. [62] used high frequency ultrasounds to spot inclusions and monitor butterfly propgression from them in bearing steel. Their work was continued by Nelias et al. [114] to find butterfly appearance dependence on inclusion depth. Post failure micrography proved the method to be a reliable tool to inspect inclusions as small as 30 microns in diameter. A similar procedure was followed by Umezawa et al. [57]. They investigated the size of the echo image from the inclusion as the number of cycles increased to assess the butterfly and crack progression from the inclusions. Auclair and Daguier [115] found a similar probability of detection of more than 95% for inclusion which are at least 30 micron in diameter. Other researchers have used similar approaches such as Reyleigh waves to detect C-cracks on the surface of the balls [116], fractal dimension analysis to detect WEBs [25], or acoustic emission all around the bearing race to quantify RCF damage [113].

Although butterflies have been known for more than half a century, due to many complications in their root cause analysis, it was only in 1992 when the first attempt was made to suggest a model for their formation. Salehizadeh and Saka [91] proposed residual stress evolution around inclusion as a possible reason for crack formation in butterflies. In 1998, Melander et al. [65–67] analyzed the stress intensity factor variation at the crack tip for cracks that were inserted in an FE model at 45 degrees relative to ORD. Vincent et al. [64] suggested accumulation of dislocations due to stress concentrations can lead to butterfly formation and eventually crack generation, in 1998. Hiraoka et al. [117] looked at the hydrostatic stress distribution around inhomogeneties for both cases with and without cracks in 2005. Later on in 2010, Alley et al. [63] investigated plastic strain accumulation near inclusion during rolling contact loading to simulate the wings. In 2014, Cerullo [118] predicted crack growth by means of irreversible cohesive elements for different crack orientations from inclusion. Also in 2014, the current authors [93] used damage mechanics to predict butterfly wings shape, size, and orientation. Shortly after them, Cerullo and Tvergaard [119] suggested a model to predict wing formation based on Dang Van theorem. Both the current works found the mean shear stress due to surface traction to be important on butterfly wing formation, independently. Mobasher Moghaddam et al. [120] expanded their model to simulate crack propagation from inclusion and final failure. It should be noted that all the previous efforts to model butterfly wing formation has been confined to 2D models and almost all the models have neglected the possible 3D aspects of the problem. (Alley et al. [63] used a 3D FE model; however, they used cylindrical or rectangular inclusions that are extended into the page, which basically reduces the 3D problem into 2D.)

The current work implements and experimental as well as an analytical approach to investigate butterfly wing formation in 3D. A FE model is coupled with a postulated damage law to simulate microstructural alterations around inclusions. Butterfly to inclusion size ratio was observed at different cross section and a closed form solution was suggested for the wing span to inclusion diameter ratio which is compared to experimental data from literature. High frequency ultrasonic inspection of inclusions was conducted to detect inclusions inside the bearing steel. Experimental serial sectioning of one of these inclusions was used as a reference to validate the simulation results. Comparison of the experimental and numerical serial sectioning suggested a lateral expansion of the butterflies in the plane transverse to ORD.

4.2 Modeling Approach

4.2.1 2D vs 3D Models

As discussed in the previous section, almost all the previous efforts to simulate butterfly wing formation have been confined to 2D models. It should be noted that a 2D model assumes plane strain condition. This means that the depth of the features into the page is practically infinite. Following this approach, a circular inclusion is actually equivalent to an infinitely long cylindrical inclusion with its main axis into the page. This is an unrealistic case. In reality, most of the inclusions possess a globular shape.

Butterfly formation is known to be a function of inclusion characteristics. It can be expected that the plane strain assumption of a 2D model is incapable of taking the details of butterfly wing formation in 3D. This idea was promoted after the authors observed white etching regions which were similar to butterfly wings but there was no inclusion visible between the two wings. Figure 4.3 pictures some of these features. As can be seen, the orientation and shape of these inclusion-less butterflies is similar to regular butterflies. Similar features have been observed by Errichello [121], Selecka and Salak [122], and Lund [76]. As can be seen in Figure 4.4, inclusion-less wings may grow and connect to one another as well. Presence of these features suggests that butterflies may propagate out of the plane and transverse to the ORD. A 2D model is incapable of answering this question and it is necessary to investigate the problem in 3D to be able to answer this question.

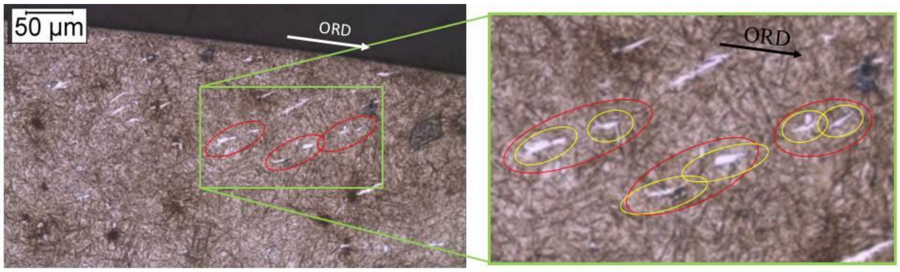

Figure 4.3. White etching features similar to butterflies without inclusions. Note the similarity to butterflies in shape and orientation.

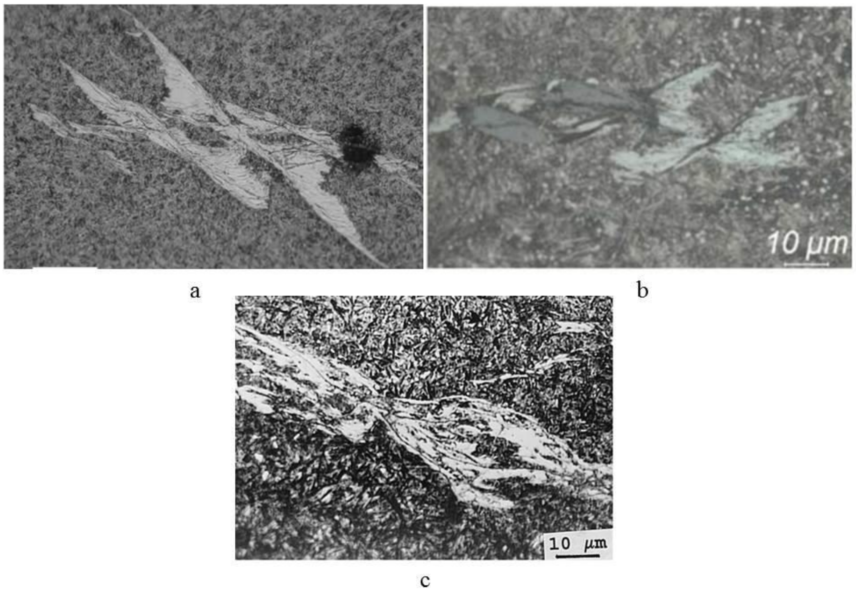

Figure 4.4. Wings without butterflies as observed by Errichello [121] (a), Lund [76] (b), and Selecka and Salak [122] (c).

4.3 Finite Element Model Set Up

A 3D FE model was developed to study butterfly formation in bearing steel. For this purpose, the 3D finite element, granular microstructure model developed by Weinzapfel et al. [98] was modified. The internal topology of the material microstructure is resembled by a series of randomly generated Voronoi tessellations wherein material grains are represented by Voronoi cells.

It should be noted that Weinzapfel et al. [123] used the Voronoi microstructure to account for the microstructural randomness during crack propagation by assuming the grain boundaries as the weak plane. However, the current model does not include crack propagation and the focus is only on the microstructural alteration which is known to be prior to crack initiation stage [124]. The main purpose of using Voronoi microstructure in the current study is to consider the possible effects of grain geometry on microstructural alterations. The FE domain Figure 4.5 shows how a Voronoi cell is comprised of several linear strain tetrahedral elements (LST).

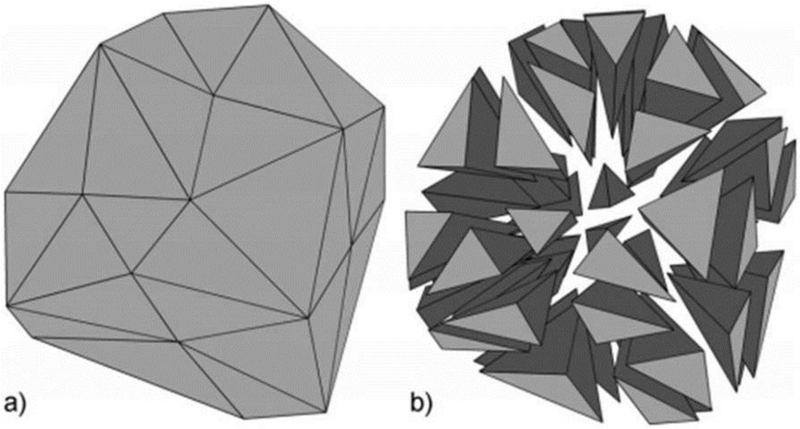

Figure 4.5. a) A material grain modeled by a 3D Voronoi cell, b) elements forming the same Voronoi cell [98].

Since the model assumes a linear elastic behavior for the material, the maximum Hertzian contact is chosen to be 2.0 GPa to avoid possible plastic deformations that may occur when excessive loads are applied. The action of a passing Hertzian load due to over rolling on the model is simulated by applying a sequence of Hertzian (parabolic) contact pressure distributions. The half contact with of this pressure profile is 50 micron and it moves from

-2b to +2b over the center of the representative volume element (RVE). Each loading cycle is modeled by combination of 21 discrete loading steps that move over the RVE. A tangential surface traction value of 0.05 opposite to over rolling direction is applied to resemble the surface friction of the driven roller similar to [20]. The model uses the commercially available FE software ABAQUS as the stress solver. A user defined subroutine UTRACLOAD was developed to apply the surface friction. More details about the FE model set up and element types are presented by Weinzapfel et al. [98] and are not mentioned here for sake of brevity.

As a modification to the existing model, a 16 microns inclusion is embedded inside the domain and at the centerline of the RVE at 0.5b below the surface. The inclusion is assumed to be perfectly bonded with the matrix. The reason for this depth selection is because 0.5b is the depth where the alternating in-plane shear stress has its maximum value. The modulus of elasticity of the inclusion is set to 300 GPa as opposed to a modulus of 200 GPa for the steel matrix. To reduce the number of factors that may affect the butterfly wing formation and shape, a simple sphere was selected as the default shape of the inclusion. To model this globular inclusion, the Voronoi seed points in the inclusion region were laid out in two concentric spheres that are evenly spaced from the boundaries of the desired inclusion, as pictured in Figure 4.6-a. This method, known as mirroring, a smooth spherical surface made of uniformly spaced Voronoi cells to build up the inclusion. The inclusion itself is illustrated in Figure 4.6-b. The FE model set up, boundary condition, and element type selection is in accordance to what Weinzapfel et al. [98] simulated and the details are not repeated here.

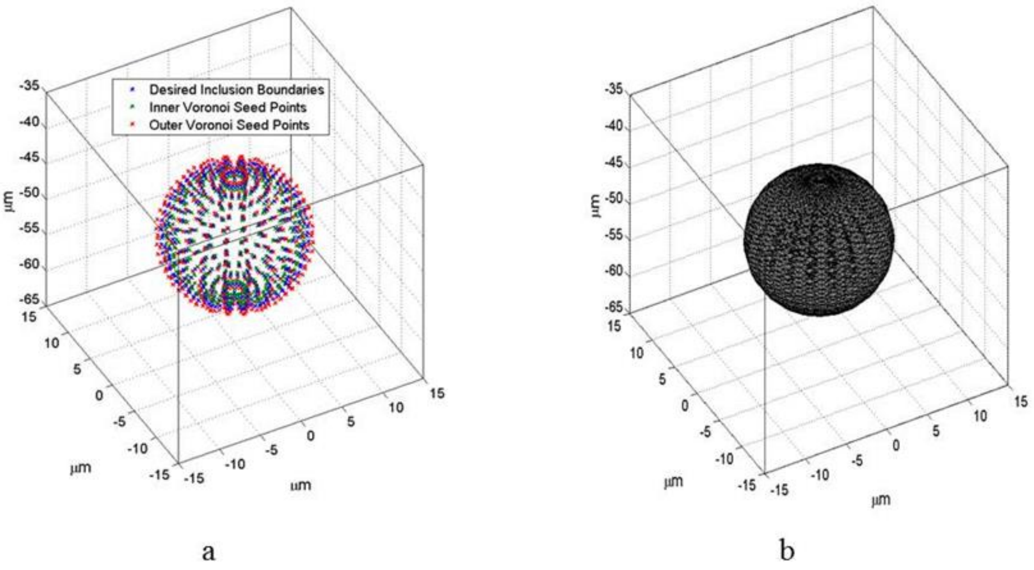

Figure 4.6. a) Mirroring procedure to lay Voronoi seed points that comprise a smooth spherical inclusion, b) the corresponding inclusion.

4.4 Theory

As discussed in the introduction, different researchers have attributed butterfly formation to a number of distinct factor. Since butterfly formation is related to RCF, and RCF is believed to be a shear driven phenomenon, the current work implements a stress based approach with a focus on shear stress to model butterfly formation. Continuum damage mechanics has widely been used to model fatigue problems in general [70–72] and RCF in particular [78,93,123,125]. The authors in previous works have implemented damage mechanics to model butterfly wing formation in 2D. An in depth review of the fundamentals of the model is presented by Xiao et al. [70] and the extension of the damage law to model butterfly formation is discussed in [93] in detail. Here, a short review of the theory is presented.

In CDM method, material degradation due to cyclic fatigue loading is simulated by updating the constitutive relationship. For this purpose, a thermodynamic state variable referred to as damage, D, is introduced in the domain such that each element of the material has a certain and constant damage value during each loading cycle. Fatigue damage due to cyclic stresses manifests itself as a gradual evolution of this parameter.

The updated constitutive relationship due to damage has the following general form:

$$\sigma_{ij} = C_{ijkl}(I_{klmn} - D_{klmn})\varepsilon_{mn} \tag{4.1}$$

Where σ_{ij}, C_{ijkl}, I_{klmn}, D_{klmn}, ε_{mn} are the stress, stiffness, identity, damage, and strain tensors respectively. For the case of isotropic material which is the assumption in this study, Eq. (4.1) can be simplified to

$$\sigma_{ij} = C_{ijkl}(1 - D)\varepsilon_{kl} \tag{4.2}$$

The damage progression law used in this model is based upon the equation suggested by Xiao [70]. According to Xiao, damage in the material evolves due to cyclic loading by:

$$\frac{dD}{dN} = \left(\frac{\sigma}{\sigma_r(1 - D)}\right)^m \tag{4.3}$$

In the equation above, N indicates the number of loading cycles and σ is the stress component that mainly causes the fatigue damage. σ_r and m are material depended constants. σ_r is commonly known as resistance stress since it represents the material's ability to resist fatigue damage accumulation. The stress component responsible for fatigue damage depends on the loading condition and can vary from case to case. The damage evolution law for this study is the same as what has been used in an earlier study [93] which focuses on the effect of alternating and mean value of shear stress during each load cycle. The damage equation used in this investigation has the following form:

$$\frac{dD}{dN} = \left(\frac{\tau_{alternating} + |\tau_{mean}|}{\tau_r(1 - D)}\right)^m \tag{4.4}$$

Parameters τ_r, m, and b are material properties that are determined by curve fitting S-N data obtained from torsion fatigue experiments. Detailed information regarding how the damage evolution equation is derived and how it is calibrated is presented in reference [93] and is not repeated here. It should be noted that the D value for the pristine material is set to zero. Damage quantity for each element is increased by applying Eq. (4.4) and using a jump-in-cycle algorithm [69]. The critical damage value for the martensite to ferrite transformation was measured by authors in an earlier work and is set to 0.1 [120]. When the damage in an element reaches the critical value, that particular element is assumed to be microstructurally altered and no further damage is evolved in that element. This means that the modulus of elasticity of the altered material would be 0.9 times the modulus of elasticity of the pristine matrix. Also, since the damage properties for the inclusion material are not available, as a simplification to the model, no damage is applied to the elements of the inclusion.

In an ideal case, the value of shear stress should be calculated at planes with all the different possible orientations. However, this would be very time inefficient. For example, considering a 1 degree step for plane rotation, there will be 180 different possible orientations for a 2D case. In a 3D simulation, this number increases to 180^3 which is equal to 5832000 possible orientations only for one element. To save the computational effort, shear stress at planes in which it has the maximum alternating value is used for the damage calculation. Weinzapfel et al. [99] have already found these planes. As can be seen in Figure 4.7, assuming the X-axis to increase along the ORD, and the Z-axis, being perpendicular to the top surface of the domain, the XZ-plane is found to have the maximum alternating shear stress value.

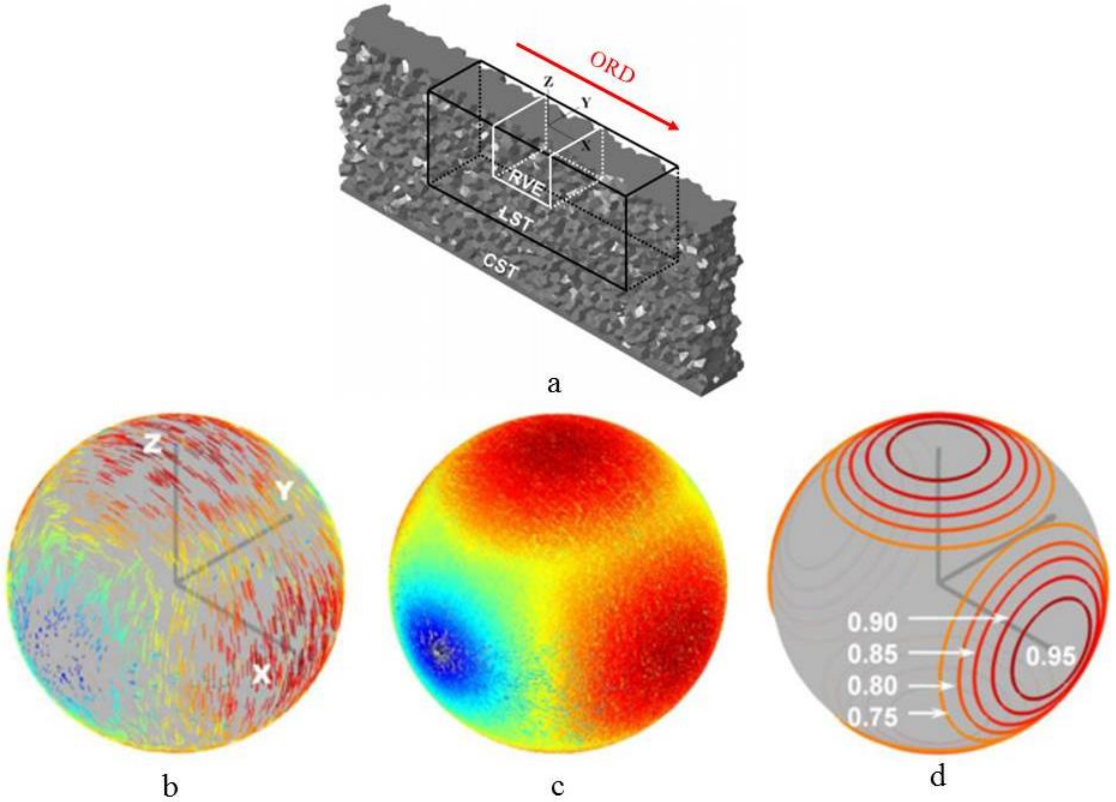

Figure 4.7. a) schematic of the FEM domain and ORD relative to the domain. Critical shear stress reversals experienced by elements is calculated on the planes normal to all possible directions in the 3D space. b) results for the elements of one randomly generated FE domain, c) composite results of several domains, d) bounding contours by percentage of the largest critical shear stress reversal [99].

4.5 Experimental Procedure

4.5.2 Test Rig Description

RCF tests have been conducted on samples made of bearing steel to investigate butterfly wing formation experimentally. A 3ball & rod RCF tester made by Federal- Mogul was used for this purpose. The test rig is shown in Figure 4.8-a. The schematic of the contact between the balls and the rod-shaped specimen is illustrated in Figure 4.8-b, and the dimensions of the specimen are mentioned in Figure 4.8-c. Three 12.7 mm in diameter balls, made of M50 steel, are separated by a retainer and are radially loaded against the test specimen between two tapered cups which are thrust- loaded by three compression springs. The tests are run samples of case carburized AISI 8620 bearing steel with more than 30% retained austenite content. The maximum Hertzian contact is 2.0 GPa and the minor and major radii of the elliptical contact are calculated to be 130 microns and 236 microns respectively. The test is conducted at a constant rotational speed of 3600 rpm. Turbine oil (MIL-PRF-23699-STD) is used at room temperature (25C) to lubricate the contact. The test is interrupted after the failure happens due to spalling on the specimen. For this purpose, an accelerometer is installed on the tester head to track the vibration. The failure criterion is set so that when the vibration level increases to 0.5 RMS above the initial value the test will stop automatically. More information about this test rig can be found in [126]. In the experimental front of current work, the goal was to obtain an understanding of the shape of a pair of butterfly wings in 3D. The chosen approach was to find a large enough butterfly and perform serial sectioning on it. Reconstruction of sections would picture the butterfly in 3D.

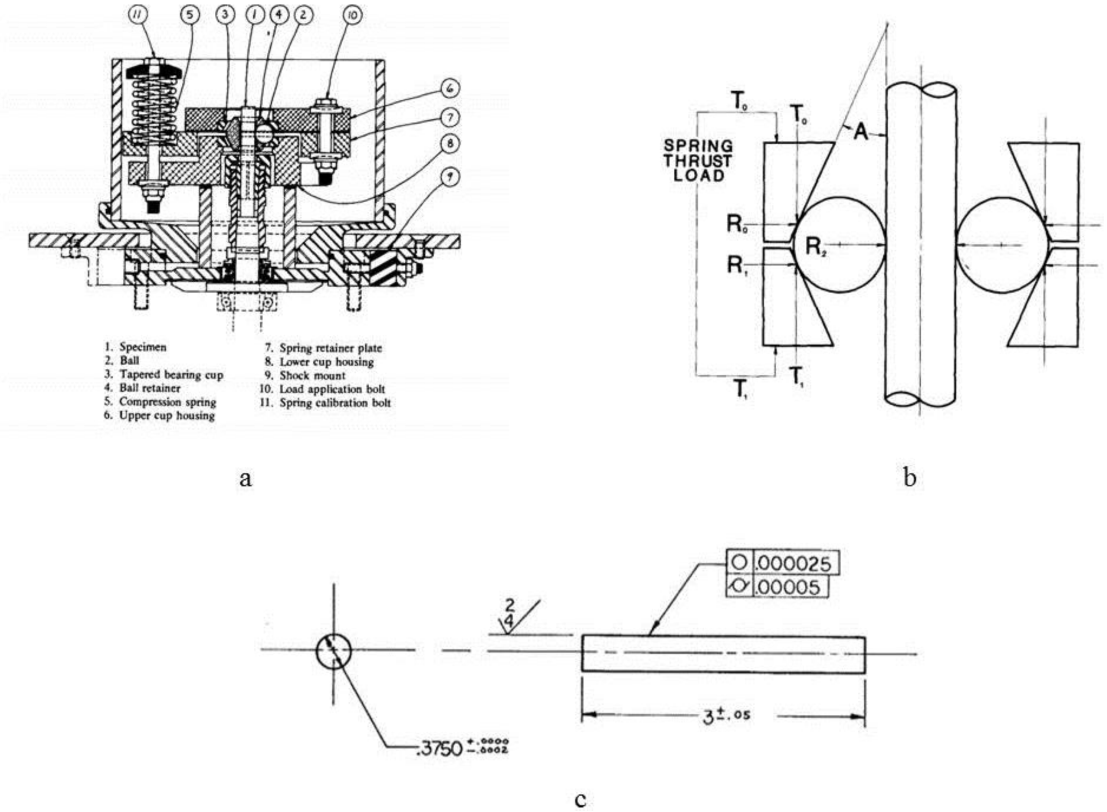

Figure 4.8. Three ball & rod RCF tester. a) Schematic of the components b) geometry of the contact c) specimen geometry. All images are from [126].

4.5.3 Ultrasonic Inspection of Inclusions

Becker [43] in a primary study performed serial sectioning on butterflies; however, his main goal was not to reconstruct the 3D geometric of the butterfly wings. Evans et al. [59] serially sectioned one wing in the transverse plane to find the locations of voids and cracks in the vicinity of butterfly/ matrix interface. In both cases, they missed parts of the butterfly wings since the inclusions are embedded inside the matrix and it is hard to start serial section with very fine steps merely before the butterfly to capture the whole butterfly body. To resolve this issue, it was decided to detect inclusions using ultrasonic inspection first and then conduct serial sectioning at the exact location of the inclusion.

As discussed in the introduction section, NDT methods have recently become popular in the study of RCF. To increase the accuracy, the detection method requires higher wave frequencies. Most researchers have been able to spot anomalies as small as 30 micron in diameter with high reliability when they used ultrasonic waves with frequencies from 50-100 MHz. In the current study, one of the specimens was inspected in collaboration with Sonolabs [127] to find nonmetallic inclusions near the surface. As pictured in Figure 4.9, the inspection was performed with the transducer beam perpendicular to the specimen surface while the whole set up was immersed in a water tank. The goal was to detect the inclusions that are subjected to high values of Hertzian stress. Considering the fact that the minor and major axes of contact were calculated to be 260 and 472 microns, inclusions within 300 micron from the surface of the specimen were inspected. It was found out that the first 150 microns below the surface are a dead zone since the reflections from the surface interrupts the possible reflections from the inclusions. Combination of ultrasonic reflections from all over the specimen surface provides a C-Scan (known as C-Mode Scanning Acoustic Microscope (C-SAM)) of the whole specimen.

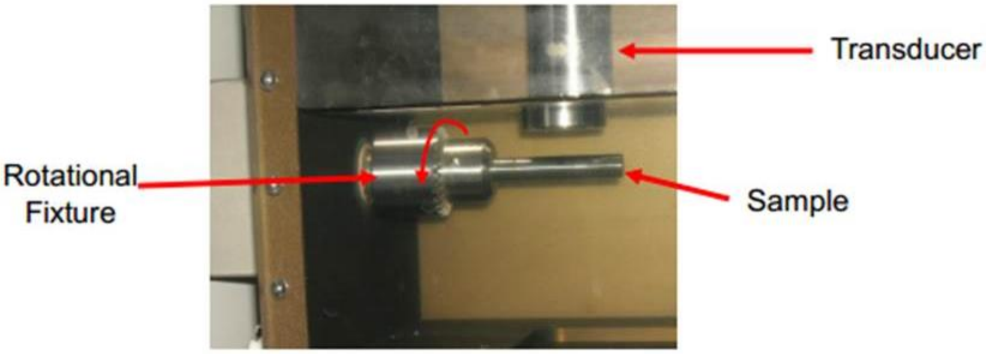

Figure 4.9. RCF specimen installed in the ultrasound. Image courtesy: Sonolabs Inc. [127].

Figure 4.10 shows the raw C-scan of the specimen; the colormap shows the depths at which the inclusions are found. A close up view of one of the inclusions is shown in the zoomed frame. The pixel size of the raw C-scan is about 30 micron by 30 micron. Similar to previous investigations, this is an estimation of the smallest inclusion size which is detectable by this method. Since the relative size of the inclusions to the specimen size is very small, Figure 4.10 by itself is not very useful. So, Figure 4.10 is post processed to exaggerate the inclusion sizes so that it is easier to observe the location of spotted inclusions, as illustrated in Figure 4.11.

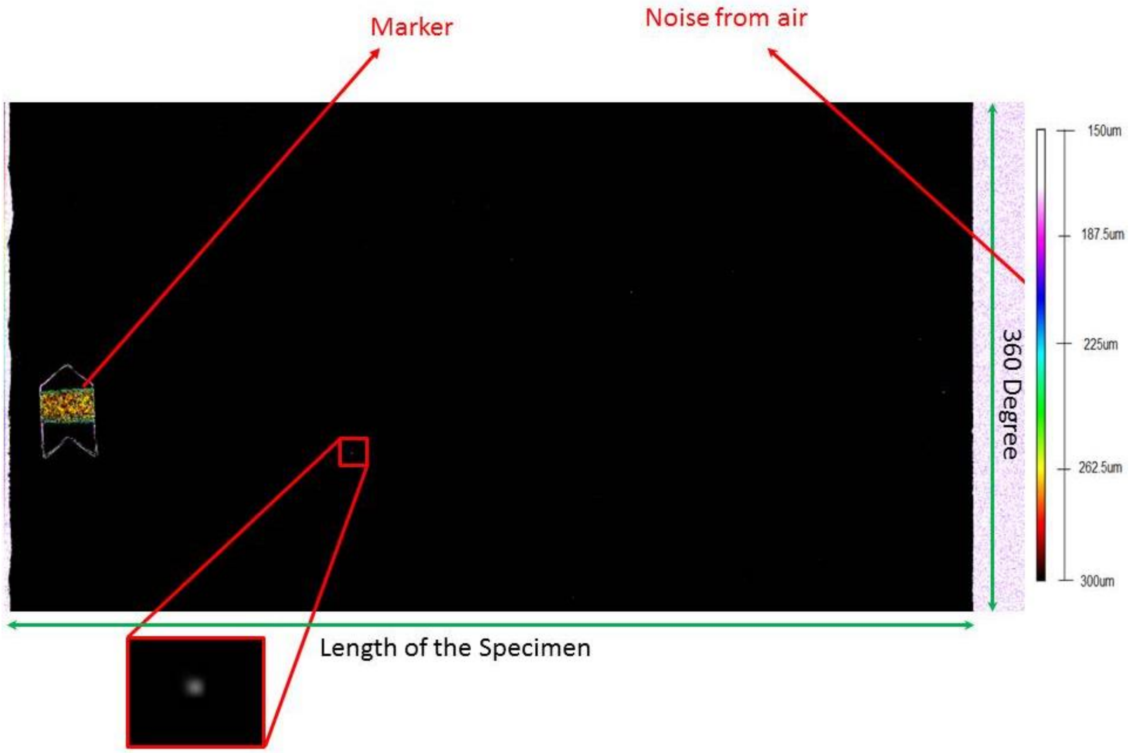

Figure 4.10. Raw C-scan of the RCF specimen with a close up view of an inclusion which was chosen for serial sectioning. The color map indicates the depth of the inclusions.

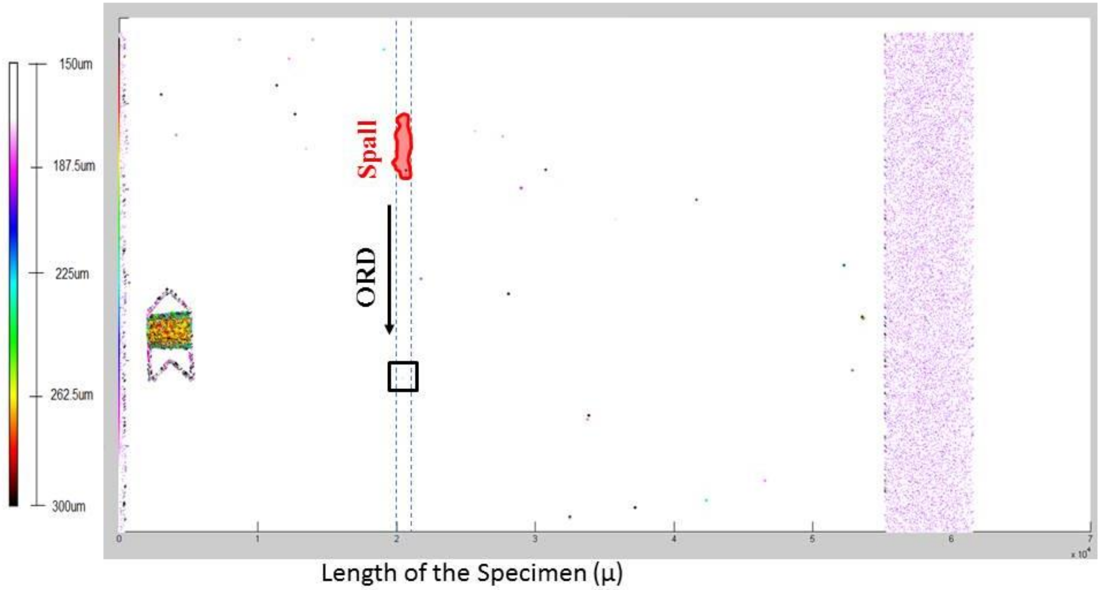

Figure 4.11. Post processed C-scan of the RCF specimen. The dashed lines show the wear track approximately. The square indicates the location of the serially sectioned inclusion.

4.6 Results

4.6.1 Analytical Serial Sectioning

The 3D model described earlier was exercised in a shell script and a C++ post processor code was used to update damage in each cycle. To make the phase transition smoother and to increase the accuracy of the model, the ΔD value in each cycle was set to 0.01. This way, after ten loading cycle, the first element was converted from martensite to ferrite. The simulation was run to model the wing propagation. The criterion to stop the simulation was the appearance of the second pair of wings because it seems that it is the point beyond which the accuracy of the model reduces. Figure 4.12. illustrates the initiation and growth of butterfly wings around the inclusion chronologically; the fully grown wings are shown from side and top view as well for the purpose of better illustration.

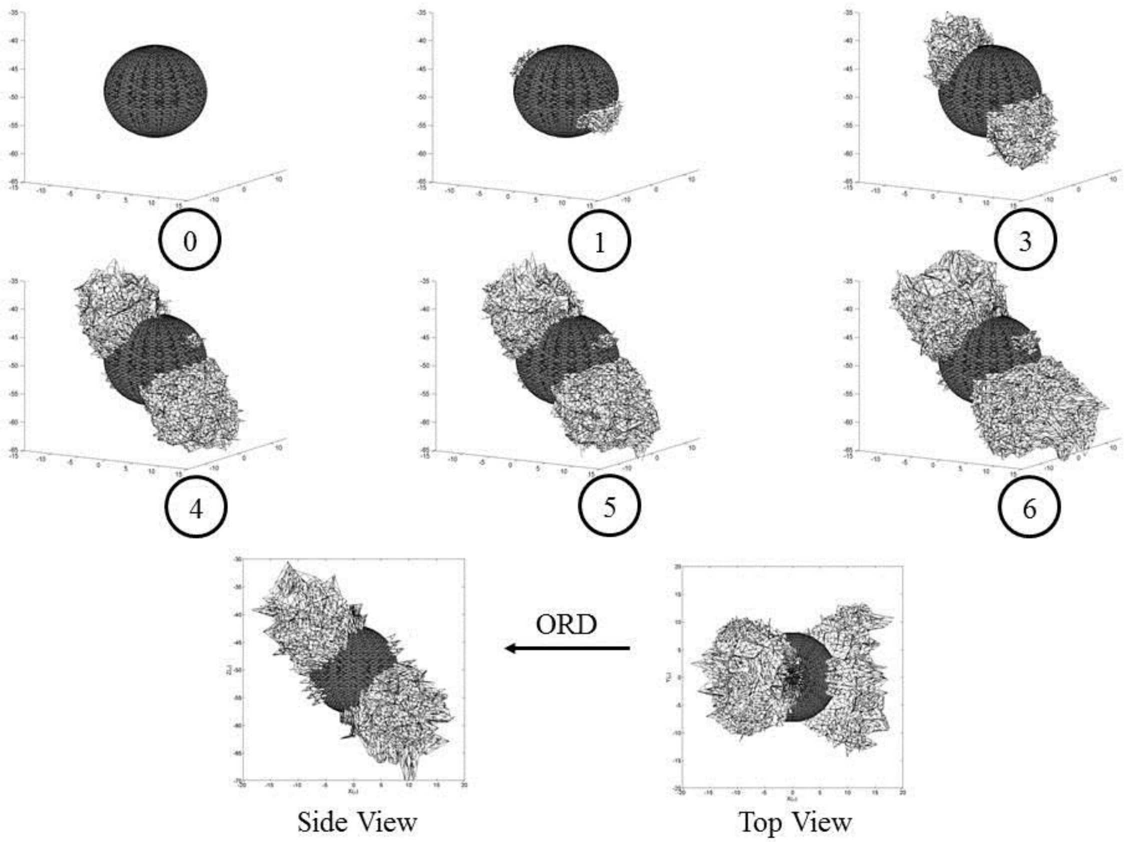

Figure 4.12. Chronological order of butterfly initiation and evolution in 3D. The side view and top view of frame #6 is included for better illustration.

It should be noted that in almost all the experimental works that are concerned with the study of butterfly formation, the microstructural alteration are observed in the 2D planes that are cut and polished after failure. Consequently to confirm the validity of the geometrical shape of the wings in 3D, it is necessary to take a step back and cut the simulated butterfly in different planes and look at the different cut sections. Hereafter in this paper, this procedure is referred to as “analytical serial sectioning”. Figure 4.13, shows the analytical serial sectioning procedure in 3D and the 2D views of the cut sections while the inclusion and wings are cut in planes parallel to the ORD. As can be seen, in the sections # 4-7, the wings appear separately without an inclusion connected to them. Indeed, this can be observed further in the top view of the 3D model in Figure 4.12 where the lateral expansion of the wings is visible beyond the inclusion extents into the transverse plane. The inclusion-less wings which are observed in the analytical serial sectioning are very similar to the white features observed in Figure 4.3. Figure 4.12 shows that the lateral extents of the wings are the last parts to appear in the evolution process of a pair of wings. This observation suggests if the rolling contact loading is continued for long enough, the wings can grow laterally beyond the inclusion extents. This may explain the observation of white features in other works as well [76,121,122]. However, an experimental serial sectioning was necessary to be performed on an inclusion to confirm this idea, which is presented in the next section to keep the continuity of the presentation of the analytical results.

4.6.2 Wingspan to Inclusion Ratio

The authors had investigated the wingspan to inclusion ratio for different inclusion sizes, in an earlier study [93] and compared the analytical results with the experimental results by Lewis and Tomkin [11]. Those results are repeated here for reference, in Figure 4.14. As can be seen, the ratio predicted by the model closely matched the lower bound of the experimental data; however, the 2D model was incapable of explaining the large deviation of the upper bound of the experimental data.

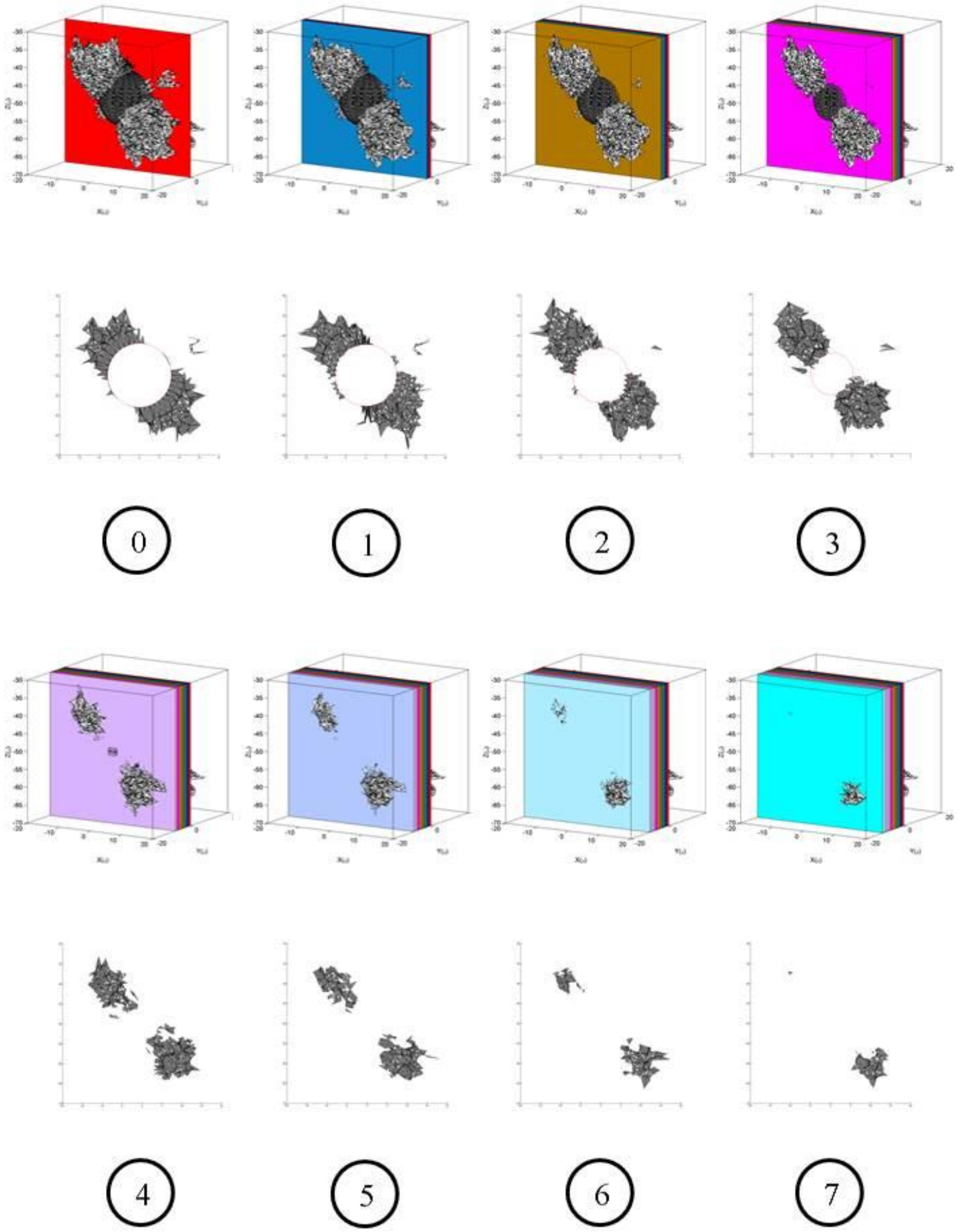

Figure 4.13. Analytical serial sectioning procedure. Note the existence of butterfly wings without any observed inclusion in sections 5, 6, and 7.

It should be noted that the aforementioned study was conducted in 2D and neglected the 3D shape of the inclusion. On the other hand, the experimental data was collected by sectioning the actual inclusions at random cross sections. Consequently, the same experimental data were analyzed again and compared with the new 3D model.

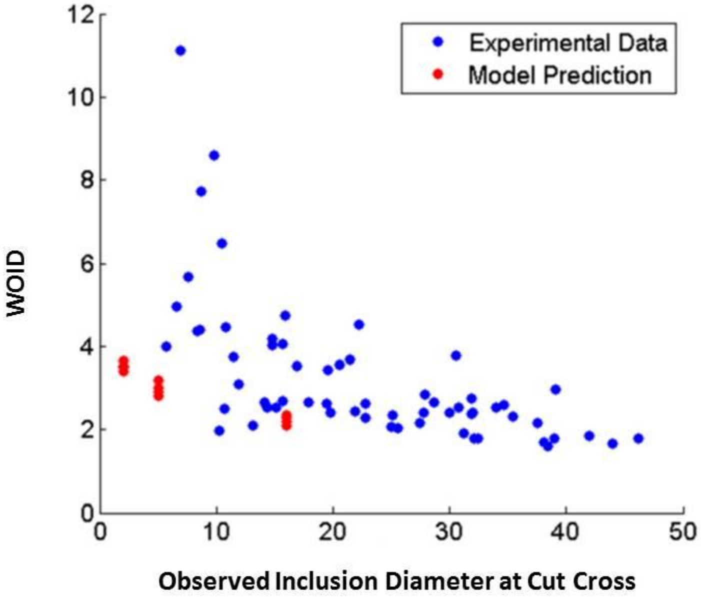

Figure 4.14. Wingspan observed to inclusion diameter (WOID) as obtained by Mobasher Moghaddam et al. [6] for a 2D model.

Looking at Figure 4.15-a, it seems that the wing span is almost constant in all the cross sections. Neglecting the slight variation in the wingspan size that happen due to the mesh geometry, the wing span is assumed to be constant over the width of butterfly. This assumption is schematically shown in Figure 4.15-b on the top view of the butterfly. The value of this constant wing span, is measure to be about two times the inclusion diameter in 3D. This is very similar to what Tsunekage et al. [128] suggested for the wingspan of butterflies. It should be noted that the inclusion diameter in 2D cross sections can be *seen* to be different based on the plane at which the inclusion is cut. Based on the above assumptions, the following geometrical equation was derived to calculate the wingspan to inclusion ratio analytically:

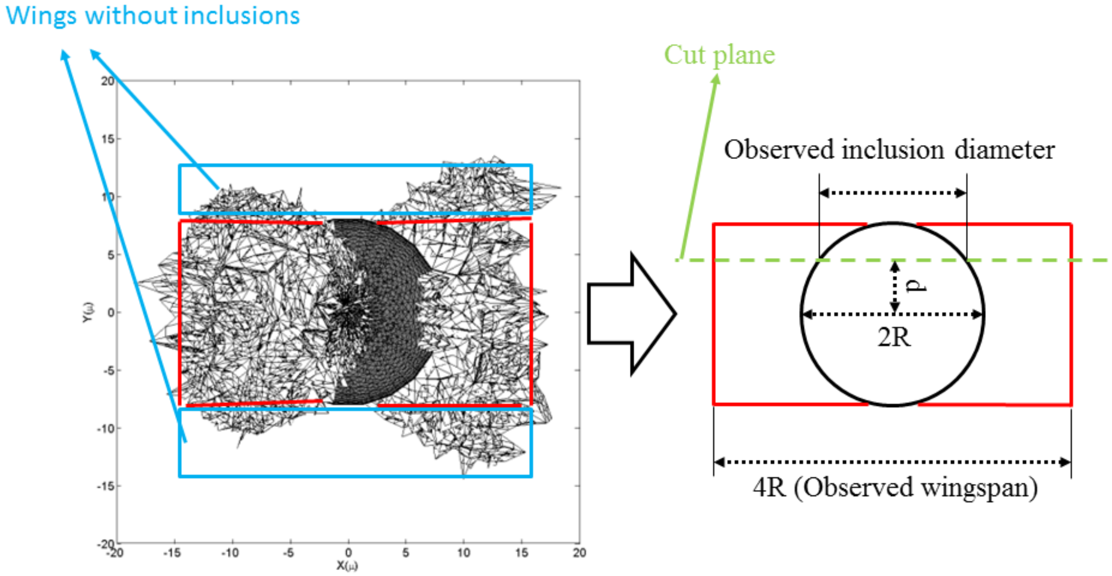

a

b

Figure 4.15. Top view of an inclusion and the schematic of the variables describing the wingspan to inclusion diameter ratio.

$$WOID = \frac{2}{\sqrt{1-\left(\frac{d}{R}\right)^2}} \tag{4.5}$$

Where d is the distance of the cut plane from the center of the inclusion and R is the actual spherical inclusion radius. It should be noted that d is confined to be between 0 and R. To compare this equation with the experimental data R needs to be determined. For this purpose, it is assumed that the data points near the line at which wingspan to inclusion diameter is equal to 2 (shown with dashed line in Figure 4.16) reflect the actual inclusion diameter since data points on this line represent inclusions that are cut near their center plane. Considering Eq. (4.5), this corresponds to a very small value of *d*. Following this assumption, the lower and upper bound of the data on the dashed line are set to be the smallest and largest inclusion sizes to which Eq. (4.5) is applied (10 and 50 microns respectively). Figure 4.16 shows these results altogether. It can be seen that the closed form analytical solution suggested in this study follows the experimental data closely. (It should be noted that it is not practically possible to obtain experimental data on the very left side of plot since the observed inclusion diameter virtually reaches zero.)

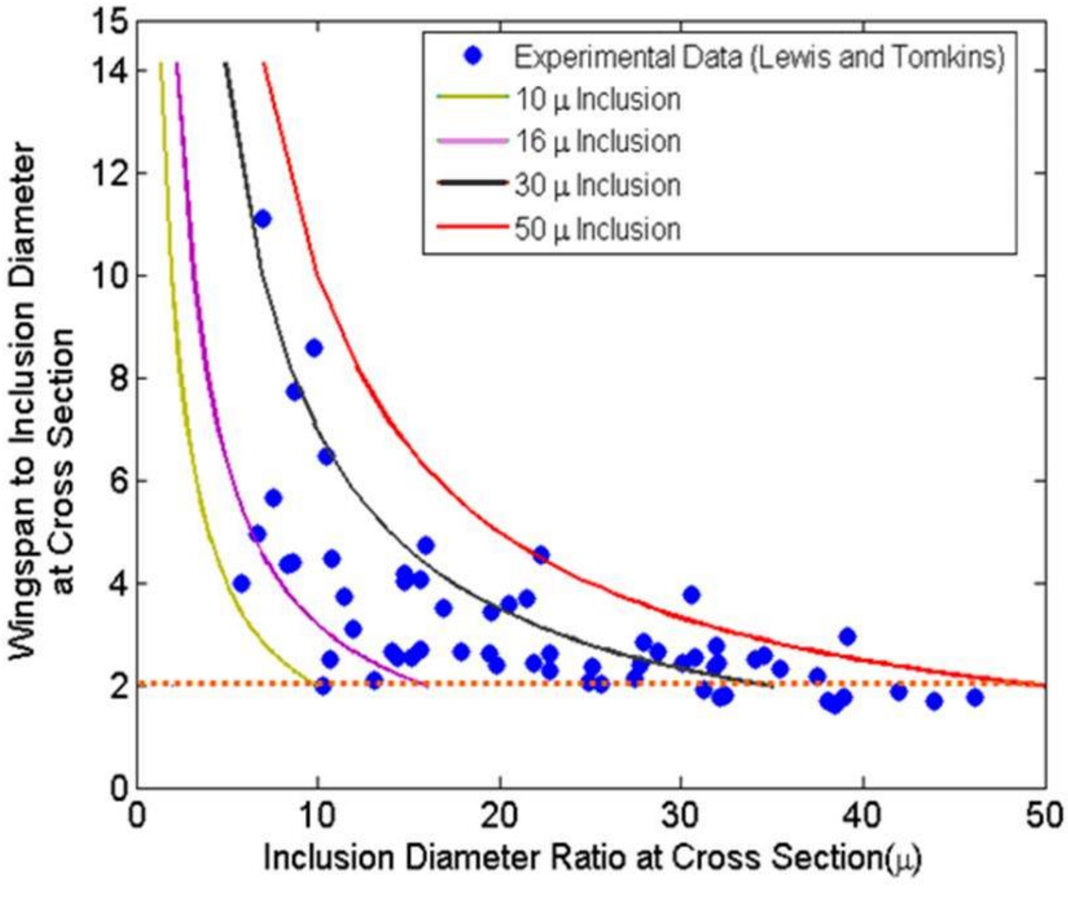

Figure 4.16. Comparison of experimental and analytical wingspan to inclusion diameter ratios of 2D sections in 3D.

4.6.3 Experimental

The main goal of this part of investigation was to conduct an experimental serial sectioning on an inclusion with butterflies to confirm the analytical serial sectioning results. RCF tests have been conducted at 2.0 GPa on 3ball & rod machine on a specimen made of AISI 8620 bearing steel. The specimen used for RCF tests is the very same one which was previously inspected using an ultrasound. The dashed lines in Figure 4.11 show the wear track on the specimen. The approximate geometry of the spall is illustrated as well. The spall was formed on top of two of the spotted inclusions; however, the spall was relatively deep and it seemed that the inclusions were detached from the matrix during spalling. Hence, it was not possible to confirm the effect of these inclusions on the spall formation with great certainty. Instead, another inclusion, pointed at with a square, was chosen for serial sectioning.

To reconstruct a 3D body from a number of parallel 2D sections, it is necessary to know the spacing between the sections. For this purpose, an approach similar to Evans et al. [46] was used. In this method, Vicker's indenters were used to mark the cut section. By knowing the geometry of the indent, it is possible to estimate the material removal by observing the reduction in the size of the indent under the microscope. Figure 4.17 depicts the serial sectioning result for the aforementioned butterfly with approximately 1 micron spacing between the sections. As can be seen, similar to Figure 4.13, the serial sectioning of the butterfly confirms the presence of the wings on the two sides of the inclusion in the planes parallel to ORD (sections 1, 2, and 11-15).

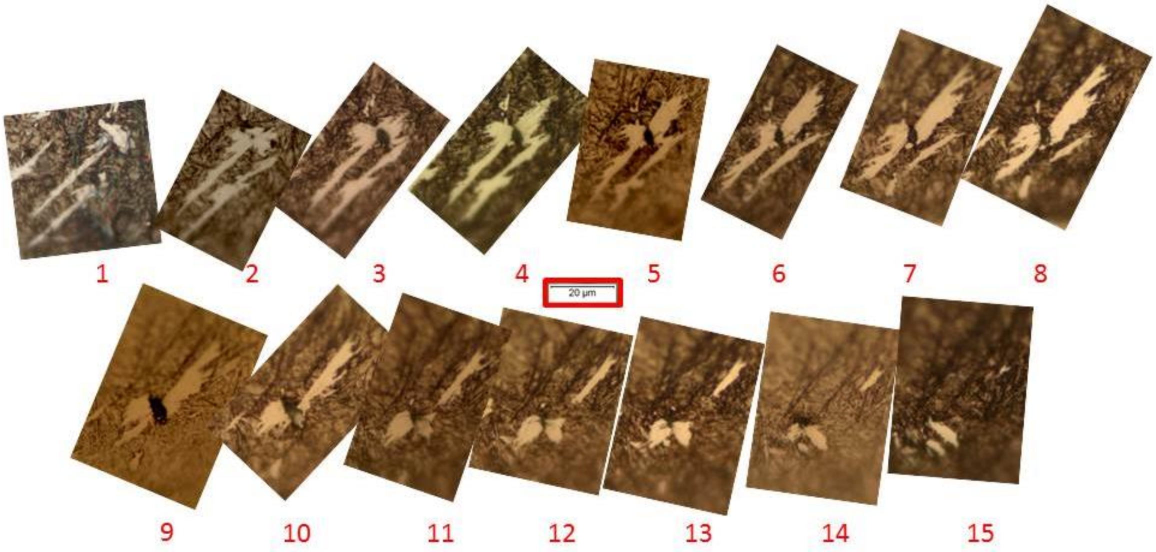

Figure 4.17. Experimental serial sectioning of an inclusion. Note the presence of inclusion- less butterflies at sections 1, 2, and 11-15.

To reconstruct a 3D body from a number of parallel 2D sections, it is necessary to know the spacing between the sections. For this purpose, an approach similar to Evans et al. [58] was used. In this method, Vicker's indenters were used to mark the cut section. By knowing the geometry of the indent, it is possible to estimate the material removal by observing the reduction in the size of the indent under the microscope. Figure 4.17 depicts the serial sectioning result for the aforementioned butterfly. As can be seen, similar to Figure 4.13, the serial sectioning of the butterfly confirms the presence of the wings on the two sides of the inclusion in the planes parallel to ORD (sections # 1, 2, and 11-15).

4.7 Summary and Conclusions

The current work implements experimental and analytical techniques to tackle butterfly wing formation around nonmetallic inclusions in bearing steel. A 3D FE model is coupled with a postulated damage law to simulate microstructural alterations around inclusions. The model was exercised to simulate the wing formation. Analytical serial sectioning illustrated that how the butterfly, as a 3D object, may appear in 2D planes under the microscope. High frequency ultrasonic inspection was used to detect the inclusions inside the bearing steel. Serial sectioning on of such inclusions was performed. Both numerical and experimental serial sectioning showed that if the RCF test continues for long enough, the butterfly wings can expand laterally beyond the inclusion bounds. Wingspan to inclusion ratio was calculated at different sections of the analytical model. A closed form solution based on the observations was suggested to predict the wingspan to inclusion ratio at different cut cross sections of the inclusions. The analytical results were compared with the experimental data available in the open literature and shows a close corroboration.

CHAPTER 5. SUMMARY, DEVELOPMENTS IN PROGRESS, AND SCOPE OF FUTURE WORK

The current investigation presents a comprehensive literature review of a phenomenon called butterfly wing formation in bearing steels. Butterfly wings are areas of microstructurally altered material around inclusions which can lead to fatigue crack initiation in RCF. In the first stage, a 2D FE simulation is coupled with a postulated damage theory to predict wing formation by taking the effect of alternating and mean shear stress into account. The model is exercised and the results are compared with the experiments by other authors that are available in open literature. It was found that the model is capable of predicting butterfly wing shape, size, and orientation similar to experimental observations. Moreover, the SN curve for wing formation was compared to experimental findings and a close corroboration was observed specifically at the low load range where most of the wind turbine bearings operate. Finally, maximum shear stress was resolved along the inclusion/matrix interface as a criterion to locate the inclusion debonding regions. The results showed good agreement with the recent experimental observations.

In the next step, the 2D model is extended to relate the butterfly formation to crack initiation and propagation in the steel. Critical damage value is experimentally measured using nanoindentation tests. Also, a new variable is introduced to assess the material vulnerability to form butterflies versus depth. A relative RCF life comparison was conducted to explore the effect of inclusion size, stiffness, and depth on RCF life.

Finally, the investigation was extended to 3D to account for the end effects due to globular shape of the inclusions. Experimental and numerical analysis showed that the butterfly formation in 3D can propagate beyond the inclusion extends in the transverse planes. Serials sectioning of the butterflies suggested a closed form solution which presents a reasonably accurate approximation for the wing span to inclusion ratio at different cross sections.

5.1 Ideas for Future Development

5.1.1 In-Situ Monitoring of Butterfly Wing Progression

As discussed throughout this document, most of the experimental studies on butterfly wings consist of destructive post-failure analysis. One of the major areas yet to be investigated is nondestructive analysis of butterfly progression rate versus the loading cycles. This can provide us with important information regarding the primary stages of the crack development inside the matrix.

NDTs have recently been implemented to find the butterflies in-situ. As mentioned in Chapter 4 extensively, among the different techniques, ultrasonic detection and X-ray tomography have been proven to effectively trace inclusions and butterflies inside the steel. Each method is known to have its own pros and cons. In most of the cases, researchers have been able to exploit ultrasounds to detect inclusions as small as 30 micron in diameter. This resolution is not sufficient to spot the very early stages of crack initiation near the inclusions. Moreover, ultrasonic detection is sensitive to the surface quality of the samples.

It is evident that running a ball or a roller on top of the inclusions will generate a wear track which changes the surface profile and quality of the material in the region of interest continuously. This makes it more difficult to use ultrasounds for in-situ monitoring of the crack propagation [129].

X-ray tomography has two major advantages when compared to ultrasonic detection: i) it provides better inspection accuracy. Modern X-ray techniques are capable of detecting inclusions as small as 0.5 micron in diameter [130], ii) The performance of the method is almost independent of the surface roughness. Hence, it would be possible to use the method while the wear track is evolving over the cycles. However, there is a downside associated with X-ray inspection and it is the large size of data files which makes it almost impossible to inspect a whole sample using this method [131].

The author suggests a hybrid NDT method to achieve the maximum detection accuracy while the inspection time remains reasonable. The suggested method is comprised of a two stage inspection procedure. In the first stage, ultrasonic detection is implemented to spot the inclusions as small as 30 micron in diameter. Then, while the RCF tests are run, X-ray tomography will be conducted only at certain inclusion locations and at predefined intervals to precisely track the microstructural changes in the vicinity of the inclusions in the embryonic stages.

5.2 Effect of Hydrogen Diffusion on Torsion Fatigue

As mentioned in Chapter 1, WECs are one of the most important failure causes in heavy duty bearings and gears. Replicating the exact circumstances under which WECs form is very hard since the root causes for WEC formation is not exactly known; however, WEC reproduction in the laboratory has been possible with the aid of Hydrogen charging [18,27,29,132–136].

There are different methods used to charge steel with Hydrogen, The most common ones are electric charging, charging with acids, and charging with NH_4SCN [29]. While electric charging [28] is more difficult and not applicable to complex geometries and charging using an acid can cause surface damage, NH_4SCN has been the most popular method in the recent years [27,29].

Research has shown that charging bearing steel with 20%wt solution of NH_4SCN can cause formation of WECs inside the bearing steel during RCF tests. This is commonly accompanied with significant fatigue life reduction, similar to what is observed in Hydrogen embrittlement phenomena. Uyama et al. [24] showed that the concentration of NH_4SCN strongly affects WEC formation. Figure 5.1 shows WECs formation for different densities of NH_4SCN solution. Hamada and Matsubara [137,138] showed that charging high strength steels with Hydrogen can reduce the life up to two orders of magnitude. It should be noted that their tests have been uniaxial fatigue tests while RCF is a more complicated phenomenon as discussed before. It has been suggested that torsion fatigue tests can be studied as an alternative to RCF since in both cases shear stress is the dominant stress component that governs the fatigue life [71,139]. For this purpose, the author suggests conducting torsion fatigue tests with and without Hydrogen to study the effect of Hydrogen diffusion on Mode II crack initiation. Fujita et al. [134] have already investigated the effect of Hydrogen charging on shear dominated crack growth. Although the SN curve they produced shows a clear fatigue life reduction, it is comprised of only three data points which is not enough for a highly scattered phenomenon like fatigue.

Moreover, as will be discussed, Fujita et al. [134] have not counted for the possible effects of Hydrogen effusion from the steel. Consequently, it is necessary to develop a more in depth understanding of Hydrogen diffusion in torsion fatigue. For this purpose, torsion tests will be conducted with the aid of a MTS torsion rig which is available at METL facilities.

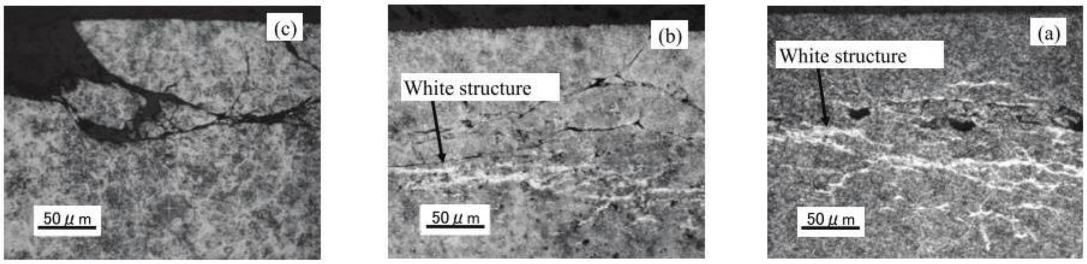

Figure 5.1. Microstructure adjacent to flaking in the Hydrogen charged specimens : a) 20% mass NH_4SCN, b) 1% mass NH_4SCN, c) 0.3% mass NH_4SCN.

As discussed, most of the charged Hydrogen can escape from the steel matrix if there is no source providing Hydrogen to the steel during the fatigue tests. The reason is mainly due to very small size of Hydrogen atoms: Hydrogen can easily penetrate through the matrix; on the other hand, it can easily escape out from the steel as well. Figure 5.2, borrowed from [85] describes the Hydrogen effusion from the matrix versus time. As can be seen, the majority of charged Hydrogen can effuse from the steel if the fatigue test takes place for long enough. To resolve this issue, a special chamber is designed to encompass the torsion specimen and charge it in-situ. The designed, set up is shown in Figure 5.3, and a close up view of the container is depicted in Figure 5.4. NH_4SCN solution is kept at 50 C throughout the tests and a positive displacement pump is used to feed the chamber with solution all the time.

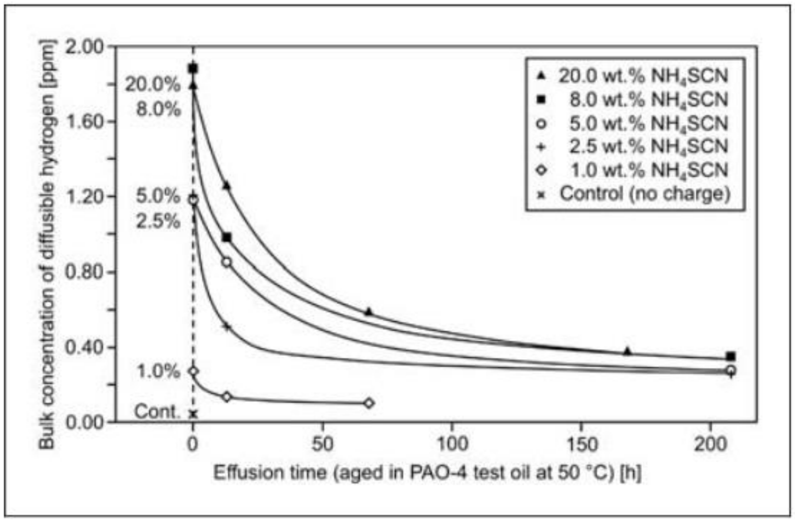

Figure 5.2. Hydrogen effusion vs. time for different NH_4SCN solution concentrations [85].

The tests results will show the SN behavior of the steel for both charged and uncharged conditions. Then, new damage parameters would be obtained and a comprehensive damage law which accounts for the effect of Hydrogen embrittlement would be used to predict RCF life.

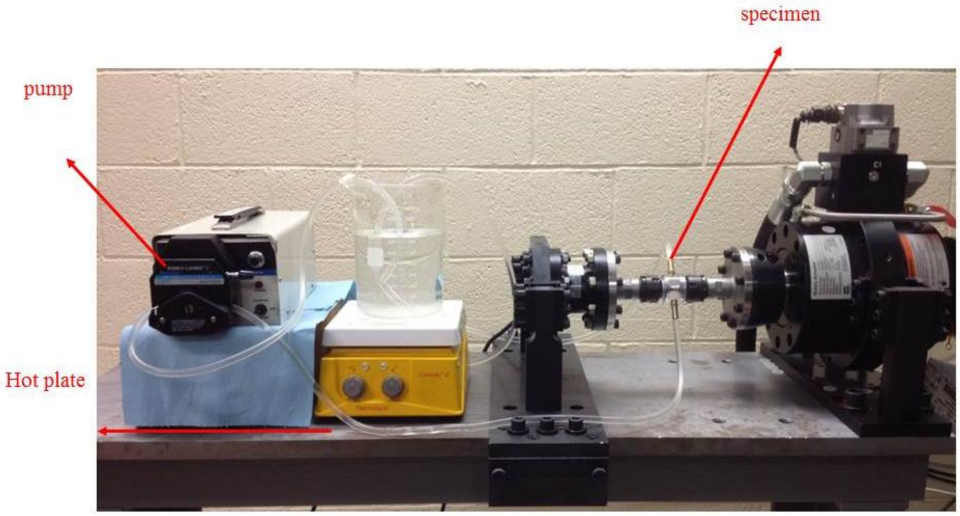

Figure 5.3. Modified MTS torsion rig capable to charge specimens with Hydrogen in-situ.

The validity of the RCF simulations can be checked by conducting actual RCF tests with the three-ball-on-rod rig for pristine as well as Hydrogen charged rods. The corresponding RCF model can advance further by modeling the Hydrogen diffusion phenomenon as well. This can be accomplished by either using a 1D iterative model similar to Kadin [33,34] or a simplified 2D model similar to Warhadpande et al. [26].

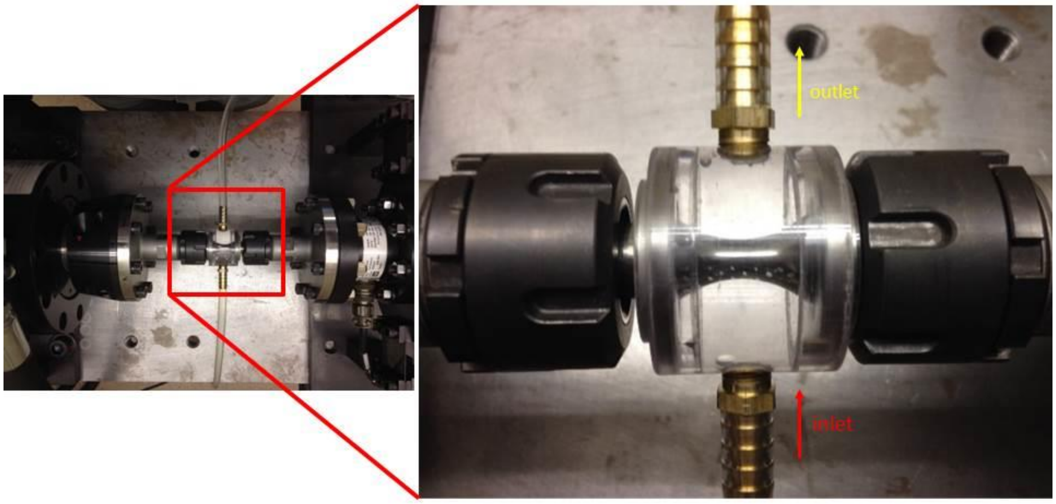

Figure 5.4. A close up view of the custom made chamber for Hydrogen charging.

LIST OF REFERENCES

LIST OF REFERENCES

[1] Dowson, D., 1979, History of Tribology, Addison-Wesley Longman Limited.

[2] Zaretsky, E., A Basis for Bearing Life Prediction. National Aeronautics and Space Administration, 1997.

[3] Lundberg, G., and Palmgren, A., 1947, “Dynamic Capacity of Rolling Element Bearings,” Acta Polytech. Scand., Mech. Eng. Ser, 1(3), pp. pp. 1–50.

[4] Styri, H., "Fatigue strength of ball bearing races and heat-treated 52100 steel specimens." In PROCEEDINGS-AMERICAN SOCIETY FOR TESTING AND MATERIALS, vol. 51, p. 682., PA 19428-2959: AMER SOC TESTING MATERIALS, 1951.

[5] Grabulov, A., Petrov, R., and Zandbergen, H. W., 2010, “EBSD investigation of the crack initiation and TEM/FIB analyses of the microstructural changes around the cracks formed under Rolling Contact Fatigue (RCF),” Int. J. Fatigue, 32(3), pp. 576–583.

[6] Swahn, H. P. C. O., Becker, C., and Vingsbo, O., "Martensite decay during rolling contact fatigue in ball bearings." Metallurgical transactions A 7, no. 8 (1976): 1099-1110.

[7] Greco, A., and Erdemir, A., "Bearing Reliability–White Etching Cracks (WEC)." Argonne National Laboratory, Energy Systems Division, NREL Gearbox Reliability Collaborative (2013).

[8] Zwirlein, O., and Schlicht, H., "Rolling contact fatigue mechanisms—accelerated testing versus field performance." Rolling Contact Fatigue Testing of Bearing Steels 771 (1982): 358-379.

[9] Warhadpande, A., Sadeghi, F., and Evans, R. D., 2013, “Microstructural Alterations in Bearing Steels under Rolling Contact Fatigue Part 1—Historical Overview,” Tribol. Trans., 56(3), pp. 349–358.

[10] Holweger, W., "Influence on bearing life by new material phenomena." InNREL-Wind Turbine Tribology Seminar, November, pp. 15-17. 2011.

[11] Lewis, M. W. J., and Tomkins, B., 2012, “A fracture mechanics interpretation of rolling bearing fatigue,” Proc. Inst. Mech. Eng. Part J-Journal Eng. Tribol., 226(J5), pp. 389–405.

[12] Furumura, K., Murakami, Y., and Abe, T., "The development of bearing steels for long life rolling bearings under clean lubrication and contaminated lubrication." ASTM SPECIAL TECHNICAL PUBLICATION 1195 (1993): 199-199.

[13] Kang, J. H., Hosseinkhani, B., Williams, C. A., Moody, M. P., Bagot, P. A. J., and Rivera-Díaz-Del-Castillo, P. E. J., 2013, “Solute redistribution in the nanocrystalline structure formed in bearing steels,” Scr. Mater., 69(8), pp. 630–633.

[14] Martin, J. A., Borgese, S. F., and Eberhardt, A. D., "Microstructural alterations of rolling—bearing steel undergoing cyclic stressing." Journal of Fluids Engineering 88, no. 3 (1966): 555-565

[15] Bush, J. J., and Grube, W. L., “Microstructural and residual stress changes in hardened steel due to rolling contact,” Trans. ASM, 54, pp. 390–412.

[16] Thielen, P., Morris E., and Fournelle, R. A., 1976, “Cyclic stress strain relations and strain-controlled fatigue of 4140 steel,” Acta Metall., 24(1), pp. 1–10.

[17] Bhattacharyya, A., Subhash, G., and Arakere, N., 2014, “Evolution of subsurface plastic zone due to rolling contact fatigue of M-50 NiL case hardened bearing steel,” Int. J. Fatigue, 59, pp. 102–113.

[18] Ruellan, A., Ville, F., Kleber, X., Arnaudon, A., and Girodin, D., 2014, “Understanding white etching cracks in rolling element bearings: The effect of hydrogen charging on the formation mechanisms,” Proc. Inst. Mech. Eng. Part J J. Eng. Tribol.

[19] Oila, A., Shaw, B. A., Aylott, C. J., and S. J. Bull. "Martensite decay in micropitted gears." Proceedings of the Institution of Mechanical Engineers, Part J: Journal of Engineering Tribology 219, no. 2 (2005): 77-83.

[20] Polonsky, I. A., and Keer, L. M., "On white etching band formation in rolling bearings." Journal of the Mechanics and Physics of Solids 43, no. 4 (1995): 637-669.

[21] Forster, N. H., Rosado, L., Ogden, W. P., and Trivedi, H. K., 2009, “Rolling Contact Fatigue Life and Spall Propagation Characteristics of AISI M50, M50 NiL, and AISI 52100, Part III: Metallurgical Examination,” Tribol. Trans., 53(1), pp. 52–59.

[22] Bearing, T. T., 1970, “The Toyo Bearing,” 15.

[23] Gegner, J., and Nierlich, W., 2011, “Hydrogen Accelerated Classical Rolling Contact Fatigue and Evaluation of the Residual Stress Response,” Mater. Sci. Forum, 681, pp. 249–254.

[24] Uyama, H., Yamada, H., Hidaka, H., and Mitamura, N., 2011, “The Effects of Hydrogen on Microstructural Change and Surface Originated Flaking in Rolling Contact Fatigue,” Tribol. Online, 6(2), pp. 123–132.

[25] Holweger, W., Walther, F., Loos, J., Wolf, M., Schreiber, J., Dreher, W., Kern, N., and Lutz, S., 2012, “Non-destructive subsurface damage monitoring in bearings failure mode using fractal dimension analysis,” Ind. Lubr. Tribol., 64(3), pp. 132–137.

[26] Warhadpande, A., Sadeghi, F., and Evans, R. D., 2013, “Microstructural Alterations in Bearing Steels under Rolling Contact Fatigue: Part 2—Diffusion-Based Modeling Approach,” Tribol. Trans., 57(1), pp. 66–76.

[27] Evans, M. H., Richardson, A. D., Wang, L., and Wood, R. J. K., 2013, “Effect of hydrogen on butterfly and white etching crack (WEC) formation under rolling contact fatigue (RCF),” Wear, 306(1-2), pp. 226–241.

[28] Vegter R. H., and Slycke, J. T., "The role of hydrogen on rolling contact fatigue response of rolling element bearings." Journal of ASTM International7, no. 2 (2009): 1-12.

[29] Tanimoto, H., Tanaka, H. and Sugimura, J., 2011. Observation of Hydrogen Permeation into Fresh Bearing Steel Surface by Thermal Desorption Spectroscopy. Tribology Online, 6(7), pp.291-296.

[30] Grujicic, M., Chenna, V., Yavari, R., Galgalikar, R., Snipes, J. S., and Ramaswami, S., 2015, “Multi-length scale computational analysis of roller-bearing premature failure in horizontal-axis wind turbine gear boxes,” Int. J. Struct. Integr., 6(1), pp. 40–72.

[31] Grujicic, M., Ramaswami, S., Yavari, R., Galgalikar, R., Chenna, V., and Snipes, J., 2014, “Multiphysics computational analysis of white-etch cracking failure mode in wind turbine gearbox bearings,” Proc. Inst. Mech. Eng. Part L J. Mater. Des. Appl., 0(0), pp. 1–21.

[32] Grujicic, M., Chenna, V., Galgalikar, R., Snipes, J. S., Ramaswami, S., and Yavari, R., "Wind-Turbine Gear-Box Roller-Bearing Premature-Failure Caused by Grain-Boundary Hydrogen Embrittlement: A Multi-physics Computational Investigation." Journal of Materials Engineering and Performance 23, no. 11 (2014): 3984-4001.

[33] Kadin, Y., 2013, “Modeling of hydrogen transport in rolling contact fatigue conditions,” Procedia Eng., 66(July), pp. 415–424.

[34] Kadin, Y., 2015, “Modeling of Hydrogen Transport in Static and Rolling Contact,” Tribol. Trans., 58(2), pp. 260–273.

[35] Jalalahmadi, B., Sadeghi, F., and Bakolas, V., 2011, “Material Inclusion Factors for Lundberg-Palmgren–Based RCF Life Equations,” Tribol. Trans., 54(3), pp. 457–469.

[36] Takemura, H., Matsumoto, Y., and Murakami, Y., " Development of a new life equation for ball and roller bearings". No. 2000-01-2601. SAE Technical Paper, 2000.

[37] Kerrigan, A., Kuijpers, J. C., Gabelli, A., and Ioannides, E., "Cleanliness of bearing steels and fatigue life of rolling contacts." J ASTM Int 3 (2006).

[38] Schlicht, H., Schreiber, E., and Zwirlein, O., "Effects of material properties on bearing steel fatigue strength." Effect of steel manufacturing processes on the quality of bearing steels (1986): 81-101.

[39] Furumura, K., Murakami, Y., and Abe, T., "Development of long life bearing steel for full film lubrication and for poor and contaminated lubrication." Motion Control 1 (1996): 30-36.

[40] Niu, L. J., Velay, X., and Sheppard, T., 2012, “On material flow and aspects of structural modification during direct and indirect extrusion of aluminium alloy,” Mater. Sci. Technol., 28(4), pp. 397–405.

[41] Evans, M.-H., 2012, “White structure flaking (WSF) in wind turbine gearbox bearings: effects of ‘butterflies’ and white etching cracks (WECs),” Mater. Sci. Technol., 28(1), pp. 3–22.

[42] Bhadeshia, H. K. D. H., 2012, “Steels for bearings,” Prog. Mater. Sci., 57(2), pp. 268–435.

[43] Becker, P. C., 1981, “Microstructural changes around non-metallic inclusions caused by rolling-contact fatigue of ball-bearing steels,” Met. Technol., 8(1), pp. 234–243.

[44] Evans, M. H., Walker, J. C., Ma, C., Wang, L., and Wood, R. J. K., 2013, “A FIB/TEM study of butterfly crack formation and white etching area (WEA) microstructural changes under rolling contact fatigue in 100Cr6 bearing steel,” Mater. Sci. Eng. A, 570, pp. 127–134.

[45] Grabulov, A., and Zandbergen, H. W., “TEM and Dual Beam (SEM / FIB) investigations of subsurface cracks and White Etching Area (WEA) formed in a deep groove ball bearing caused by Rolling Contact Fatigue (RCF).”

[46] Grabulov, A., Ziese, U., and Zandbergen, H. W., 2007, “TEM/SEM investigation of microstructural changes within the white etching area under rolling contact fatigue and 3-D crack reconstruction by focused ion beam,” Scr. Mater., 57(7), pp. 635–638.

[47] Errichello, R., Budny, R., and Eckert, R., 2013, “Investigations of Bearing Failures Associated with White Etching Areas (WEAs) in Wind Turbine Gearboxes,” Tribol. Trans., 56(6), pp. 1069–1076.

[48] Oila, A, Shaw, B. A, Aylott, C. J., and Bull, S. J., 2005, “Martensite decay in micropitted gears,” Proc. Inst. Mech. Eng. Part J J. Eng. Tribol., 219(2), pp. 77–83.

[49] Loy, B., and Mccallum, R., 1973, “B. LOY and R. McCALLUM,” 24, pp. 219–228.

[50] Sharma, V. K. "Roller contact fatigue study of austempered ductile iron."Journal of Heat Treating 3, no. 4 (1984): 326-334.

[51] Grad, P., Reuscher, B., Brodyanski, A., Kopnarski, M., and Kerscher, E., 2012, “Mechanism of fatigue crack initiation and propagation in the very high cycle fatigue regime of high-strength steels,” Scr. Mater., 67(10), pp. 838–841.

[52] King, A., 2013, “Electron Microscopy of Stress-Induced Structural Alterations Near Inclusions in Bearing Steels,” (September 1966), pp. 568–571.

[53] Oila, A., and Bull, S. J., 2005, “Phase transformations associated with micropitting in rolling/sliding contacts,” J. Mater. Sci., 40(18), pp. 4767–4774.

[54] Dufrane, K. F., and Glaeser, W. A., "Rolling-contact deformation of MgO single crystals." Wear 37, no. 1 (1976): 21-32.

[55] Sauger, E., Fouvry, S., Ponsonnet, L., Kapsa, P., Martin, J. ., and Vincent, L., 2000, “Tribologically transformed structure in fretting,” Wear, 245(1-2), pp. 39–52.

[56] Grabulov, A., 2010, “Fundamentals of Rolling Contact Fatigue.”,a PhD thesis.

[57] Umezawa, O., “Modeling of Crack Generation and Growth Under Rolling Contact Fatigue in Martensite Steels,” pp. 555–564.

[58] Evans, M. H., Wang, L., Jones, H., and Wood, R. J. K., 2013, “White etching crack (WEC) investigation by serial sectioning, focused ion beam and 3-D crack modelling,” Tribol. Int., 65(2), pp. 146–160.

[59] Evans, M. H., Richardson, A. D., Wang, L., and Wood, R. J. K., 2013, “Serial sectioning investigation of butterfly and white etching crack (WEC) formation in wind turbine gearbox bearings,” Wear, 302(1-2), pp. 1573–1582.

[60] Grabulov, A., 2010, “Fundamentals of Rolling Contact Fatigue.”

[61] Stiénon, A., Fazekas, A., Buffière, J. Y., Vincent, A., Daguier, P., and Merchi, F., 2009, “A new methodology based on X-ray micro-tomography to estimate stress concentrations around inclusions in high strength steels,” Mater. Sci. Eng. A, 513-514(C), pp. 376–383.

[62] Guy, P., and Meynaud, P., 1997, “Sub-surface damage investigation by high ultrasonic echography aring steel frequency on lOOCr6,” 30(4).

[63] Alley, E. S., and Neu, R. W., 2010, “Microstructure-sensitive modeling of rolling contact fatigue,” Int. J. Fatigue, 32(5), pp. 841–850.

[64] Vincent, A., Lormand, G., Lamagnere, P., Fougeres, R., Gosset, L., Girodin, D., and Dudragne, G., "From white etching areas formed around inclusions to crack nucleation in bearing steels under rolling contact fatigue". No. CONF-9611259--. American Society for Testing and Materials, West Conshohocken, PA (United States), 1998.

[65] Melander, A., "Simulation of the behaviour of short cracks at inclusions under rolling contact fatigue loading-specially the effect of plasticity." ASTM SPECIAL TECHNICAL PUBLICATION 1327 (1998): 70-86.

[66] Melander, A., and Ölund, P., 1999, “Detrimental effect of nitride and aluminium oxide inclusions on fatigue life in rotating bending of bearing steels,” Mater. Sci. Technol., 15(5), pp. 555–562.

[67] Melander, A. "A finite element study of short cracks with different inclusion types under rolling contact fatigue load." International Journal of Fatigue 19, no. 1 (1997): 13-24.

[68] Jiang, Y., and Sehitoglu, H., 1999, “A model for rolling contact failure,” Wear, 224(1), pp. 38–49.

[69] Lemaître, J., 1992, A course on damage mechanics, Springer-Verlag, Berlin; New York.

[70] Xiao, Y., Li, S., and Gao, Z., 1998, “A continuum damage mechanics model for,” 20(7), pp. 503–508.

[71] Bomidi, J. A. R., 2013, “Experimental and Numerical Investigation of Torsion Fatigue of Bearing Steel,” J. Tribol., 135(3), p. 031103.

[72] Bomidi, J. A. R., Weinzapfel, N., Sadeghi, F., Liebel, A., and Weber, J., 2013, “An Improved Approach for 3D Rolling Contact Fatigue Simulations with Microstructure Topology,” Tribol. Trans., 56(3), pp. 385–399.

[73] Bomidi, J. A. R., Weinzapfel, N., Wang, C.-P., and Sadeghi, F., 2012, “Experimental and numerical investigation of fatigue of thin tensile specimen,” Int. J. Fatigue, 44, pp. 116–130.

[74] Bolotin, V. V., and Belousov, I. L., 2001, “Early fatigue crack growth as the damage accumulation process,” Probabilistic Eng. Mech., 16(4), pp. 279–287.

[75] Shimizu, S., Tsuchiya, K., and Tosha, K., 2009, “Probabilistic Stress-Life (P-S-N) Study on Bearing Steel Using Alternating Torsion Life Test,” Tribol. Trans., 52(6), pp. 807–816.

[76] Lund, T. B., Beswick, J., and Dean, S. W., 2010, “Sub-Surface Initiated Rolling Contact Fatigue—Influence of Non-Metallic Inclusions, Processing History, and Operating Conditions,” J. ASTM Int., 7(5), p. 102559.

[77] Huwaldt, J. A., 2013, “PlotDigitizer.”

[78] Bomidi, J. A. R., Weinzapfel, N., and Sadeghi, F., 2012, “Three-dimensional modelling of intergranular fatigue failure of fine grain polycrystalline metallic MEMS devices,” Fatigue Fract. Eng. Mater. Struct., p. no–no.

[79] Lankford, J., "Inclusion-matrix debonding and fatigue crack initiation in low alloy steel." International Journal of Fracture 12, no. 1 (1976): 155-157. [80]
Bathias, C., 2012, “Gigacycle fatigue of bearing steels,” Mater. Sci. Technol., 28(1), pp. 27–33.

[81] Bathias, C., Field, D., Antolovich, S., and Paris, P. C., “Microplasticity , Microdamage , Microcracking in Ultrasonic Fatigue.”

[82] Sakai, T., Sato, Y., and Oguma, N., 2002, “Characteristic S-N properties of high-carbon-chromium-bearing steel under axial loading in long-life fatigue,” Fatigue <html_ent glyph=“@amp;” ascii=“&”/> Fract. Eng. Mater. Struct., 25(8-9), pp. 765–773.

[83] Neishi, Y., Makino, T., Matsui, N., Matsumoto, H., Higashida, M., and Ambai, H., 2012, “Influence of the Inclusion Shape on the Rolling Contact Fatigue Life of Carburized Steels,” Metall. Mater. Trans. A, 420(1), pp. 2131–2140.

[84] Evans, M. H., Richardson, A. D., Wang, L., Wood, R. J. K., and Anderson, W. B., 2014, “Confirming subsurface initiation at non-metallic inclusions as one mechanism for white etching crack (WEC) formation,” Tribol. Int., 75, pp. 87–97.

[85] Evans, M.-H., Wang, L., and Wood, R., 2014, “Formation mechanisms of white etching cracks and white etching area under rolling contact fatigue,” Proc. Inst. Mech. Eng. Part J J. Eng. Tribol.

[86] Donzella, G., Faccoli, M., Mazzù, A., Petrogalli, C., and Desimone, H., “On rolling contact fatigue of gear steels with different inclusion content,” pp. 783–790.

[87] Taylor, P., Clarke, T. M., Miller, G. R., Keer, L. M., and Cheng, H. S., 2008, “The Role of Near-Surface Inclusions in the Pitting of Gears The Role of Near-Surface Inclusions in the Pitting of Gearso,” (March 2014), pp. 37–41.

[88] Meredith, R., and Sewell, J., 1975, “Assessment of Nonmetallic Inclusion Content and the Relationship to Fatigue Life of One Percent Carbon-Chrome St ls.”

[89] Li, X. P., Choi, J., Kwon, O. D., and Yim, C., 1999, “Investigation of inclusion detection by acoustic microscope,” Met. Mater., 5(3), pp. 241–249.

[90] Dumont, M. L., and Vincent, A., 1999, “Role of Inclusions , Surface Roughness and Operating Conditions on Rolling Contact Fatigue,” 121(April).

[91] Saka, N., 1992, “The Mechanics of Crack Initiation at Hard Particles in Rolling Line Contacts,” 114(April).

[92] Melander, A., and Gustavsson, A., 1996, “An FEM study of driving forces of short cracks at inclusions in hard steels,” Int. J. Fatigue, 18(6), pp. 389–399.

[93] Mobasher Moghaddam, S., Sadeghi, F., Weinzapfel, N., and Liebel, A., 2014, “A Damage Mechanics Approach to Simulate Butterfly Wing Formation Around Nonmetallic Inclusions,” J. Tribol., 137(1), p. 011404.

[94] Raje, N., Sadeghi, F., Rateick, R. G., and Hoeprich, M. R., 2007, “Evaluation of Stresses Around Inclusions in Hertzian Contacts Using the Discrete Element Method,” J. Tribol., 129(2), p. 283.

[95] Raje, N., Sadeghi, F., and Rateick, R. G., 2008, “A Statistical Damage Mechanics Model for Subsurface Initiated Spalling in Rolling Contacts,” J. Tribol., 130(4), p. 042201.

[96] Jalalahmadi, B., and Sadeghi, F., 2009, “A Voronoi Finite Element Study of Fatigue Life Scatter in Rolling Contacts,” J. Tribol., 131(2), p. 022203.

[97] Warhadpande, A., Sadeghi, F., Kotzalas, M. N., and Doll, G., 2012, “Effects of plasticity on subsurface initiated spalling in rolling contact fatigue,” Int. J. Fatigue, 36(1), pp. 80–95.

[98] Weinzapfel, N., Sadeghi, F., and Bakolas, V., 2010, “An Approach for Modeling Material Grain Structure in Investigations of Hertzian Subsurface Stresses and Rolling Contact Fatigue,” J. Tribol., 132(4), p. 041404.

[99] Weinzapfel, N., Sadeghi, F., Bakolas, V., and Liebel, A., 2011, “A 3D Finite Element Study of Fatigue Life Dispersion in Rolling Line Contacts,” J. Tribol., 133(4), p. 042202.

[100] Slack, T., and Sadeghi, F., 2010, “Explicit finite element modeling of subsurface initiated spalling in rolling contacts,” Tribol. Int., 43(9), pp. 1693–1702.

[101] Shewchuk, J. R., “Triangle : Engineering a 2D Quality Mesh Generator and Delaunay Triangulator.”

[102] Littmann, W. E., and R. L. Widner. “Propagation of Contact Fatigue From Surface and Subsurface Origins,” (6), pp. 624–635.

[103] Carter, T. L., Butler, R. H., Bear, H. R., and Anderson, W. J., 1958, “Investigation of Factors Governing Fatigue Life with the Rolling-Contact Fatigue Spin Rig,” A S L E Trans., 1(1), pp. 23–32.

[104] Gegner, J., 2011, “Tribological Aspects of Rolling Bearing Failures,” C.-H. Kuo (ed.), Tribol. Lubr., pp. 33–94.

[105] Glover, D., "A ball-rod rolling contact fatigue tester." Rolling Contact Fatigue Testing of Bearing Steels, ASTM STP 771 (1982): 107-125.

[106] Oliver, W., and Pharr, G., "An improved technique for determining hardness and elastic modulus using load and displacement sensing indentation experiments." Journal of materials research 7, no. 06 (1992): 1564-1583.

[107] Luyckx, J., 2012, White Etching Crack Failure Mode in Roller Bearings: From Observation via Analysis to Understanding and an Industrial Solution, Rolling Element Bearings.

[108] Hiraoka, K., and Nagao, M., and Isomoto, T., 2006, “Study on flaking process in bearings by white etching area generation,” J. ASTM Int, 3(5), pp. 1–7.

[109] Weinzapfel, N, “PhD Thesis ”, Purdue University, 2010.

[110] Harris, T. A., 2001, Rolling bearing analysis, Wiley, New York, NY.

[111] Kang, J.-H., Hosseinkhani, B., and Rivera-Díaz-del-Castillo, P. E. J., 2012, “Rolling contact fatigue in bearings: multiscale overview,” Mater. Sci. Technol., 28(1), pp. 44–49.

[112] “Styri, H., 1951, ‘Fatigue Strength of Ball Bearings Races and Heat-Treated 52100 Steel Specimens,’ Proceedings of the American Society for Testing and Materials, Vol. 51, pp. 682–700.”

[113] Rahman, Z., Ohba, H., Yoshioka, T., and Yamamoto, T., 2009, “Incipient damage detection and its propagation monitoring of rolling contact fatigue by acoustic emission,” Tribol. Int., 42(6), pp. 807–815.

[114] Dumont, M. L., and Vincent, A., 2015, “Role of Inclusions , Surface Roughness and Operating Conditions on Rolling Contact Fatigue,” 121(April 1999).

[115] “Auclair, G., and Daguier, P., ‘Appropriate Techniques for Internal Cleanliness Assessment,’ Bearing ,Steel Technology ASTM STP 1419, J. M. Beswick, Eds., American Society for Testing Materials International, West Conshohocken, PA, 2002.”

[116] Deneuville, F., Duquennoy, M., Ouaftouh, Ourak, M., Jenot, F., and Desvaux, S., 2009, “High frequency ultrasonic detection of C-crack defects in silicon nitride bearing balls,” Ultrasonics, 49(1), pp. 89–93.

[117] Hiraoka, K., Nagao, M., and Isomoto, T., ‘Study on flaking process in bearings by white etching area generation.’ J. ASTM Int 3, no. 5 (2006): 1-7.”

[118] Cerullo, M., 2014, “Sub-surface Fatigue Crack Growth at Alumina Inclusions in AISI 52100 Roller Bearings,” Procedia Eng., 74, pp. 333–338.

[119] Cerullo, M., and Tvergaard, V., ‘Micromechanical study of the eff; ect of inclusions on fatigue failure in a roller bearing.’ International Journal of Structural Integrity 6, no. 1 (2015).”

[120] Mobasher Moghaddam, S., Sadeghi, F., Paulson, K., Weinzapfel, N., Correns, M., Bakolas, V., and Dinkel, M., 2015, “Effect of non-metallic inclusions on butterfly wing initiation, crack formation, and spall geometry in bearing steels,” Int. J. Fatigue, 80, pp. 203–215.

[121] Errichello, R., 2011, “Microstructural Alterations in Hertzian Fatigue,” NREL Wind turbine Tribol. Semin.

[122] Selecka, M., and Salak, A., 1999, “Durability and failure of powder forged rolling bearing rings ˇ.”

[123] Weinzapfel, N., and Sadeghi, F., 2013, “Numerical modeling of sub-surface initiated spalling in rolling contacts,” Tribol. Int., 59, pp. 210–221.

[124] “Littmann, W. E., and R. L. Widner. ‘Propagation of contact fatigue from surface and subsurface origins.’ Journal of Fluids Engineering 88, no. 3 (1966): 624-635.”

[125] Raje, N., Sadeghi, F., and Rateick, R., ‘A statistical damage mechanics model for subsurface initiated spalling in rolling contacts.’ Journal of Tribology 130, no. 4 (2008): 042201.”

[126] Douglas, G., ‘A ball-rod rolling contact fatigue tester.’ Rolling Contact Fatigue Testing of Bearing Steels, ASTM STP 771 (1982): 107-125.”

[127] “http://www.sonoscan.com/.”

[128] Norimasa, T., Kazuya, H., Takeshi, F., and Kazuhiko, H., 2012, “Initiation Behavior of Crack Originated from Non-Metallic,” 7(2), pp. 1–10.

[129] Nélias, D., Dumont, M. L., Champiot, F., Vincent, A., Girodin, D., Fougéres, R., and Flamand, L., 1999, “Role of Inclusions, Surface Roughness and Operating Conditions on Rolling Contact Fatigue,” J. Tribol., 121(2), p. 240.

[130] Harrer, B., Kastner, J., Winkler, W., and Degischer, H. P., 2008, “On the Detection of Inhomogeneities in Steel by Computed Tomography,” Mater. Sci., pp. 1–7.

[131] Makino, T., Neishi, Y., Shiozawa, D., Fukuda, Y., Nakai, Y., Kajiwara, K., and Nakai, Y., 2014, “Evaluation of rolling contact fatigue crack path in high strength steel with artificial defects,” Int. J. Fatigue, pp. 579–586.

[132] Turnbull, A., Carroll, M. W., and Ferriss, D. H., 1989, “Analysis of hydrogen diffusion and trapping in a 13% chromium martensitic stainless steel,” 31(I), pp. 2039–2046.

[133] Karsch, T., Bomas, H., Zoch, H.-W., and Mändl, S., 2014, “Influence of hydrogen content and microstructure on the fatigue behaviour of steel SAE 52100 in the VHCF regime,” Int. J. Fatigue, 60, pp. 74–89.

[134] Fujita, S., Matsuoka, S., Murakami, Y., and Marquis, G., 2010, “Effect of hydrogen on Mode II fatigue crack behavior of tempered bearing steel and microstructural changes,” Int. J. Fatigue, 32(6), pp. 943–951.

[135] Solano-Alvarez, W., Song, E. J., Han, D. K., Suh, D.-W., and Bhadeshia, H. K. D. H., 2014, “Cracks in Martensite Plates as Hydrogen Traps in a Bearing Steel,” Metall. Mater. Trans. A, 46(2), pp. 665–673.

[136] Ju, E., Suh, D., and Bhadeshia, H. K. D. H., 2013, “Theory for Hydrogen Desorption in Ferritic Steel,” 79(May), pp. 36–44.

[137] Paper, T., 2006, “The Influence of Hydrogen on Tension-Compression and Rolling Contact Fatigue Properties of Bearing Steel,” (74).

[138] Hamada, H., and Matsubara, Y., “A Novel Method to Evaluate the Influence of Hydrogen on Fatigue Properties of High Strength Steels,” 3(2), pp. 153–166.

[139] Shimizu, S., 2005, “P-S-N/P-F-L Curve Approach Using Three-Parameter Weibull Distribution for Life and Fatigue Analysis of Structural and Rolling Contact Components,” Tribol. Trans., 48(4), pp. 576–582.

VITA

VITA

Sina Mobasher Moghaddam was born on October 15th, 1987 in Tehran, Iran. He attended Sharif University of Technology from 2006 to 2011 where he obtained his Bachelor of Science in mechanical engineering. After graduation he applied to Purdue University and enrolled in the Master of Science program where he obtained his degree under supervision of Professor Farshid Sadeghi in the Mechanical Engineering Tribology Laboratory (METL) in 2013. He pursued his graduate studies towards a doctorate degree at METL and obtained his PhD in Spring 2016.

PUBLICATIONS

LIST OF PUBLICATIONS

Moghaddam Moghaddam, S., Bomidi, J.A.R., Sadeghi, F., Weinzapfel, N., and Liebel, A., "Effects of compressive stresses on torsional fatigue." Tribology International 77 (2014): 196-210.

Moghaddam Moghaddam, S., Sadeghi, F., Weinzapfel, N., and Liebel, A., "A Damage Mechanics Approach to Simulate Butterfly Wing Formation Around Nonmetallic Inclusions." Journal of Tribology 137, no. 1 (2015): 011404.

Moghaddam Moghaddam, S., Sadeghi, F., Paulson, K., Weinzapfel, N., Correns, M., Bakolas, V., and Dinkel, M., "Effect of non-metallic inclusions on butterfly wing initiation, crack formation, and spall geometry in bearing steels." International Journal of Fatigue 80 (2015): 203-215.

Mobasher Moghaddam, S., Sadeghi, F., "An Overview of Microstructural Alterations around Non-Metallic Inclusions in Bearing Steel during Rolling Contact Fatigue", (Accepted for publication at Tribology Transactions)

Mobasher Moghaddam, S., Sadeghi, F., Paulson, K., Weinzapfel, N., Correns, M., Bakolas, V., and Dinkel, M., "A 3D Analytical and Experimental Investigation of Microstructural Alterations Around Inclusions in Bearing Steel", (Under review at International Journal of Fatigue)